UNIVERSITY OF LIVERPOOL

NANOMATERIAL COMPOSITE SYNTHESIS TO ACHIEVE VISIBLE LIGHT ACTIVE PHOTOCATALYSTS

THESIS SUBMITTED IN ACCORDANCE WITH THE REQUIREMENTS OF THE UNIVERSITY OF LIVERPOOL FOR THE DEGREE OF DOCTOR IN PHILOSOPHY

BY

RUOCHEN LIU

August/2021

PGR Declaration of Academic Honesty

NAME (Print)	**RUOCHEN LIU**
STUDENT NUMBER	**1101663**
SCHOOL/INSTITUTE	**School of Science – Department of Chemistry**
TITLE OF WORK	**NANOMATERIAL COMPOSITE SYNTHESIS TO ACHIEVE VISIBLE LIGHT ACTIVE PHOTOCATALYSTS**

This form should be completed by the student and appended to any piece of work that is submitted for examination. Submission by the student of the form by electronic means constitutes their confirmation of the terms of the declaration.

Students should familiarise themselves with Appendix 4 of the PGR Code of Practice: PGR Policy on Plagiarism and Dishonest Use of Data, which provides the definitions of academic malpractice and the policies and procedures that apply to the investigation of alleged incidents.

Students found to have committed academic malpractice will receive penalties in accordance with the Policy, which in the most severe cases might include termination of studies.

STUDENT DECLARATION

I confirm that:

- I have read and understood the University's PGR Policy on Plagiarism and Dishonest Use of Data.
- I have acted honestly, ethically and professionally in conduct leading to assessment for the programme of study.
- I have not copied material from another source nor committed plagiarism nor fabricated, falsified or embellished data when completing the attached material.
- I have not copied material from another source, nor colluded with any other student in the preparation and production of this material.
- If an allegation of suspected academic malpractice is made, I give permission to the University to use source-matching software to ensure that the submitted material is all my own work.

SIGNATURE……………………………………………………………………………………………
………………..

DATE………………………………………………………………………………………………………
……………….

Abstract

Trititanate nanotube (TiNT) is an inexpensive, harmless semiconductor and can be simply prepared from TiO_2 via a hydrothermal process. It has a high surface area and photoactivity, and it has shown potential applications as adsorbent and photocatalyst towards waste water treatment, such as removal of methylene blue. However, due to its large band gap, it can only be activated by UV light, which is less than 5% in the solar spectrum. Thus, improving the photoactivity of TiNT under visible light is necessary.

This thesis aims to improve the photoactivity of TiNT under visible light by surface modification of TiNT. In Chapter 4, TiNT was modified by organic compounds with a catechol structure, and the light absorbance was extended to the visible light range. More importantly, selective enhanced Raman scattering was reported, which was explained by the formation of the charge transfer complex and the HOMO and LUMO positions of the modifiers. This part of the work was published as SERS of Trititanate Nanotubes: Selective Enhancement of Catechol Compounds. Chem. Select, 2018, 3 (28), 8338-8343. In Chapter 5, TiNT was modified by graphitic C_3N_4, which was a semiconductor prepared from urea. The resulted nanocomposites have shown high adsorption/photodegradation ability depending on the annealing temperature. In Chapter 6, TiNT was modified by synthesized organic linker and gold nanoparticles. However, the product did not show improvement in photodegradation of methylene blue.

This thesis introduced the basic background and mechanism of TiNT photocatalyst and included a literature review of titanate nanotubes, graphitic carbon nitride, and surface plasmon effect by gold nanoparticles. This thesis summarized the main outcomes of a PhD project, which contained surface enhanced Raman scattering by TiNT-catechol systems, high adsorption/photodegradation activities by TiNT-C_3N_4 composites, and researches on AuNP-Organic-TiNT composites.

Acknowledgement

Firstly, I would like to express my sincere gratitude to my supervisor Prof. Graham Dawson. I appreciate his patient, encouragement, and guidance during the past four years. The present work would not have been possible without his support. Prof. Dawson is not only my academic supervisor but also a friend of mine. Talking to him is always a pleasure. His positive attitude toward working and life affect me much.

I would like to thank Prof. Eric Amigues for his help in organic chemistry. He gave me great help when I was new to organic synthesis. He answered all my organic questions patiently. I would also like to thank Prof. Kim Lau. The talks with him made me think deeply, not only of chemistry but also of philosophy. Many thanks to all the chemistry department staff, especially Ms Jianfang Wu, Ms Tong Ji, and Ms Peipei Wang, for their technical support.

Many appreciations go to Mr Shiqi Zhao, who had lots of academic discussions and daily talks with me, and gave me a big help in the lab. I would also thank our group members and my friends, especially Ms Luna Zhang, Mr Yuanxun Zhang, Mr Yang Zhang and Mr Nan Zhou.

I am particularly grateful to my and my wife’s families for their constant support. Special thanks to my wife, Mrs Lixi Sun, who always accompanies me, supports me, motivates me, and encourages me.

Publications

1. Liu, R.; Morris, E.; Cheng, X.; Amigues, E.; Lau, K.; Kim, B.; Liu, Y.; Ke, Z.; Ashbrook, S. E.; Bühl, M.; Dawson, G., SERS of Trititanate Nanotubes: Selective Enhancement of Catechol Compounds. *Chem. Select,* **2018,** *3* (28), 8338-8343.

2. Dawson, G., Cheng, X., Centeno, A. *et al.* Excellent surface enhanced Raman properties of titanate nanotube-dopamine-Ag triad through efficient substrate design and LSPR matching. *J Mater Sci: Mater Electron* **32,** 21603–21610 (2021).

Table of Contents

PGR Declaration of Academic Honesty..i

Abstract iii

Acknowledgement v

Publications vii

Table of Contents...1

List of Abbreviations..5

List of Figures..9

List of Tables 23

Chapter 1: Introduction..24

1.1 Background..24

1.2 Photodegradation Mechanism..26

1.3 Factors affecting photodegradation..27

1.3.1 pH 27

1.3.2 Photocatalyst Adsorption and Load Amount 29

1.3.3 Light Source 31

1.4 Removal of Methylene Blue 32

1.5 Research Scheme 34

1.6 Chapters Summary 36

Chapter 2 Literature Review 38

2.1 TiO_2 and Trititanate Nanotubes as Photocatalyst........................... 38

2.1.1 TiO_2.. 38

2.1.2 Trititanate Nanotubes.. 41

2.2 Graphitic Carbon Nitride as Photocatalyst..................................... 46

2.3 Gold Nanoparticles and Surface Plasmon Resonance...................... 50

Chapter 3 Instrumentation 54

3.1 Instrumentation Information... 54

3.2 Principles of Primary Instrumentation 55

3.3 Sample preparation and Analysis Methods.................................... 63

Chapter 4: Surface Enhanced Raman Scattering 69

4.1 Preface 69

4.2 Experimental Section 69

4.3 Results and Discussions 71

4.4 Conclusion 92

Chapter 5: C_3N_4-TiNT Nanocomposite.. 94

5.1 Preface 94

5.2 Experimental Section 94

5.3 Results and Discussions 99

5.3.1 Protonation of g-C_3N_4.. 99

5.3.2 Characterization of C_3N_4-TiNT System................................ 102

5.3.3 Investigation of Annealed TiNT 125

5.3.4 Methylene Blue Standard Curve 131

5.3.5 Methylene Blue Degradation Pathway 133

5.3.6 Methylene Blue Self-Degradation and Degradation Catalysed by TiNT and g-C_3N_4 136

5.3.7 Methylene Blue Degradation Catalysed by TiNT-C_3N_4 and TiNT-dopamine-C_3N_4 Composites 139

5.3.8 Methylene Blue Degradation Catalysed Under Visible Light . 145

5.4 Conclusion 146

Chapter 6: AuNP-Organic-TiNT Composites and Organic Synthesis 148

6.1 Preface 148

6.2 Experimental Section 149

6.2.1 Gold Nanoparticles Synthesis 150

6.2.2 Organic Synthesis 153

6.2.3 Au-Organic-TiNT Nanocomposites Synthesis 157

6.3 Results and Discussions 162

6.3.1 Gold Nanoparticles 162

6.3.2 Discussion of Organic Reactions 165

6.3.3 Results and Discussion of AuNP-Organic-TiNT Composite ... 169

6.4 Conclusion 186

Chapter 7: Summary and Future Work 187

Reference List 189

Appendix.. 202

List of Abbreviations

a.u.	Absorbance Unit
AO7	Acid Orange 7
ATR	Attenuated Total Reflectance
AuNP	Gold Nanoparticle
CB	Conduction Band
CPS	Count per Second
d	Doublet
DCM	Dichloromethane
dd	Doublet of Doublets
DFT	Density Functional Theory
DMF	N,N-Dimethylformamide
DMSO	Dimethylsulfoxide
dop	Dopamine
e^-	Electrons
EDX	Energy-Dispersive X-Ray Spectroscopy
EF	Enhancement Factor
Eg	Energy Gap
EM	Electromagnetic
EtOAc	Ethylacetate
EtOH	Ethanol

FTIR	Fourier Transform Infrared Spectroscopy
FWHM	Full Width at Half Maximum
g-C_3N_4	Graphitic Carbon Nitride
GC-MS	Gas Chromatography-Mass Spectrometer
h^+	Positive Electron Holes
HOMO	Highest Occupied Molecular Orbitals
HRTEM	High Resolution Transmission Electron Microscopy
KSAc	Potassium Thioacetate
LC-MS	Liquid Chromatography-Mass Spectrometer
LSPR	Localized Surface Plasmon Resonance
LUMO	Lowest Unoccupied Molecular Orbital
m	Multiplet
m/z	Mass-to-Charge Ratio
MB	Methylene Blue
MeCN	Acetonitrile
MeOH	Methanol
NMR	Nuclear Magnetic Resonance Spectroscopy
PE	Petroleum Ether
PIRET	Plasmon-Induced Resonance Energy Transfer
PPh_3	Triphenylphosphine
ppm	Part per Million

RB4	Reactive Blue 4
s	Singlet
SAc	Thioacetate
SEM	Scanning Electron Microscope
SERS	Surface Enhanced Raman Scattering
SPR	Surface Plasmon Resonance
ssNMR	Solid-State Nuclear Magnetic Resonance Spectroscopy
t	Triplet
TEA	Triethylamine
TEM	Transmission Electron Microscope
TFA	Trifluoroacetic Acid
TGA	Thermogravimetric Analysis
TiNT	Trititanate Nanotube
TLC	Thin Layer Chromatography
TOAB	Tetraoctylammonium Bromide
UV	Ultraviolet
UV-Vis	Ultraviolet-visible
v:v	Volume to Volume
VB	Valence Band
WC	Weight Concentration
wt.%	Weight Percent

XPS	X-ray Photoelectron Spectroscopy
XRD	X-ray Diffraction
δ	Chemical Shift

List of Figures

Figure 1 Structures of (a) Reactive Orange 4; (b) Chromotrope 2B; (c) Amido Black 10B. They are anionic dyes and the degradation rates of them are sensitive to pH values. 28

Figure 2 Structure of Methylene Blue, which is a cationic dye and its aqueous solution is weak alkaline. 29

Figure 3 The colours of MB solutions with different weight concentrations from left to right: 1 g/L, 100 mg/L, 10 mg/L, and 1 mg/L. The blue colour of MB is still significant under low concentration. 33

Figure 4 Target structure of TiNT-organic-AuNP system. Organic linkers are attached to TiNT surface by catechol structure and attach to AuNPs via free thiol group. 35

Figure 5 Crystal structure of (a)rutile; (b)anatase; (c)brookite. Blue octahedral stands for TiO_6 blocks and purple spheres stand for Ti atoms.[51] They have distorted TiO_6 octahedra, in which titanium cations are coordinated to 6 oxygen atoms. (Figure reprinted with the permission of RSC, ref 51) 39

Figure 6 Photocatalysis mechanism of TiO_2. Electrons are excited to conduction band under light illumination and participate in reduction. Holes are left in the valence band and participate in oxidation....... 40

Figure 7 Structural and morphological transformation of a protonated titanate nanotube during thermal treatment.[69] Titanate can transform to monoclinic TiO_2 (B) at <350 °C by loss of water and finally to TiO_2 anatase at <450 °C. (Figure reprinted with the permission of ACS, ref 69)..44

Figure 8 Structure of g-C_3N_4: consist of tri-*s*-triazine units connected by planar amino groups..46

Figure 9 Reaction pathway of g-C_3N_4[97] from different precursors including urea, thiourea, dicyandiamide and melamine to melam, melem and finally g-C_3N_4. (Figure reprinted with the permission of RSC, ref 97) 49

Figure 10 A schematic of a localized surface plasmon[103] (Figure reprinted with the permission of ANNUAL REVIEWS, ref 103)..................51

Figure 11 Illumination of Bragg's law: $n\lambda = 2d\sin\theta$, where n is the order of reflection, λ is the wavelength of incident X-ray, d is the spacing between the crystal planes, and θ is the glancing angle...............58

Figure 12 Component of a TEM instrument. From top to bottom: the electron gun, condenser, specimen, objective lens, objective aperture, projector lens, and viewing screen,..59

Figure 13 Principle of Raman. Stokes and anti-Strokes Raman scattering are caused by the excitations going back to higher/lower energy levels and releasing light with a different frequency from the incident light.

....61

Figure 14 (a) monodentate model of TiNT-dopamine system: one hydroxyl group attach to TiNT and the other hydroxyl group interact with other dopamine molecules through hydrogen bonds; (b) bidentate model of TiNT-dopamine system: two hydroxyl groups attached to TiNT and dopamine molecules interact through π-π stacking [33] (Figure reprinted with the permission of John Wiley and Sons, ref 33)....................72

Figure 15 Structures of dopamine, 3-hydroxytyrosol, 3.4-dihydroxybenzoic acid and 4-nitrocatechol. They all contain a catechol structure, but the ending groups are different...73

Figure 16 Photos of TiNT-catechol samples from left to the right: TiNT, TiNT-3,4-dihydroxybenzoic acid, TiNT-4-nitrocatechol, TiNT-3-hydroxytyrosol, and TiNT-dopamine. TiNT is white when the TiNT-catechol compounds show colours from light brown to dark brown. 74

Figure 17 UV-Vis absorbance of catechol functionalized TiNT systems. TiNT-catechol samples show charge transfer band[124] dominating the visible range of the spectrum up to 600 nm and a shoulder at around 380 nm..75

Figure 18 ssNMR spectrum of (a) 3,4-dihydroxybenzoic acid, (b) TiNT-3,4-dihydroxybenzoic acid, (c) 4-nitrocatechol, (d) TiNT-4-nitrocatechol,

(e) 3-hydroxytyrosol and (f) TiNT-3-hydroxytyrosol. The spectra indicated the attachment of organic molecules on TiNT by the shifting of peaks..78

Figure 19 FTIR of (a) dopamine and TiNT-dopamine[33], (b) 4-nitrocatechol & TiNT-4-nitrocatechol, (c) 3,4-dihydroxybenzoic acid & TiNT-3,4-dihydroxybenzoic acid, and (d) 3-hydroxytyrosol & TiNT-3-hydroxytyrosol. The weakening of OH peaks indicated the replacement of the C-O-H bond by the C-O-Ti bond. (Figure reprinted with the permission of John Wiley and Sons, ref 33)....................80

Figure 20 XRD patterns of TiNT and TiNT-catechol. TiNT: peaks at 25° and 28° are the nanotube interlayer spacing (110) and (310); peak at 48° is the hydrogen titanate compounds (020). TiNT-catechol: broad peak at 28° is caused by π-π stacking; new peak at 13° is the interaction between the layers of nanotubes...82

Figure 21 TEM images of (a) TiNT, (b) TiNT-dopamine[33] and (c) & (d) TiNT-4-nitrocatechol. The nanotube has a diameter around 10 nm and a length around 100 nm. The morphology of nanotubes did not change upon surface modification. (Figure 21 (b) was reprinted with the permission of John Wiley and Sons, ref 33).................................83

Figure 22 TGA Temperature-Weight % curves of (a)TiNT and (b)TiNT-3,4-dihydroxybenzoic acid. TiNT lost 13.3 wt. % of water up to 350 °C, when TiNT-3,4-dihydroxybenzoic acid had an additional loss of 4.7 wt. % as loss of 3,4-dihydroxybenzoic acid on the nanotube surfaces...... 84

Figure 23 Raman spectra of (a) 4-nitrocatechol (0.1 M) and TiNT-4-nitrocatechol. (b) 3,4-dihydroxybenzoic acid (0.1 M) and TiNT-3,4-dihydroxybenzoic acid. (c) TiNT and TiNT-4-nitrocatechol. The enhancement of signals was ~10 fold for TiNT-3,4-dihydroxybenzoic acid and ~75 fold for TiNT-4-nitrocatechol. 89

Figure 24 DFT calculation results. The HOMO and LUMO positions of TiNT-catechol, TiNT-4-nitrocatechol and TiNT-dopamine were 1.35 eV, 1.62 eV and 1.88 eV respectively 91

Figure 25 Setup of photodegradation. Total power of Xe lamp is 300 W, and the distance between reactor and lamp is 120 cm. 99

Figure 26 Zeta potential of TiNT (-27.3 mV, a negatively charged surface), g-C_3N_4 (1.6 mV, a nearly neutral surface) and p-C_3N_4 (23.2 mV, a positively charged surface)... 100

Figure 27 UV-Vis spectrum of (a)p-C_3N_4 compared with g-C_3N_4; (b)p-C_3N_4-TiNT-1:3 compared with g-C_3N_4-TiNT-1:3. No obvious difference of absorbance band position could be found for both p-C_3N_4 and the composite prepared from p-C_3N_4 101

Figure 28 XRD of p-C_3N_4-TiNT-1:3 (top); g-C_3N_4-TiNT-1:3 (bottom). The XRD patterns show no obvious difference, which means the protonation process did not change the phase of samples.......... 101

Figure 29 UV-Vis absorbance of TiNT, p-C_3N_4, C_3N_4-TiNT-1:2 and C_3N_4-TiNT-1:3. TiNT shows a band gap of 3.2 eV when the C_3N_4 composites show a similar band gap to carbon nitride, which is 2.76 eV. 103

Figure 30 UV-Vis absorbance of C_3N_4-TiNT-1:2, C_3N_4-TiNT-1:2-300°C and C_3N_4-TiNT-1:2-400°C. All samples show the same band gap, which is 2.8 eV. 104

Figure 31 Tauc plots of C_3N_4-TiNT-1:2, C_3N_4-TiNT-1:2-300°C and C_3N_4-TiNT-1:2-400°C 105

Figure 32 UV-Vis absorbance of TiNT-dopamine, C_3N_4-TiNT-dop-1:2, C_3N_4-TiNT-dop-1:2-300°C and TiNT-dop-1:2-400°C. TiNT-dopamine and C_3N_4-TiNT-dop-1:2 show absorbance in the visible light range. The bands of composites were donated by both TiNT-dopamine and C_3N_4. 106

Figure 33 ATR-FTIR spectrum of g-C_3N_4, C_3N_4-TiNT-3:1-400°C, C_3N_4-TiNT-1:2-300°C, and C_3N_4-TiNT-1:2-400°C. The peak at 810 cm^{-1}: breathing mode of tri-s-triazine[137]; 890 cm^{-1}: deformation mode of N-H in amino groups[139]; 1200-1650 cm^{-1}: stretching modes of CN heterocycles[138]; 3000-3300 cm^{-1}: amino groups[138] exists in the samples, and O-H bond from surface adsorbed water. 108

Figure 34 (a)-(b) TEM of C_3N_4-TiNT-1:1; (c) TEM of C_3N_4-TiNT-1:1 heated under 550°C; (d) HRTEM of C_3N_4-TiNT-1:1 heated under 550°C. (a) and (b) shows the morphology of TiNT did not change upon mixing. (c) shows the disappearance of tubular structures and the appearance of nanoparticles. (d) shows the d-spacing of nanoparticles which is 0.35 nm and corresponds to the (101) surface of anatase........... 110

Figure 35 TEM (left) and HRTEM (right) images of (a)&(b): C_3N_4-TiNT-dop-1:2; (c)&(d): C_3N_4-TiNT-dop-1:2-300°C; (e)&(f): C_3N_4-TiNT-dop-1:2-400°C. (a) and (b) show the morphology of TiNT and C_3N_4 in the composite. (c) and (d) show the appearance of nanoparticles when the morphology of nanotubes and nanosheets did not change after annealing at 300 °C. (e) and (f) show the existence of nanoparticles with a d-spacing of 0.35 nm, which corresponded to the (101) surface of anatase... 112

Figure 36 XPS Ti2p of C_3N_4-TiNT and C_3N_4-TiNT-dop Composites........ 114

Figure 37 XPS N1s of C_3N_4-TiNT and C_3N_4-TiNT-dop Composites......... 116

Figure 38 XPS O1s of C_3N_4-TiNT and C_3N_4-TiNT-dop Composites......... 118

Figure 39 C1s of C_3N_4-TiNT and C_3N_4-TiNT-dop Composites................ 120

Figure 40 XPS-VB of TiNT. The valence band position of TiNT was 2.3 eV. The band gap of TiNT was 3.2 eV, and thus the conduction band was proposed to be at -0.9 eV.. 121

Figure 41 Band diagram of C_3N_4-TiNT composite. The band positions were proposed from XPS-VB spectra and band gaps of TiNT and C_3N_4. 122

Figure 42 XPS-VB of (a) g-C_3N_4-TiNT-dop 1:2; (b) g-C_3N_4-TiNT-dop 1:2-300°C 123

Figure 43 XRD patterns of TiO_2, g-C_3N_4, C_3N_4-TiNT-1:2-300°C and C_3N_4-TiNT-1:2-400°C. The composite annealed at 400 °C shows strong signals of anatase TiO_2 due to the transformation from TiNT to TiO_2 when the composite annealed at 300 °C shows poor signals due to the low content of TiO_2. 124

Figure 44 XRD patterns of TiO_2, g-C_3N_4, C_3N_4-TiNT-3:1-300°C and C_3N_4-TiNT-3:1-400°C. The composite annealed at 300 °C shows strong C_3N_4 peaks, but the intensities of anatase peaks are low. The composite annealed at 400 °C show strong anatase signals. 125

Figure 45 Photos of TiNT and heated TiNT samples (a) TiNT; (b) TiNT-150; (c) TiNT-250; (d) TiNT-350; (e) TiNT-450; (f) TiNT-550 126

Figure 46 UV-Vis absorbance of TiNT and heated TiNT samples. Samples have no significant difference in absorbance, and the band gap of TiNT did not change upon annealing. 126

Figure 47 X-Ray Diffraction of TiNT, heated TiNT, and TiO_2. TiNT shows peaks at 25.5°, 28.4°, 38.0° and 48.2°, which stand for (110), (310), (113), and (020) planes, respectivley[68]. Anatase TiO_2 shows peaks at 25.4°, 37.0°, 37.9°, 38.7°, 48.1°, 53.9° and 55.1°, which stand for

(101), (103), (004), (112), (200), (105) and (211). The annealing process of TiNT leads to the destruction of the tubular structure, and the formation of anatase crystal and stronger anatase signals can be observed for the TiNT annealed at higher temperatures............. 128

Figure 48 (a) TEM image of TiNT; (b)-(d) TEM and HRTEM images of TiNT-550. TiNT shows a tubular structure with a diameter of ~10nm and a length of ~100nm. TiNT-550 has shown three morphologies: long tubes like TiNT, small nanosheets, and nanoparticles. The d-spacing of nanoparticle was measured as ~0.34 nm, which corresponded to the (101) surface of anatase when a d-spacing of nanotube was ~0.19 nm, which corresponded to the (020) surface[68] of TiNT.............. 130

Figure 49 Binding energy of TiO_2, TiNT and TiNT-550........................ 131

Figure 50 Methylene blue standard curve. Absorbance=0.21267*weight concentration and R^2 is 0.99895. This equation was used to calculate the weight concentration of samples.. 133

Figure 51 Proposed degradation pathway of Methylene Blue. The intermediates were determined by GC-MS................................. 135

Figure 52 Baseline, TiNT and g-C_3N_4: (a) Weight concentration changed versus time; (b) Weight concentration ratio changed versus time. TiNT adsorbed 0.4 mg of MB within two hours which was 12 times than g-C_3N_4. 41% of MB has self-degraded after 5 hours of illumination. g-

C_3N_4 has shown a rapid degradation rate in the first hour, but later the degradation was slow. TiNT has shown better degradation than g-C_3N_4, which degraded 71% of MB in five hours. 138

Figure 53 Methylene blue degradation catalysed by annealed C_3N_4-TiNT 1:2 and 3:1 composites: (a) Weight concentration changed versus time; (b) Weight concentration ratio changed versus time. The C_3N_4-TiNT-1:2 composite annealed at 300 ^{o}C shows the highest absorption ability, while the C_3N_4-TiNT-1:2 composite annealed at 400 ^{o}C shows the highest degradation ability. The C_3N_4-TiNT-3:1 sample shows poor absorption and degradation ability due to the high content of C_3N_4. 140

Figure 54 Methylene blue degradation catalysed by annealed C_3N_4-TiNT 1:3 composites: (a) Weight concentration changed versus time; (b) Weight concentration ratio changed versus time. The sample annealed at 300 ^{o}C shows high adsorption ability and removed 46% of methylene blue in the first hour. The sample annealed at 400 ^{o}C shows a very low adsorption ability (0.11 mg). However, this sample had a 71% removal rate in the first hour under light illumination and 88.5% within two hours. 142

Figure 55 Methylene blue degradation catalysed by C_3N_4-TiNT-dopamine 1:3 composites: (a) Weight concentration changed versus time; (b)

Weight concentration ratio changed versus time. TiNT-dopamine and C_3N_4-TiNT-dop-1:2 annealed under 300 °C have shown similar adsorption and photocatalytic ability to the composite without dopamine. The composite annealed under 400 °C shows poorer adsorption than C_3N_4-TiNT-1:2-400°C, but no obvious difference in degradation rate. 144

Figure 56 Photodegradation of methylene blue under visible light 145

Figure 57 Organic linkers in Au-Organic-TiNT nanocomposites (a) F2029; (b)F2037; (c)F2050. They all have catechol structures and a free thiol group as an ending group. 149

Figure 58 UV-Vis absorbance of AuNP-PPh_3. No obvious SPR peak was found. 163

Figure 59 UV-Vis absorbance of AuNPs prepared by Burst method. An SPR peak at ~515 nm was found. 164

Figure 60 UV-Vis absorbance of AuNPs prepared by Martin method. An SPR peak at ~515 nm was found. 165

Figure 61 UV-Vis absorbance of F2029 and F2030. F2029 shows the TiNT profile, a charge transfer band, and SPR peak of AuNPs. F2030 shows a charge transfer band and similar SPR peak with higher overall intensities. 170

Figure 62 TEM and HRTEM images of (a)-(c): F2029; (d)-(f): F2030. (a) and (b) shows the morphology of F2029, which contained nanotubes from TiNT and nanoparticles from AuNPs. (c) indicated the d-spacing of the nanoparticle, which was 0.24 nm and corresponded to the (111) surface of Au[153].(d)-(f) shows the morphology and HRTEM of F2030, which were similar to F2029. 171

Figure 63 UV-Vis absorbance of F2037 I and F2037 II. TiNT profile and charge transfer band can be found for F2037 I but no SPR peak. Compared to F2037 I, F2037 II has a broad peak at ~550 nm. ... 172

Figure 64 TEM and HRTEM images of F2037 II. (a) and (b) shows the morphology of composite, which contained nanotubes and nanoparticles. (c) and (d) indicated the d-spacing of nanoparticles, which corresponded to the (111) surface of Au[153]...................... 173

Figure 65 TEM and HRTEM images of F2050. (a) and (b) shows the morphology of composite, which contained nanotubes and nanoparticles. (c) and (d) indicated the d-spacing of nanoparticles, which corresponded to the (111) surface of Au[153]...................... 175

Figure 66 UV-Vis absorbance of F2041B, F2042 and F2050. F2041 B and F2042 show TiNT profile and charge transfer profile, which was similar to other TiNT-catechol systems. F2050 shows a strong peak at 526 nm, which was attributed to the LSPR effect of AuNPs. 176

Figure 67 XPS C1s spectrum of F2050. The peak at 284.4 eV was assigned as C-C and C=C from both aromatic ring and carbon chain[158], as well as carbon addiction for calibration purposes. The peak at 286.6 eV was dominated by C-O/C-S[159], which was from the hydroxyl groups on the catechol structure and thiol ending group. 288.9 eV was assigned as a C=O double bond. 177

Figure 68 XPS O1s spectrum of F2050. The peak at 530.4 eV was assigned as O-Ti. The broad peak at 531.4 eV was donated by O-C organic bonds and O-H bonds. 179

Figure 69 XPS Ti2p spectrum of F2050 179

Figure 70 XPS Au4f spectrum of F2050. The peaks at 83.4 eV and 87.1 eV stands for Au4f$_{7/2}$ and Au4f$_{5/2}$ of Au^{0,} respectively.[159, 160] 181

Figure 71 XPS (a) S2p ;(b) Cl2p spectra of F2050............................ 182

Figure 72 Photodegradation of methylene blue catalysed by F2029 and F2030: (a) Weight concentration changed versus time; (b) Weight concentration ratio changed versus time. Both samples show high adsorption ability, which removed ~60% of methylene blue. However, their photocatalytic ability was poor. 183

Figure 73 Photodegradation of methylene blue catalysed by F2037 II, F2041B, and F2050: (a) Weight concentration changed versus time; (b) Weight concentration ratio changed versus time. F2037 II shows the highest adsorption ability among the three samples. However, no sample has shown a high degradation ability. 185

List of Tables

Table 1 Structural parameters of trititanate nanotube[68] (Table reprinted with the permission of ACS, ref 68) 43

Table 2 CHN Elemental Analysis of modified TiNT samples 85

Chapter 1: Introduction

1.1 Background

Energy issues and environmental pollution are challenges in the 21st century. The current energy supply is heavily based on fossil fuels, with carbon dioxide production, which further results in climate change and global warming. Thus, people seek new and renewable energy sources such as wind energy, hydro energy, hydrogen energy, and solar energy to rebuild energy structures. These kinds of energy are clean and green because of low pollution. In the meantime, the pollution issue is becoming more and more severe due to the discharge of waste gas and wastewater. Waste gas usually contains fine particulate pollutants such as PM2.5 and gas pollutants such as SO_2 and NO. These pollutants can cause significant damage to the human respiratory system.

What is more important, water pollution has become a significant concern because the lives of living beings can be directly affected by the quality of water resources.[1] In particular, industrial wastewater can cause significant environmental damage and endanger human life. For example, the Minamata disease event in the 1950s caused severe mercury pollution. These events occurred because industrial waste water contains many hazardous pollutants, including heavy metals, pesticide residues, and some other organic pollutants like organic dyes that can hardly be degraded. In particular, organic dyes, as one kind of organic pollutants, are widely used in many industrial fields, such as ink, plastic, textile, cosmetics, and textile.[2] It was estimated that the annual amount of discharged textile dyes is around 280,000 tons.[3] To avoid water pollution caused by dyes, the discharge and treatment of dye-polluted wastewater are strictly controlled in many countries.

Ideally, the techniques to remove organic pollutants, including dyes, should be efficient, inexpensive, and green. In addition, all reagents, energy sources and catalysts for removal uses should be inexpensive, abundant, and environmentally friendly.[4] The mainstream techniques to remove organic pollutants from waters and wastewaters are conventional biological and physical treatments, such as coagulation, adsorption, and ultrafiltration.[4] However, these methods merely transfer dye from water to solid, and further treatments are necessary.[2] Thus, the main drawbacks of these techniques are high cost, the difficulty of recycling, and secondary pollution. Besides these techniques, oxidation of organic pollutants, which converts organic pollutants into CO_2 and water, is also widely applied. The burning method is a typical oxidation technique, and usually, the oxidant is oxygen from the air. However, in practice, most organic pollutants are stable under room temperature and can release secondary pollutants if the pollutants are not completely burnt. As a result, the pollutants must be pre-treated, primarily involving classification and concentration. In addition, a very high temperature is required to activate the oxidation reaction, and specific equipment is necessary to control secondary pollution. As a result, the cost of the combustion method is high when minimizing pollution, thus limiting its application.

1.2 Photodegradation Mechanism

As an oxidation technique, photodegradation is an attractive option for removing organic dye pollutants due to its reusability, environmental friendliness, and low cost. The mechanistic pathways and reaction equations of photodegradation are described below in equations (1)-(8).[1, 4] When a semiconductor is under illumination with light of higher energy than the band gap, electrons are promoted from the valence band (VB) to conduction band (CB), and thus electron-hole pairs are produced. The produced electrons in the conduction band (e_{CB}^-) and the produced electron vacancy in the valence band (h_{VB}^+) could migrate to the catalyst surface, where redox reactions can occur with other species.[1] For photodegradation occurring in water, water and oxygen are adsorbed on the catalyst surface. The h_{VB}^+ can react with water to produce hydroxyl radicals ($^{\cdot}OH$) or oxidize the dye molecules directly. On the other hand, e_{CB}^- can react with O_2 to produce superoxide radical anions ($O_2^{-\cdot}$) or reduce the dye molecules directly. The superoxide radical anions can further react with water to produce peroxide and then produce hydroxyl radicals. The hydroxyl radicals can degrade organic dye molecules to smaller organic molecules, and finally, degrade them to H_2O and CO_2. The overall reaction is shown in equation (8). The photocatalyst is not consumed during the photodegradation process, and the only external energy source is light energy. Dyes are usually used in photocatalytic degradation processes as probe molecules because their concentrations are easy to measure.

$$H_2O + h_{VB}^+ \rightarrow {}^{\cdot}OH + H^+ \qquad (1)$$

$$O_2 + e_{CB}^- \rightarrow O_2^{-\cdot} \qquad (2)$$

$$O_2^{-\cdot} + H_2O \rightarrow H_2O_2 \qquad (3)$$

$$H_2O_2 \rightarrow 2{}^{\cdot}OH \qquad (4)$$

$${}^{\cdot}OH + dye \rightarrow dye_{ox} \qquad (5)$$

$$e_{CB}^- + dye \rightarrow dye_{red} \qquad (6)$$

$$h_{VB}^+ + dye \rightarrow dye_{ox} \qquad (7)$$

$$\text{Overall:} \quad dye + O_2 \xrightarrow[\text{Photocatalysts}]{\text{UV}} H_2O + CO_2 + \text{inorganic species} \qquad (8)$$

1.3 Factors affecting photodegradation

1.3.1 pH

The photocatalytic dye degradation efficiency is influenced by many factors, and pH is one of the significant factors.[5] Since catalyst surface charge is highly dependents on the pH of the solution,[6, 7] dye adsorption onto the catalyst surface can be promoted or hindered by adjusting pH values and thus influencing the photodegradation rate. The pH value is also related to the mechanism and affects the degradation rate. Under low pH, the h_{VB}^+ is the primary oxidant to oxidize the dye, but under neutral or higher pH, hydroxyl radicals become the major oxidation species.[8] Generally, high pH values have been found to lead to better photocatalytic degradation of cationic form pollutant molecules, while molecules with negative charges are degraded to a higher degree at low pH values.[9] For example, the removal of an anionic dye named reactive orange 4 (Figure 1(a)) at pH=9 was six times as high as that at pH=1, and this was explained by TiO_2 agglomeration and decreasing of hydroxyl radicals at low pH.[10] However, conflicting results have been reported as well; for example, chromotrope 2B (Figure 1(b)) and amido black 10B (Figure 1(c)) are anionic dyes, but they have shown maximum degradation at pH=9 under photocatalysis by titanium dioxide.[11] It was proposed that with increasing concentration of OH^-, the generation of hydroxyl radicals by TiO_2 was promoted.[11]

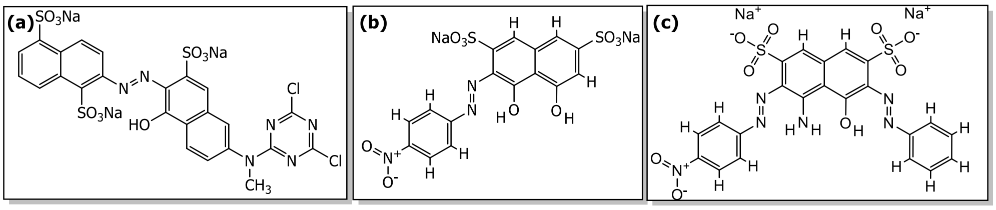

Figure 1 Structures of (a) Reactive Orange 4; (b) Chromotrope 2B; (c) Amido Black 10B. They

are anionic dyes and the degradation rates of them are sensitive to pH values.

For methylene blue (MB) (the structure is shown in Figure 2), it has been reported that, at a low pH, the adsorption of cationic MB was reduced because of the competition with excess H^+ ions, and at a high pH, the adsorption of cationic groups of MB was reduced as well due to the strong attraction to OH^- ions.[12] The aqueous MB solution is weak alkaline, which is within the proper range of photodegradation.

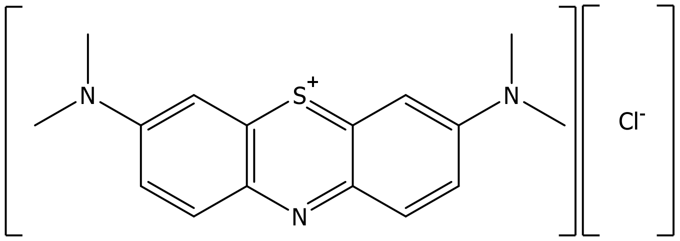

Figure 2 Structure of Methylene Blue, which is a cationic dye and its aqueous solution is weak alkaline.

1.3.2 Photocatalyst Adsorption and Load Amount

The adsorption of water and dye molecules on photocatalysts is another crucial factor that influences the photodegradation efficiency because the photodegradation process occurs on the photocatalyst surface. As shown in the above mechanism equations (1)-(8), the initial photogenerated species react with water or dye on the catalyst surface. The generated radicals do not have to migrate to solution if they can react with surface adsorbed molecules, and the electron-hole pairs are not long-lived; therefore, their recombination can be prevented if the adsorption of dye molecules is rapid. [13]. As a result, the degradation rate increases when the adsorption becomes higher. It was reported that by increasing the load amount of photocatalyst, the photodegradation rate increases correspondingly.[14, 15] However, when the photocatalyst load amount exceeded a specific number, which was 2.5 g/L when degrading reactive blue 4 (RB4) assisted by titanium dioxide, the increment of degradation rate was small, and the final degradation ratio did not increase anymore.[14] In another research, the degradation rate was highest when the load amount reached 1g/L.[13] There are three possible explanations for this phenomenon. Firstly, the addition of photocatalyst can be excess if all dye molecules are adsorbed by photocatalyst.[5] This may hinder the interaction between the catalyst and excited dye molecules or incoming light.[5] Secondly, when the number of photocatalyst particles increases, the interaction between particles becomes significant, and this results in the reduction of site density for holes and electrons on the surface.[16] Thirdly, at higher photocatalyst loading, the opacity of suspension increases and thus, the effective light intensity may decrease.[16] As a result, the reaction rate decreases when the adding amount of photocatalyst is too high.

In this project, the adsorption abilities of samples were compared by measuring

UV-Vis absorbance of the liquid system, and the adsorption ratio was calculated by the changes of absorbance divided by the initial absorbance of the dye solution. The adding amount of photocatalyst was controlled at 0.1 g/L for all the photodegradation measurements for giving comparable results.

1.3.3 Light Source

Due to the characteristic of semiconductors, light can only be utilized if its energy is higher than the band gap of the material. It has been reported that the photodegradation rate of acid orange 7 (AO7) on TiO_2 was higher under UV light compared to visible light when two 6 W UV lamps and a 175 W metal halide lamp were used as UV light source and visible light source, respectively.[17] Even the visible light source has higher total power, the UV lamp resulted in a higher photodegradation rate. Research in 1992 compared the degradation of phenol by TiO_2 under a 100 W mercury lamp and sunlight from a clear sky and sunlight resulted in a higher photodegradation rate.[18] The main reason is the photocatalyst TiO_2 has a large band gap that it can only utilize UV light. Therefore the output power of the lump is not equivalent to the effective light intensity of illumination. In this project, photodegradation of methylene blue solution by samples was measured under a 300W Xenon lamp for simulating full-range light illumination, and a 400 nm cut-off filter was applied for simulating visible light illumination, and the results were compared.

1.4 Removal of Methylene Blue

Methylene blue (MB) (its structure is shown in Figure 2 in the previous section) was the first synthetic drug in history and has been used for about 130 years.[19] Nowadays, methylene blue is also widely used as a dye for silk, cotton and wood.[20, 21] As a strong coloured dye, the presence of methylene blue is obvious in water even if the amount is very small; thus, the methylene blue in waste water is undesirable. Figure 3 shows the colours of MB solutions with different weight concentrations from left to right: 1 g/L, 100 mg/L, 10 mg/L, and 1 mg/L.

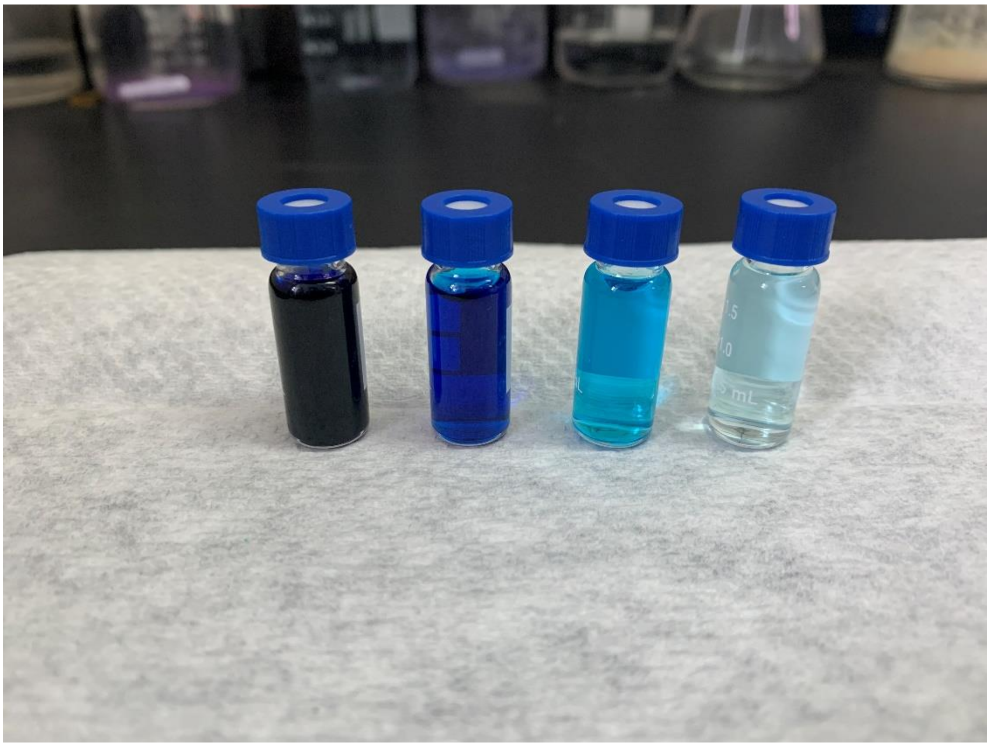

Figure 3 The colours of MB solutions with different weight concentrations from left to right: 1 g/L, 100 mg/L, 10 mg/L, and 1 mg/L. The blue colour of MB is still significant under low concentration.

In addition, methylene blue is harmful, although it is not strongly hazardous.[22] Therefore, methods for removing as much methylene blue in aqueous solutions as possible have been investigated. The adsorption method has been preferred due to its capability and simplicity for waste water treatment.[21] Many materials have been reported to show high adsorption ability for methylene blue, such as activated carbon[20], carbon nanotubes[23], as well as TiNT and modified TiNT[24].

Besides being a model dye in adsorption researches, methylene blue is also used as a probe molecule in photodegradation. Methylene blue has a high molar attenuation coefficient ($\varepsilon_{660} = 10^5$ $dm^3mol^{-1}cm^{-1}$)[25, 26] with maximum absorbance at around 660 nm. Its singly reduced form is pale yellow, and it can readily form a doubly reduced form of MB, *leuco*-methylene blue, which is colourless[19, 26, 27]. It is also reported that oxidized methylene blue has a maximum absorbance at around 520 nm.[26] In brief, methylene blue can easily change/lose colour during redox reactions and can be simply measured by UV-Vis absorbance. Photodegradation is a redox process, and methylene blue is commonly used[26, 28-30] to indicate the removal progress as a probe molecule. Recent research has reported that g-C_3N_4/TiO_2 film can enhance the photodegradation of methylene blue.[31] Because TiNT is made from TiO_2 and has shown high adsorption[24, 32], which is beneficial to photodegradation, the photodegradation ability of TiNT was improved by forming a composite with g-C_3N_4 in this project.

1.5 Research Scheme

In this research, TiNT was firstly synthesized from TiO_2. Next, several commercial organic compounds which contain a catechol sub-structure were attached to the TiNT surface, based on the proposed TiNT-dopamine binding models[33]. The resultant TiNT-catechol structures were investigated using several techniques, including solid-state NMR, UV-Vis, FTIR, TEM and Raman.

During the measurement of Raman, selective SERS was found to be related to the structures of the catechol modifiers. This phenomenon was further investigated and discussed in Chapter 4: surface enhanced Raman scattering. Research of g-C_3N_4-TiNT composite started from electrostatic adherence under room temperature. Upon annealing the samples, it was found that the photodegradation ability of samples had improved. This phenomenon was further investigated and discussed in Chapter 5: C_3N_4-TiNT nanocomposite. The synthesis of the TiNT-organic-AuNP system started from the synthesis of AuNPs and organic compounds, respectively, followed by combining TiNT, organic compounds (as linkers) and AuNPs into TiNT-organic-AuNP system (target structure is shown in Figure 4). The characterization and properties of this system were further discussed in Chapter 6: AuNP-Organic-TiNT Composites and Organic Synthesis.

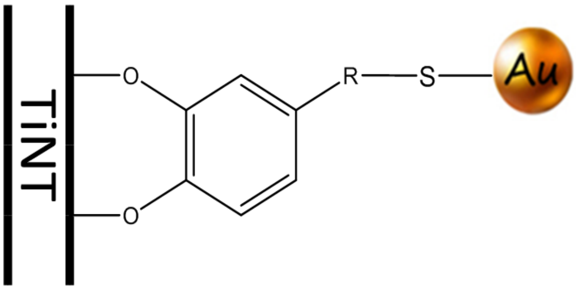

Figure 4 Target structure of TiNT-organic-AuNP system. Organic linkers are attached to TiNT surface by catechol structure and attach to AuNPs via free thiol group.

1.6 Chapters Summary

In Chapter 1, the general background of this research was introduced, the mechanism of photodegradation was explained, the key factors that affect photodegradation were discussed, and the basic background and removal of methylene blue were introduced. In addition, the scheme of this research and the chapters were summarized. Chapter 2 is a literature review that contains three sections. The first section reviewed TiO_2 and trititanate nanotubes as photocatalyst, including the background, history, properties, and applications as photocatalyst. The second section reviewed graphitic carbon nitride as photocatalyst, including the properties, applications as photocatalyst, and modification methods. The third section reviewed gold nanoparticles, surface plasmon resonance effect, and metal plasmonic-semiconductor heterojunctions. These three sections reviewed three main materials that were used and investigated in this thesis. In Chapter 3, instrumentation, information of all used instruments was introduced. Principles of primary instrumentation were discussed. Sample preparation and analysis methods were also introduced. In Chapter 4, surface enhanced Raman scattering by TiNT-catechol systems was reported and discussed. TiNT-catechol systems were synthesized, characterizations of these systems were measured and analysed and discussed. Chapter 5 is the C_3N_4-TiNT nanocomposite, which combined two semiconductors, and achieved high photoactivity and high adsorption abilities toward removing methylene blue. The characterizations of C_3N_4-TiNT nanocomposites were measured and discussed. In Chapter 6, AuNP-Organic-TiNT composites were synthesized by the surface modification of TiNT using organic linkers and the addition of AuNPs. The synthesized systems' characterizations were discussed, and their photoactivity towards photodegradation of methylene blue was tested. In this chapter, several organic compounds were synthesized and analysed as well. Chapter 7 is a summary of this thesis and an outlook of future work.

Chapter 2 Literature Review

2.1 TiO_2 and Trititanate Nanotubes as Photocatalyst

2.1.1 TiO_2

TiO_2 is a natural oxide of titanium. It is not only inexpensive, harmless, and chemically stable[34, 35], which makes it suitable for pigment and cosmetics, but also has appropriate chemical properties to show great potential in water splitting[36-38], environmental decontamination[39-41], fuel cells[42, 43], solar cells[44-46], and energy storage devices[47-49]. TiO_2 is normally described to have three polymorphs that are found in nature: rutile, anatase, and brookite. Rutile and anatase play important roles in industry, while the rareness and preparation difficulty of brookite limits researches related to it.[50] The crystal structures of rutile, anatase, brookite are shown in Figure 5[51]. All of the three polymorphs have distorted TiO_6 octahedra, in which titanium cations are coordinated to 6 oxygen atoms. Anatase structures are formed by sharing the octahedral edges, when the rutile and brookite frameworks contain both corner-sharing and edge-sharing configurations.[50, 51]

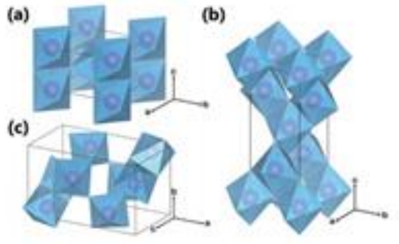

Figure 5 Crystal structure of (a)rutile; (b)anatase; (c)brookite. Blue octahedral stands for TiO_6 blocks and purple spheres stand for Ti atoms.[51] They have distorted TiO_6 octahedra, in which titanium cations are coordinated to 6 oxygen atoms. (Figure reprinted with the permission of RSC, ref 51)

The photocatalytic properties of TiO_2 were first discovered and reported by Fujishima and Honda in 1972.[52] During the 1970s, the demonstration of hydroxyl radical formation[53] and metal ion reduction[54] on TiO_2 surface were investigated. A scheme of the photocatalysis mechanism of TiO_2 is shown in Figure 6. As a semiconductor photocatalyst, when the material is irradiated by light, the electrons (e^-) from the valence band of the TiO_2 surface are activated to the conduction band and leave positive electron holes (h^+) in the valence band. The activated electron-hole charge carriers can recombine and undergo charge annihilation. When they migrate to the surface of the catalyst and do not undergo charge annihilation, secondary reactions with the surface adsorbed materials are initiated.[55] The excited electrons in the conduction band are reductive, and the holes are oxidative. The products of the redox reactions can take part in the degradation of organic pollutants.

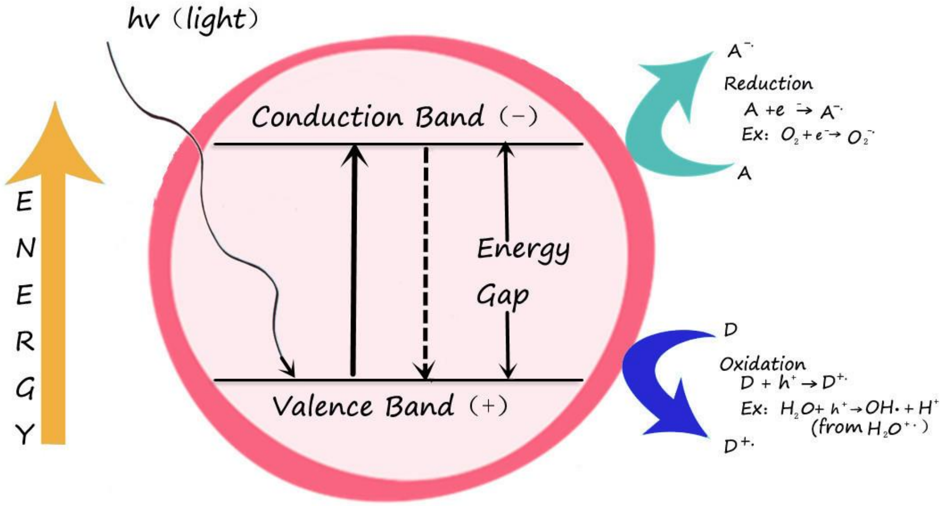

Figure 6 Photocatalysis mechanism of TiO_2. Electrons are excited to conduction band under light illumination and participate in reduction. Holes are left in the valence band and participate in oxidation.

The main drawback of TiO_2 as a photocatalyst is its large band gap, which is 3.2 eV for anatase and 3.0 eV for rutile. The relevant wavelength of light is calculated by the following equation (9), where E is photon energy, h is the Planck constant, c is the speed of light in vacuum, and λ is the wavelength. The band gap of anatase TiO_2, which is 3.2 eV, corresponds to 388 nm. That means TiO_2 can only be activated by UV light, which is less than 5% in the solar spectrum. As a result, the applications of TiO_2 photocatalysts are limited. There are many ways to increase the optical activity, including doping, sensitizing TiO_2 with colourful compounds, and surface modification of TiO_2 nanomaterials with another semiconductor.[56]

$$E = hc/\lambda \tag{9}$$

Surface modification is a mild, efficient, and sustainable method to improve the photoactivity of TiO_2 through light harvesting and electron transfer for charge separation.[24, 57] TiO_2 is modified based on its uncoordinated surface sites by the attachment of compounds with specific structures like dopamine, which act as ligand.[58] TiO_2 can be made into the trititanate nanotube (TiNT), which was reported to have a high surface area and a porous structure.[32]

2.1.2 Trititanate Nanotubes

Compared to TiO_2 itself, the tubular form of TiO_2 has attracted attention and become important due to its larger surface area and higher photocatalytic activity[59]. Among the nanotubes prepared from TiO_2, trititanate ($H_2Ti_3O_7$) nanotube has attracted researchers because it can be easily prepared by hydrothermal methods from TiO_2.[60, 61] The preparation of TiNT was first reported by Kasuga *et al.* in 1998 by hydrothermal treatment of TiO_2 with 10 M NaOH solution[62], and this hydrothermal method was latterly improved by other researchers.[32, 63] Other methods of preparing nanotubes from TiO_2 were also reported, such as the chemical templating method[64] and the electrochemical oxidation method.[65] The former method usually contains the following procedures[64, 66]: firstly, under the help of template agents, solutions that contain titanium undergo controlled sol-gel hydrolysis. Then TiO_2 deposits onto the surface of template aggregate or polymerise in the template molecules. Finally, the templating agents are removed. The latter method was firstly reported by Grimes *et al*. in 2001.[65] In this method, titanium foil was anodised in an H_2O-HF electrolyte directly and self-organised TiO_2 nanotubes were prepared. Compared with these methods, the hydrothermal method only involves simply heating and washing processes by non-toxic reagents like NaOH and HCl, so this method was mainly used in this project.

The formation mechanism of trititanate nanotubes by hydrothermal synthesis was explained by researchers as follows[63]: firstly, in the early stage, TiO_2 reacts with NaOH and a highly disordered phase forms. Then this disordered phase is recrystallized into thin plates which have only a few layers in thickness. Next, individual trititanate layers are peeled off from the plates. Finally, all the plates scroll to nanotubes after three days of reaction. Surface tension is the main driving force of the cleavage, and this surface tension together with Coulomb force as well as interlayer coupling control the formation and dimension of the nanotubes.

Compared to TiO_2, TiNT has a higher surface area, and it is more easily modified. TiNT shows a similar band gap (3.2 eV) to TiO_2, which means it can only be driven by UV light and modification of TiNT for improving its photoactivity under visible light is necessary. Titanium and oxygen can be detected from TiNT by energy-dispersive X-ray spectroscopy (EDX), which is the same as TiO_2; however, the structure profile of TiNT is different from that of TiO_2, and thus X-ray diffraction is helpful to distinguish them. Unlike the three dimensional structure of TiO_2, the trititanate has a layered structure with a monoclinic structure (a=1.603, b=0.373, c=0.919 nm and β=101.45°)[67], and its structural parameters of TiNT are shown in Table 1[68]. What is more, it was reported that structural transformation could occur following the sequence: titanate →monoclinic TiO_2 (B) →anatase[69, 70] under heating when TiO_2 (B) acts as an intermediate product. Figure 7[69] illustrates the transformation sequence during the thermal treatment of protonated titanate nanotubes.

Table 1 Structural parameters of trititanate nanotube[68] (Table reprinted with the permission of ACS, ref 68)

$H_2Ti_3O_7$ (data from JCPDS 47-0561 monoclinic)

d	*h*	*k*	*l*
7.87	2	0	0
3.65	1	1	0
3.05	3	1	0
2.67	3	1	-2
2.37	1	1	3
1.88	0	2	0

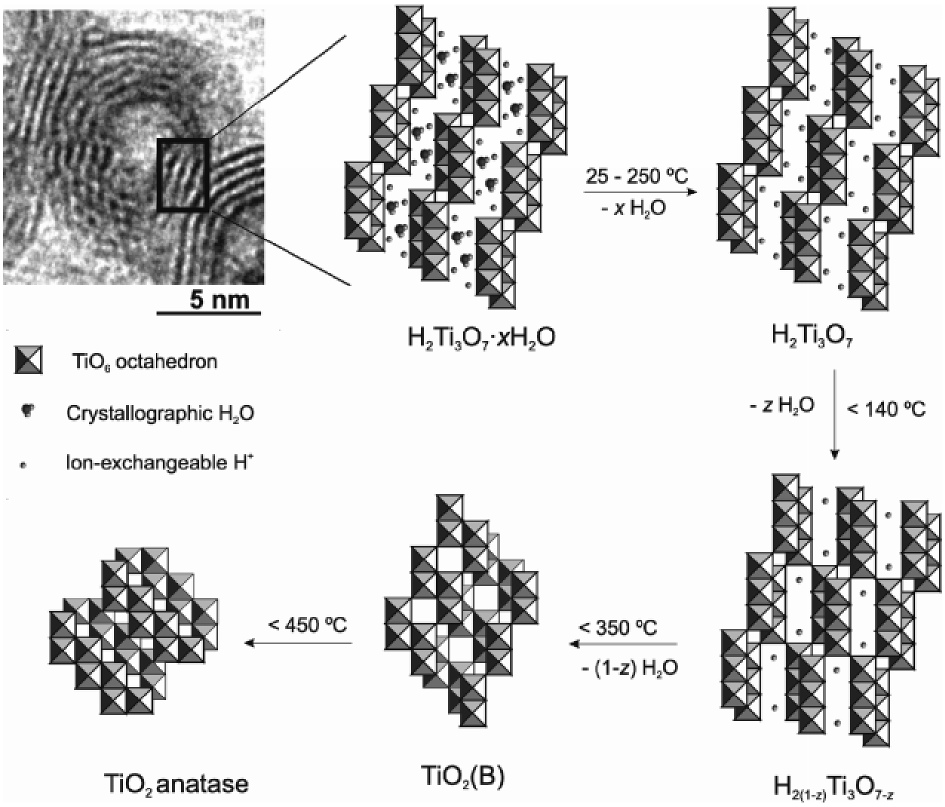

Figure 7 Structural and morphological transformation of a protonated titanate nanotube during thermal treatment.[69] Titanate can transform to monoclinic TiO_2 (B) at <350 °C by loss of water and finally to TiO_2 anatase at <450 °C. (Figure reprinted with the permission of ACS, ref 69)

TiNT has shown its potential applications in many fields due to its high surface area, elongated morphology and semiconductor properties.[66] TiNT and modified TiNT were applied for energy storage[71, 72] and used as a catalyst for organic reaction[73], adsorbent[24, 32] and photocatalyst[24, 74]. As a catalyst for organic synthesis, it was reported that Cu_2O nanoparticles supported TiNT can catalyse the synthesis of 1,2,3-triazoles under mild conditions and highly improve the yield of product compared with Cu_2O itself and common catalyst

CuI.[73] TiNT with high adsorption capacity (58 mg/g) was reported to adsorb nearly 95% of fluoride in a short time at low pH and this phenomenon was explained by abundant hydroxyl groups on TiNT surface, the high surface area of TiNT, ion-exchange between fluoride and hydroxyl groups and electrostatic attraction.[75] TiNT were also reported to be able to strongly adsorb dyes in an aqueous solution due to the high surface area and porous structure of the nanotubes.[32] Besides TiNT itself, modified TiNT was also reported to show high adsorption capacity. In 2012, trititanate nanotubes with high adsorption capacity towards methylene blue dye were prepared through self-assembly surface modification with dopamine molecules.[24] This research suggests the possibility of surface modification with specific molecules by self-assembled and improvement of photoactivity. By further investigating the TiNT-dopamine system, two models for self-assembled dopamine on the surface of trititanate nanotubes were proposed, including monomer units linked through π-π stacking, and mono-attached interacting by hydrogen bonds.[33] It is expected to achieve high adsorption and high photodegradation of methylene blue through the surface modification of TiNT.

2.2 Graphitic Carbon Nitride as Photocatalyst

Graphitic carbon nitride (g-C_3N_4) is a metal-free polymer n-type semiconductor that only contains carbon, nitrogen, and hydrogen. g-C_3N_4 contains graphitic stacking of C_3N_4 layers, which is consist of tri-*s*-triazine units connected by planar amino groups. The structure of g-C_3N_4 is shown in Figure 8.

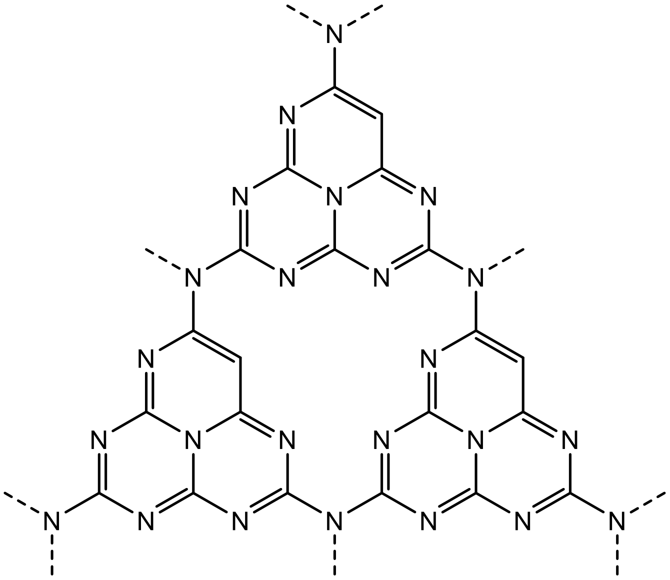

Figure 8 Structure of g-C_3N_4: consist of tri-*s*-triazine units connected by planar amino groups.

g-C_3N_4 has shown good chemical stability that can work under strong acid and base, and this has been attributed to the strong covalent bonds.[76] It also has high stability under light irradiation, and it is environmental-friendly. It shows many promising properties, such as unique electric and optical properties, which have made g-C_3N_4 based materials become a new nanoplatform for energy, electronic, and catalytic applications.[77, 78] The band gap of g-C_3N_4 is 2.7

eV, which means it can absorb light with a wavelength smaller than 460 nm and makes g-C_3N_4 able to absorb visible light. Moreover, the conduction band and valence band edge of carbon nitride were reported as -0.8V and 1.9V, which was theoretically suitable for photo redox of surface adsorbed water of semiconductor.[79, 80] The g-C_3N_4 was firstly reported as a photocatalyst for producing hydrogen from water in 2009.[81] After that, g-C_3N_4 applied in photoreactions has attracted increasing interest, and the potential applications of g-C_3N_4 in water splitting and photodegradation were further investigated.

However, it was reported that the efficiency of water splitting of g-C_3N_4 is low, which was caused by low surface area and high recombination rate of photo-generated electron-hole pairs.[81] It was also reported that the electrical conductivity and localized excitons of g-C_3N_4 are poor due to its structural defects, which leads to the low activity of interfacial electron transfer reaction, and the transformation of adsorbed oxygen toward active oxygen radicals is hindered.[82, 83] There are several approaches to improving the performance of g-C_3N_4 photocatalyst: metal ion doping such as zinc doping[84] and Fe doping[85]; non-metal doping such as O[86], S[87] and P[88]; noble metal doping like Au[89]; semiconductor coupling with g-C_3N_4 like polymer semiconductor[90], ZnO[91, 92] and TiO_2[93-95]. These modifications work through enhancing visible-light absorption, accelerating surface reaction kinetics, inhibiting the charge recombination, and improving charge separation efficiency.[76, 96]

g-C_3N_4 can be easily synthesized via a one-step polymerization process, which only uses cheap nitrogen-rich starting material like urea, thiourea, melamine, cyanamide, and dicyandiamide.[81, 97, 98] For example, simply heating urea in a furnace under 550 °C for 4 hours can give g-C_3N_4 without further treatment. This makes g-C_3N_4 possible to be mass-produced in factories at a very low cost. The mechanism of the reaction pathway of g-C_3N_4 from urea, thiourea, dicyandiamide and melamine is shown in

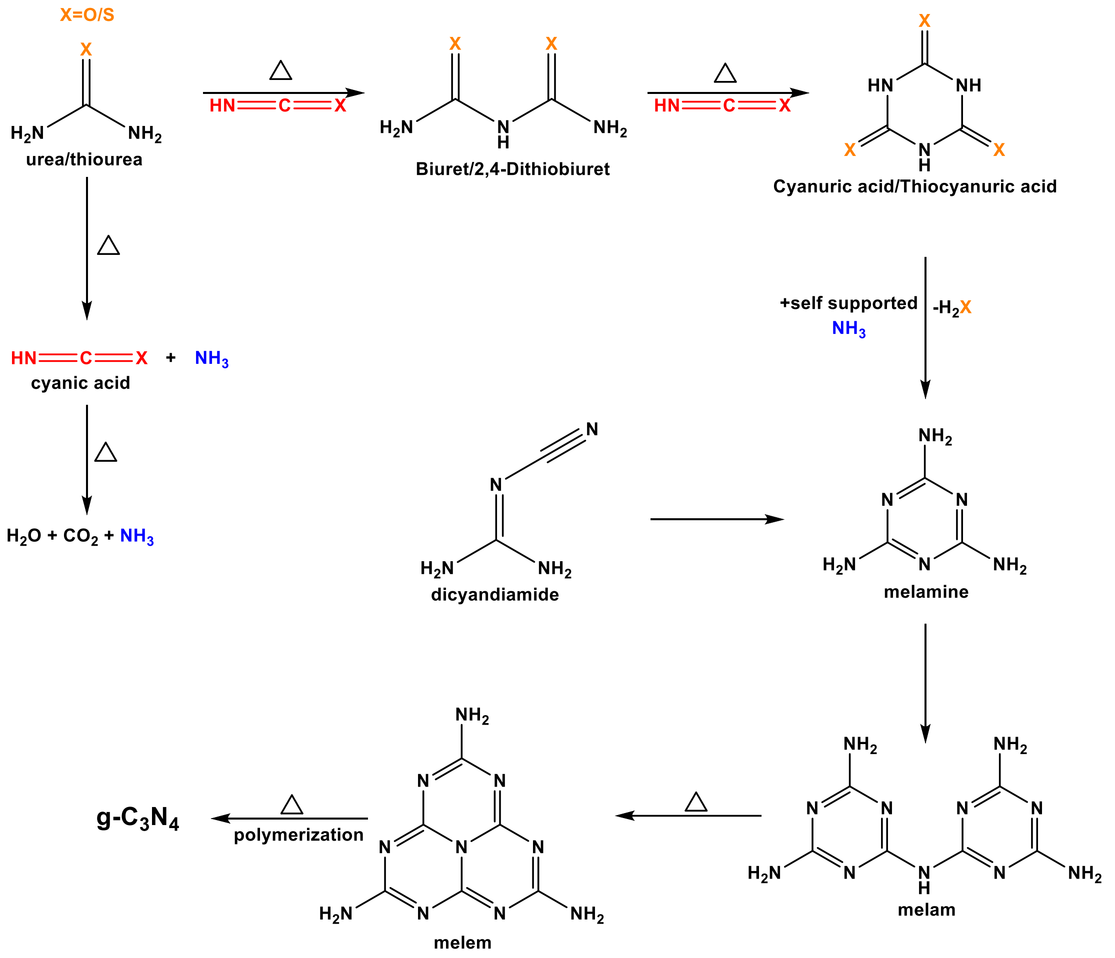

Figure 9.[97] Take urea as an example, an ammonia molecule is firstly lost under heating, and isocyanic acid forms; isocyanic acid then reacts with urea to form biuret; next, nucleophilic addition occurs between biuret and urea to form rings. Then this structure reacts with ammonia and forms melamine. Through heating, the intermolecular reaction of melamine results in melam and the intramolecular of melam give melem. Finally, the melem polymerized to g-C_3N_4. Although different precursors undergo a similar reaction process, the resulting g-C_3N_4 shows a slight difference in chemical activity. Yuewei *et al.*[97] have reported that g-C_3N_4 prepared from urea has a higher surface area due to its low polymerization and results in higher efficiency. This is because of the stronger C=O bond in urea compared to the C=S bond in thiourea and the stronger electronegativity of the O atom.

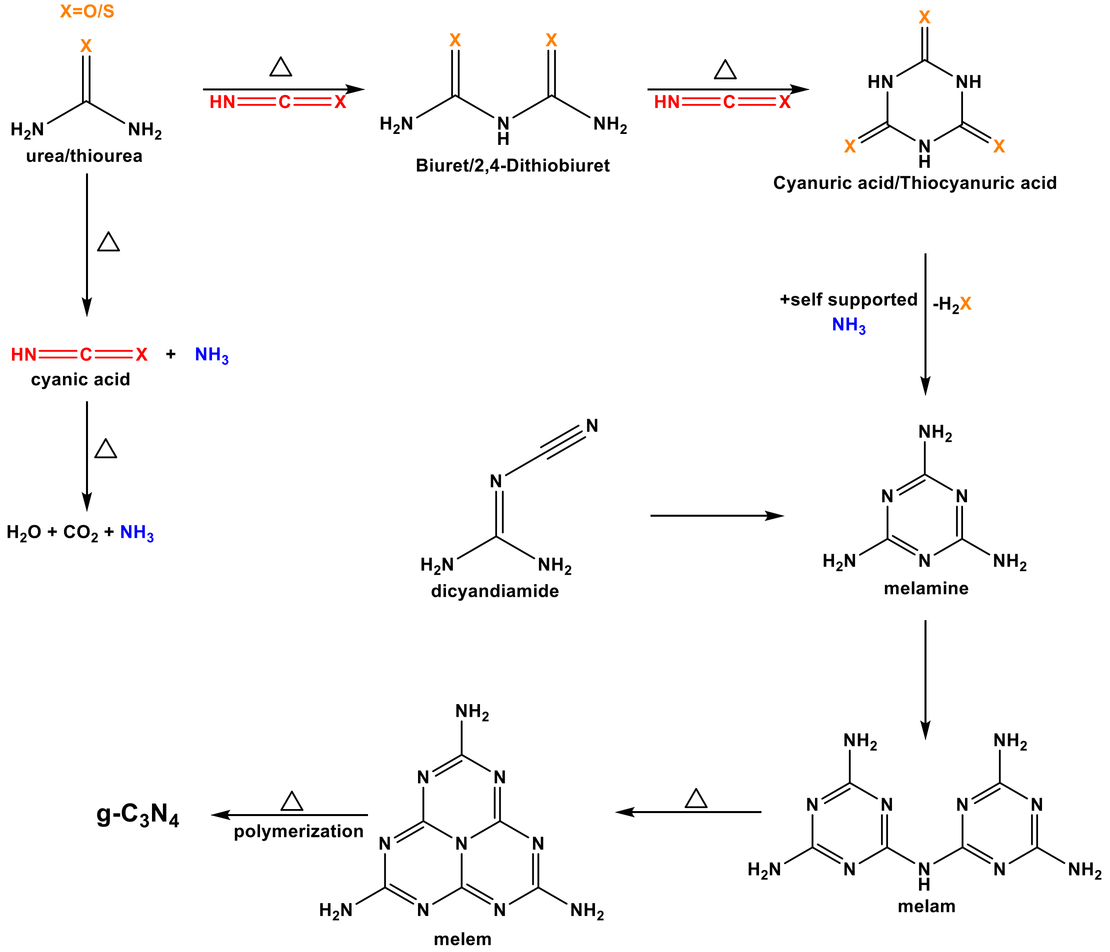

Figure 9 Reaction pathway of g-C_3N_4[97] from different precursors including urea, thiourea, dicyandiamide and melamine to melam, melem and finally g-C_3N_4. (Figure reprinted with the permission of RSC, ref 97)

2.3 Gold Nanoparticles and Surface Plasmon Resonance

Gold nanoparticles can induce SERS because of surface plasmon resonance.[99] Surface plasmon resonance (SPR) is described as the resonant, collective oscillation of valence electrons in a solid that is stimulated by incident light.[100] The basic principle of SPR is explained as follows: On one side, under a condition of total internal reflection, at the interface, an evanescent field (standing wave) will penetrate the exit medium.[100] On the other side, in analogy to a real plasma, plasmons can be described as an electron cloud with negative charges that are coherently displaced from its equilibrium position around a lattice, which is made of positively charged ions.[101, 102] For a metal nanoparticle like a gold nanoparticle, although it is electrically neutral, it can be considered as a plasmon. When excited by electromagnetic radiation, including light, a coherent oscillation of the surface conduction electrons occurs.[103] At a specific wavelength, the resonance of standing wave and oscillation of surface electrons could happen. This resonance is called surface plasmon resonance. When there is SPR, the reflection of the resonance wavelength of the incident light will reduce dramatically.

Localized surface plasmons (LSPs) are the plasmons in nanoparticles with sizes that are much smaller than the wavelength of the incident light, which are nonpropagating excitations because the resulting plasmon oscillation is distributed over the whole particle.[101, 104] Figure 10 is a schematic of a localized surface plasmon.[103] As metal nanoparticles, gold nanoparticles can undergo localized surface plasmon resonance (LSPR) under incident light. In the last two decades, plasmon resonance in gold nanoparticles has been a popular research subject. It has been reported that the LSPR peaks of gold nanoparticles are strongly related to their shape, size, and dielectric constant of the surrounding medium[105].

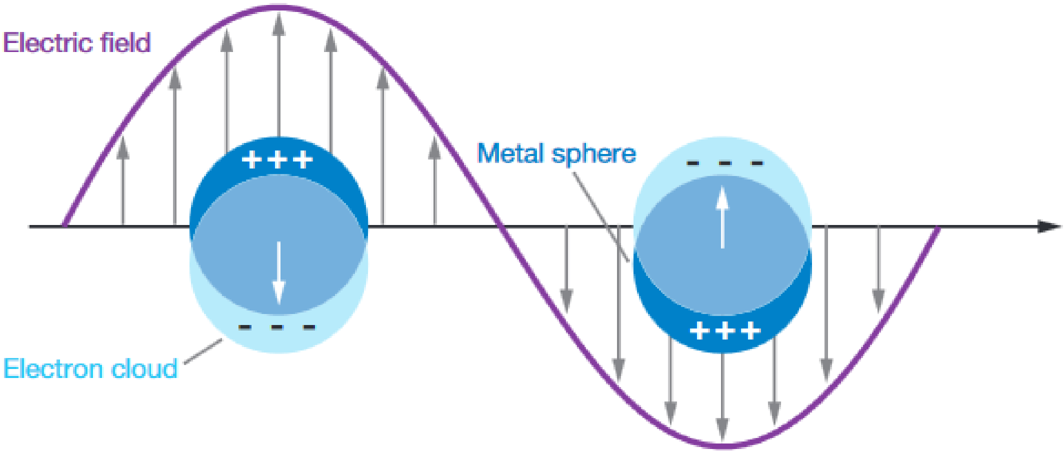

Figure 10 A schematic of a localized surface plasmon[103] (Figure reprinted with the permission of ANNUAL REVIEWS, ref 103)

The activity of photocatalysts can be improved by the formation of heterojunctions by coupling plasmonic nanostructures with semiconductors, and plasmonic can act as light antennas for extending the light absorption range of semiconductors.[106] There are three main mechanisms of the energy transfer from a plasmonic metal to a semiconductor: plasmon-induced resonance energy transfer (PIRET), light scattering/trapping, hot electron injection.[106] PIRET mechanism explained that dipole could be generated by the excitation of plasmons, then the plasmonic energy can be transferred to the semiconductor through dipole-dipole interaction, and electron-hole pairs are generated.[107, 108] The efficiency of PIRET is highly related to the spectral overlap between the absorption band of semiconductor and the plasmonic resonance band, and the distance between metal and semiconductor.[106] Light scattering/trapping mechanism explained that the incident light could be scattered by metal nanoparticles in the metal-semiconductor heterojunction systems.[109, 110] The scattering effect is also called 'light trapping' due to its enhancement in charge separation and light absorption, and this effect only works when the energy of scattering photons is larger than the semiconductor's band gap.[106] Hot electron injection explained that hot carriers could be generated by the non-radiative dissipation of plasmon energy, and the hot electrons that have higher energy than the Schottky barrier at the metal-semiconductor interface can be directly injected into the semiconductor's conduction band.[111, 112] Compared to the photogenerated electrons via inter-band transitions, the hot electrons from plasmonic metal could have a lower charge recombination and higher thermodynamic driving force.[106]

In this project, TiNT-AuNPs systems were designed, and several organic compounds were synthesized as linkers between gold nanoparticles and TiNT. Gold nanoparticles were used to help harvest visible light, and the controlled size of gold nanoparticles was expected to adjust the wavelength of absorbed visible light to boost photocatalysis. It was expected that the photoactivity of TiNT could be improved by forming a plasmonic-semiconductor system.

Chapter 3 Instrumentation

3.1 Instrumentation Information

UV-Vis absorbance spectra were recorded using Cary 300 UV-Vis for solid samples and Cary 60 UV-Vis for liquid samples. ^{13}C solid-state NMR spectra were measured on a Bruker Advance III 400 spectrometer equipped with a 4 mm H/X DVT probe. Liquid NMR was recorded on an Ascend^{TM} 400 MHz NMR produced by Bruker. FTIR was measured on a Cary 660 FTIR. CHN Element Analysis was measured on an Elementar Vario MACRO CHNS. Powder X-ray diffraction was recorded on a Bruker D8 advance diffractometer with Cu Kα at 40 kV and 40 mA. Transmission electron microscope (TEM) images were carried out on an FEI Tecnai F20 operating at 200 kV. Raman measurements were made using HORIBA Scientific XploRA. A 785 nm laser was used for excitation. Typical spectra acquisition parameters were: laser: 785nm; Filter: 100%; Hole: 300; Slit: 100; Grating: 1200T; RTD exposure time: 1s; Exposure time: 5s; Accumulation number: 3. Experiments were repeated several times on the same sample, and the spectra shown were representative and reproducible. Zeta potential was recorded on a Malvern Zetasizer Nano. X-ray photoelectron spectroscopy was recorded on an ESCALAB 250 XI. GC-MS was recorded by a 5975 C produced by Agilent Technologies. Mass spectra were recorded on a microTOF-Q II produced by Bruker. Heating and annealing processes were carried out in a muffle furnace (model 4-10 TP) produced by Shanghai Huitai Equipment Manufacturing Co., Ltd. An oven produced by SENXIN (model DGG-9030AD) was used for normal drying. Centrifuging was carried out in a Sigma 1-14 centrifuge. A Xenon light PLS-SXE 300D purchased from PerfectLight was used as the light source. Light intensity was measured by a PL-MW2000 photoradiometer produced by PerfectLight.

3.2 Principles of Primary Instrumentation

UV-Vis

Electrons in molecules can absorb the UV light energy and excite to higher anti-bonding molecular orbitals. The UV-Vis spectrum gives information about the light absorbance of the sample at different light wavelengths. The absorbance is related to the concentration of the solution, which is described by Beer's law:

$$A=-\log T=\alpha lc$$

Where A is the absorbance, T is the transmittance, α is the molar absorptivity (L/mol/cm), l is the path length of radiation (cm), and c is the concentration.[113] From a series of known concentrations of one substance, a linear calibration curve can be plotted within a proper range. Thus the UV-Vis spectrometer can be used for quantitative determinations. In our research, UV-Vis was used for measuring the absorbance and band gap of solid samples. Absorbances of liquid samples were converted to weight concentration and monitored the process of photodegradation.

FTIR

FTIR spectroscopy is widely used for analysing the chemical bonding and molecular structure of organic compounds and some inorganic materials.[114] It works based on the absorption of infrared radiations, leading to the transitions from the ground state to an excited state. The absorption occurs when the frequency of light matches the characteristic frequencies of chemical bond vibrations.[114] For regular IR, the incident IR light, which is different single wavelengths, is reflected and absorbed by the sample, and the transmission light is detected. FTIR can collect the spectral data of all wavelengths in one pass.

An FTIR spectrometer includes a detector, a source of infrared radiation, a beam splitter, a sample chamber, and mirrors. The FTIR collects the interferogram as raw data, then Fourier is transformed to produce the IR spectrum. ATR-FTIR uses a crystal through which IR light passes and interacts with the samples. In our research, FTIR was used to identify the structure of samples by characterisation peaks and analyse the changes of organic functional groups upon modifications.

XRD

XRD is a non-destructive technique to obtain the crystallographic information of material. Basically, diffraction occurs when the photons from the X-ray are scattered by the atoms in the lattice. Bragg's law[115] (shown in Figure 11) gives an equation:

$$n\lambda = 2d\sin\theta$$

Where n is the order of reflection, λ is the wavelength of incident X-ray, d is the spacing between the crystal planes, and θ is the glancing angle. For inducing an enhanced interference, the difference in path length of incident lights is nλ, and its relation to d and θ can be expressed by trigonometric function and finally gives Bragg's law. The x-ray diffractometer records data and provides peaks, and the d-spacing can be calculated by Bragg's law.

XRD can provide clear and high signal-to-noise ratio peaks of samples. XRD can be used for semiquantitative analysis and identification of unknown crystals by comparing the characterization peaks with the database. XRD is widely used in drug development, geology, engineering, and materials science. The main limitation of XRD is that the sample must be tiny, and its accuracy towards small crystalline structures is poor. In our research, XRD is mainly used to identify the phases of samples and investigate the phase transformation process of TiNT under annealing.

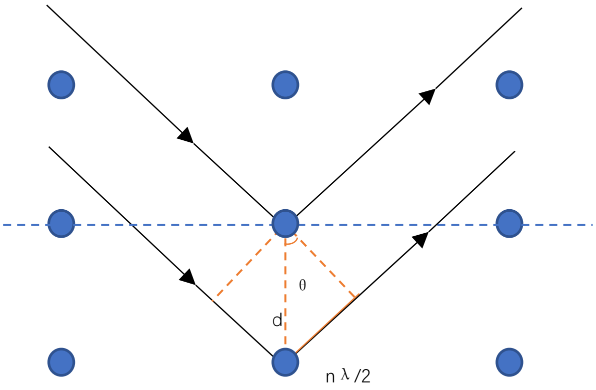

Figure 11 Illumination of Bragg's law: $n\lambda = 2d\sin\theta$, where n is the order of reflection, λ is the wavelength of incident X-ray, d is the spacing between the crystal planes, and θ is the glancing angle.

TEM

A TEM instrument comprises several components shown in Figure 12, including electron gun, condenser, specimen, objective lens, objective aperture, projector lens, and viewing screen. Electrons are fired from the electron gun down through the specimen, and when the electron beam interacts with the sample, an image is created and recorded by a charge-coupled device (CCD) camera. Due to wave-particle duality, electrons with high energy can behave like waves. Electrons can pass through the specimen and out the other side, then the beam is focused to form an image on the screen.

TEM has many advantages. TEM can provide powerful magnification, which can be one million times or more, and the images are high-quality. TEM can provide morphology, element information, and crystallographic information of samples. Therefore, TEM has many applications in a variety of fields. Despite the advantages, TEM has some limitations. TEM is a large machine and quite expensive. The operation and maintenance of it require special training. The samples for TEM are limited to the small specimen that is transparent to electrons and can be put inside the vacuum chamber, and the specimen may be destroyed by the intense electron beams. In our research, we used TEM and HRTEM to analyse the morphology and crystallographic information of nano-sized materials.

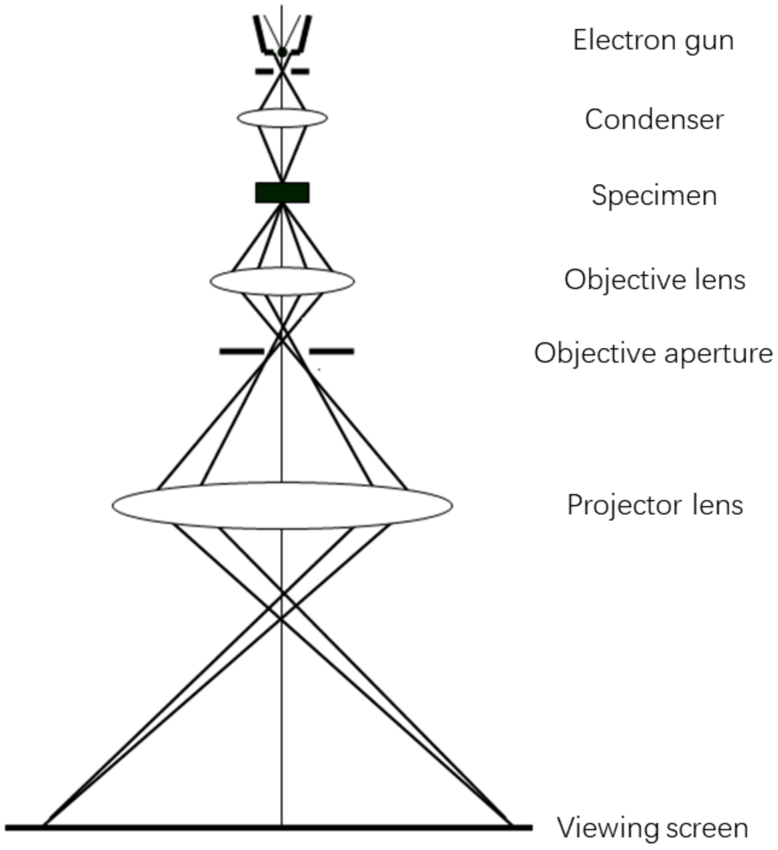

Figure 12 Component of a TEM instrument. From top to bottom: the electron gun, condenser, specimen, objective lens, objective aperture, projector lens, and viewing screen,

Raman

Raman spectroscopy is a technique to observe vibrational, rotational, and other low-frequency modes in a system. In chemistry, it is used to provide a fingerprint to identify molecules.[116] For example, silicon shows a characterisation peak at 520nm.[117] Figure 13 explains the basic principle of Raman spectroscopy. Under external light illumination, vibrations, phonons, or other excitations interact with light and are motivated to virtual energy states with higher energy. Most of them will return to their original energy level and release light with the same frequency as the incident light. This kind of scattering is called Rayleigh scattering. However, a small portion of them return to higher/lower energy levels and release light with a different frequency from the incident light. This kind of scattering is called Raman scattering. A Raman spectroscopy machine provides laser light, filters off Rayleigh scattering signals, and collects Raman scattering signals to provide a spectrum. Usually, laser light sources have specific wavelengths, including 532nm, 633nm, and 785nm.

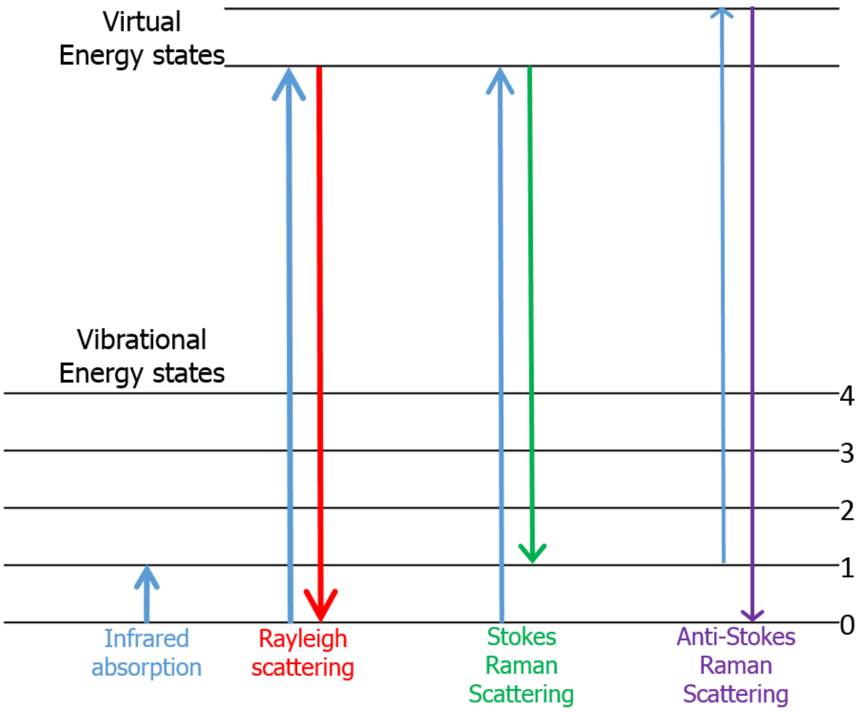

Figure 13 Principle of Raman. Stokes and anti-Strokes Raman scattering are caused by the excitations going back to higher/lower energy levels and releasing light with a different frequency from the incident light.

With the development of laser technology, Raman spectroscopy has been widely used for identifying molecules and collecting structure information of samples. However, the low intensity of Raman signals has become a limitation. Surface enhanced Raman scattering (SERS) is a technique that enhances Raman scattering signals of molecules by adsorbing on support materials. Typically, the support materials are based on noble metals, such as gold tips and gold nanoparticles. In the literature, the exact mechanism of SERS is still a matter of debate. There are two main theories to explain the SERS.

Electromagnetic (EM) theory explains that SERS is caused by an enhancement in the electric field provided by the surface plasmon like AuNPs.[99] Chemical theory explains the SERS by charge transfer complex formed between the substrate and the detected molecules.

The enhancement factor (EF) of SERS is calculated by equation (10)[118-121], where I_{SERS} and I_0 are the intensities of the selected Raman peak in relevant spectrums. N_{SERS} and N_0 are the average number of molecules in scattering for SERS and normal measurement. Equation (11)[122] shows the calculation of N_{SERS} and N_0 under an assumption that the probed molecules disperse uniformly on the substrates. N is the number of molecules, C is the molar concentration of the probed solution, V is the volume of droplet, N_A is the Avogadro constant which is $6.22*10^{23}$ particles per mole, and S_{scan} and S_{sub} are the areas of laser spot and substrate, respectively. The radius of the laser spot is calculated by Equation (12), where λ is the wavelength of laser light and NA is the microscope numerical aperture of the lens.

$$EF = \frac{I_{sers}/N_{sers}}{I_0/N_0} \tag{10}$$

$$N = CVN_A S_{scan}/S_{sub} \tag{11}$$

$$R_{spot} = 1.22 \times \lambda/NA \tag{12}$$

In our research, the Raman technique was used to provide structural information of TiNT and modified TiNT samples and investigate the surface enhanced Raman scattering caused by the TiNT-catechol systems.

3.3 Sample preparation and Analysis Methods

UV-Vis

For solid samples, the powder was firstly dispersed in water in small sample vials by ultrasonication. Then several drops of dispersion were dropped on glass slides and dried at 50°C for 30 mins. For liquid samples, the liquid was put in a quartz cuvette and measured.

The UV-Vis data was imported into OriginPro and plotted. Band gaps of samples were calculated by two methods. One method was plotting a tangent line of absorption edge and reading the point of intersection of the tangent line of the linear part of the plot and the X-axis. The resulted value of wavelength (in nm) was converted to band gap energy (in eV) by the equation: $Eg=h*c/\lambda$, where Eg is the band gap, h is the Planks constant ($6.626*10^{-34}$ J/s), c is the speed of light ($3*10^{8}$ m/s), and λ is the wavelength. This equation can be simplified to $Eg=1240/\lambda$. Another method is the Tauc plot. The Y-axis is $(\alpha h\nu)^{(1/n)}$, where $n=0.5$ for direct semiconductors and α is the absorption coefficient derived from UV-Vis absorbance via Beer's law. The X-axis is hν derived from the wavelength. The point of intersection of the tangent line of the linear part of the plot and the X-axis indicates the band gap. For degradation results, a correction curve was firstly fitted and plotted by measuring the absorbance of known concentrations of methylene blue. The absorbances of degradation samples were converted to weight concentrations, then being plotted and compared.

NMR

Insoluble powder samples were directly measured for solid-state NMR. Soluble organic samples were dissolved in the deuterated solvents and transferred to NMR tubes.

NMR results were analysed using TopSpin. The general analysis process was as follows. The peaks of Deuterium reagent and tetramethylsilane (TMS) addition were used as a reference for calibration. The solvent peaks were identified based on a table of NMR chemical shifts of common solvent[123]. Other peaks were assigned as organic functional groups based on their chemical shifts and compared with reference compounds to monitor organic reactions and identify the product and by-product.

FTIR

Powder samples were directly measured for ATR-FTIR. For normal FTIR, the solid sample was mixed with KBr and ground into a fine powder, and then the powder was pressed to tablets and measured.

FTIR data were imported and plotted by OriginPro. Characterisation peaks of organic functional groups were compared and identified by literature/database. The samples were compared to each other to show the appearance or disappearance of peaks, which indicated the changes of functional groups and the type of reactions.

XRD

Powder samples were ground and put on sample holders, then pressed to form flat surfaces.

XRD data were plotted by OriginPro. The peaks were compared with the literature and JCPDS (The Joint Committee on Powder Diffraction Standards) database for identifying the phase of samples. The samples were compared to each other for indicating the phase changes during the surface modification and annealing process.

TEM

Samples were dispersed in ethanol and ultrasonicated for 15 mins. Then a tiny amount of dispersion was dropped on an ultrathin carbon film supported copper grid and dried under a heating lamp.

TEM images were processed by GMS3, and the d-spacing of the selected area was measured by the software. The measured d-spacing was further compared with literature and XRD results.

Raman

For solid samples, the powder was put on the centre of glass slides and focused via both microscope and laser spot. For liquid samples, a flat metal plate was firstly measured as a background. Several drops of liquid samples were dropped on the centre of the metal plate, focused by laser, and were measured immediately to minimise the effects of evaporating.

Raman data were plotted by OriginPro. Characterisation peaks were compared and assigned according to literature results. Samples were compared to each other for investigating the enhancement of signals.

Zeta potential

Samples were prepared by dispersing solid samples in water followed by ultrasonication for 30 minutes. The dispersion was transferred to a sample cell then measured.

Zeta potential directly gives values without process. The figures were plotted by OriginPro.

XPS

Powder samples were placed/pressed on tape then measured.

XPS data were plotted by OriginPro. The peaks were split and fitted based on the binding energy of the orbitals of each element. The areas of peaks were calculated by the software. Samples were compared to each other and literature results to indicate the changes of samples upon modification.

GC-MS

Samples were dissolved in organic solvent then transferred to sample vials.

Peaks from the resulting GC chromatogram were analysed one by one. Each GC peak contained a mass spectrum. The peaks from each mass spectrum were compared with the molecular weight of organic compounds.

Mass Spectrum (Q-TOF)

Samples were dissolved in organic solvent then measured.

For each spectrum given by Q-TOF, the peaks were compared with the proposed molecular weight of each organic product. Organic compounds were identified when the exact value of molecular weights was found from Q-TOF.

Chapter 4: Surface Enhanced Raman Scattering

4.1 Preface

In this chapter, based on our previous research of TiNT-dopamine system[33], the structures of the modifiers of TiNT were extended to other catechol compounds, including 3,4-dihydroxybenzoic acid, 4-nitrocatechol, and 3-hydroxytyrosol. By investigating the characterization of the TiNT-catechol system, selective surface enhanced Raman scattering of systems were reported, and the reasons were further discussed. The outcome of this chapter was published as follows: Liu, R.; Morris, E.; Cheng, X.; Amigues, E.; Lau, K.; Kim, B.; Liu, Y.; Ke, Z.; Ashbrook, S. E.; Bühl, M.; Dawson, G., SERS of Trititanate Nanotubes: Selective Enhancement of Catechol Compounds. *Chem. Select,* **2018,** *3* (28), 8338-8343.

4.2 Experimental Section

Materials

Titanium dioxide (anatase) and dopamine hydrochloride were purchased from Sigma-Aldrich. 4-Nitrocatechol, 3,4-dihydroxybenzoic acid and 3-hydroxytyrosol were purchased from Aladdin. Concentrated HCl solution and ethanol were purchased from Sinopharm. NaOH was purchased from Greagent. Teflon vessels and autoclaves were purchased from Tansoole. Clear glass sheets were purchased from Fisher Scientific. Ultrapure water was produced by an Advantage A10 water purification system from EMD Millipore. Ultrathin carbon film supported copper grids were purchased from Beijing XXBR Technology Co., Ltd.

Synthesis

Synthesis of TiNT was carried out based on a literature procedure[61]. Experimentally, anatase TiO_2 (1 g) was added to 10 M NaOH solution (20 mL), and the resultant slurry was stirred at room temperature for at least 30 min to disperse TiO_2 powder well. Then the mixture was transferred into a Teflon vessel, and the vessel was sealed in a metal autoclave. Next, the autoclave was placed in an oven at 140 ^{o}C. After 72 hours, the autoclave was taken out of the oven and cooled under running water. The white solid in the Teflon vessel was removed and washed with distilled water, 0.1 M HCl solution, and finally with a large amount of distilled water until the pH value of the filtrate was 7. The solid was then collected, dried at 60 ^{o}C, and finally ground into fine powder.

Surface modification of TiNT: Typically, TiNT was suspended in ultrapure water, then 10 wt.% of organic compound was added. For TiNT-3,4-dihydroxybenzoic acid, TiNT-4-Nitrocatechol and TiNT-3-hydroxytyrosol, the mixture was stirred under room temperature overnight. The resulting solid was filtered, washed with water (50 mL) and ethanol (20 mL) to remove any excess ligand. The solid was then collected, dried at 60 °C and finally ground into fine powder.

4.3 Results and Discussions

In our previous research, two models for self-assembled dopamine on the surface of TiNT were proposed: monodentate model interacted through hydrogen bonds shown in

Figure 14(a) and bidentate model linked by π-π stacking shown in

Figure 14(b).[33] Dopamine monomer units have shown a close-packed arrangement on the TiNT surface via the two ortho hydroxyl groups on the aromatic ring: the catechol structure.[33] In this chapter, a series of catechol compounds functionalized TiNT systems were synthesized, and it is found that the functional groups on the sidechain of catechol compounds were of decisive significance to the surface enhanced Raman scattering (SERS) effect. Figure 15 shows the chemical structure of dopamine, 3-hydroxytyrosol, 3,4-dihydroxybenzoic acid and 4-nitrocatechol. All these compounds contain the catechol sub-structure and different functional groups attached to the benzene ring. Dopamine and 3-hydroxytyrosol have carbon chains with ending groups on the aromatic rings, while the other two have functional groups directly attached to the ring.

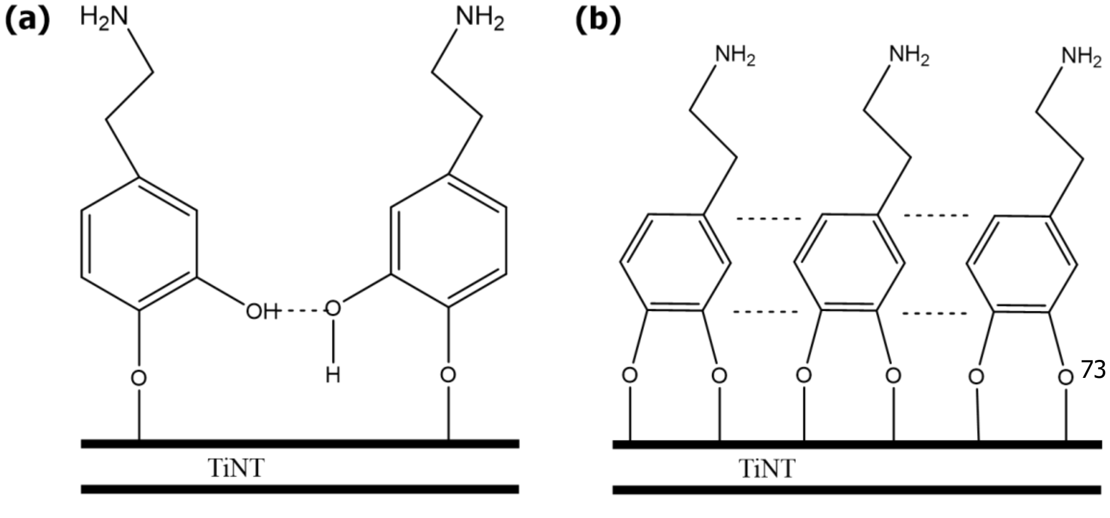

Figure 14 (a) monodentate model of TiNT-dopamine system: one hydroxyl group attach to TiNT and the other hydroxyl group interact with other dopamine molecules through hydrogen bonds; (b) bidentate model of TiNT-dopamine system: two hydroxyl groups attached to TiNT and dopamine molecules interact through п-п stacking [33] (Figure reprinted with the permission of John Wiley and Sons, ref 33)

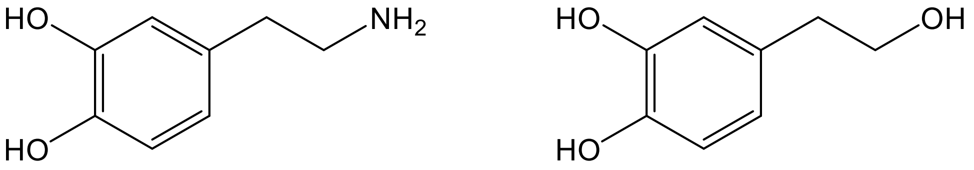

dopamine 3-hydroxytyrosol

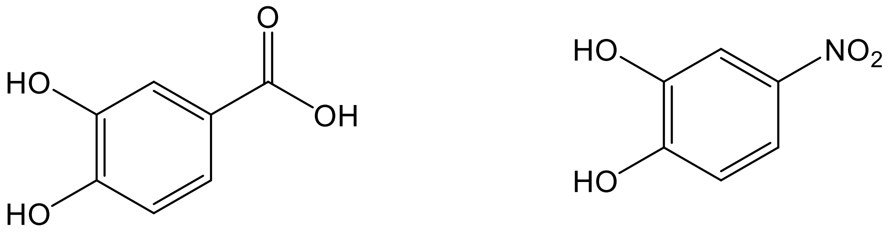

3,4-dihydroxybenzoic acid 4-nitrocatechol

Figure 15 Structures of dopamine, 3-hydroxytyrosol, 3.4-dihydroxybenzoic acid and 4-nitrocatechol. They all contain a catechol structure, but the ending groups are different.

Optical Property

Figure 16 shows the colour of the samples. Before modification, the TiNT and modifier were white except 4-nitrocatechol, which was light yellow. During the modification, rapid colour changes of the reaction mixture were observed, with the colours of products ranging from light brown to dark brown. Figure 17 shows the solid UV-Vis of catechol functionalized TiNT systems. Before modification, the TiNT showed almost no absorbance within the range 400-800 nm, which is a visible light range due to its large band gap. After modification, all three TiNT-catechol systems showed a similar profile: a charge transfer band[124] dominating the visible range of the spectrum up to 600 nm and a shoulder leading into the band edge at around 380 nm. Among the TiNT-catechol samples, TiNT-4-nitrocatechol showed the highest intensity of the shoulder. However, the UV-Vis absorbance of these samples was close. This indicated a similar attachment mode for all samples, which was expected for the selection of catechol modification compounds. Similar charge transfer bands and the formation of charge transfer between TiO_2 and absorbed organic compounds were reported by researchers.[124-127] Therefore, the colour changes and UV-Vis absorbance were explained by the formation of the charge transfer complex of the TiNT-catechol system.

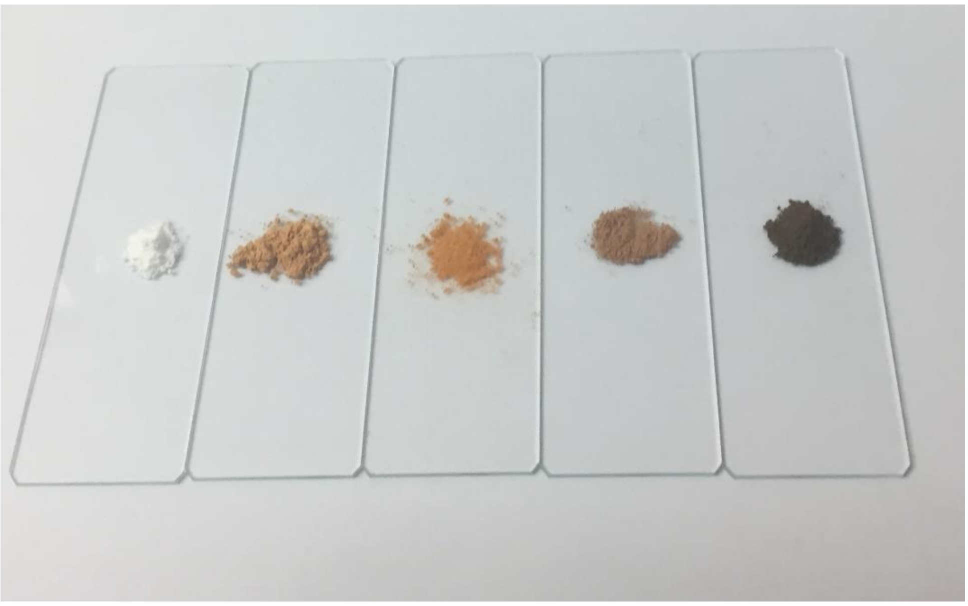

Figure 16 Photos of TiNT-catechol samples from left to the right: TiNT, TiNT-3,4-dihydroxybenzoic acid, TiNT-4-nitrocatechol, TiNT-3-hydroxytyrosol, and TiNT-dopamine. TiNT is white when the TiNT-catechol compounds show colours from light brown to dark brown.

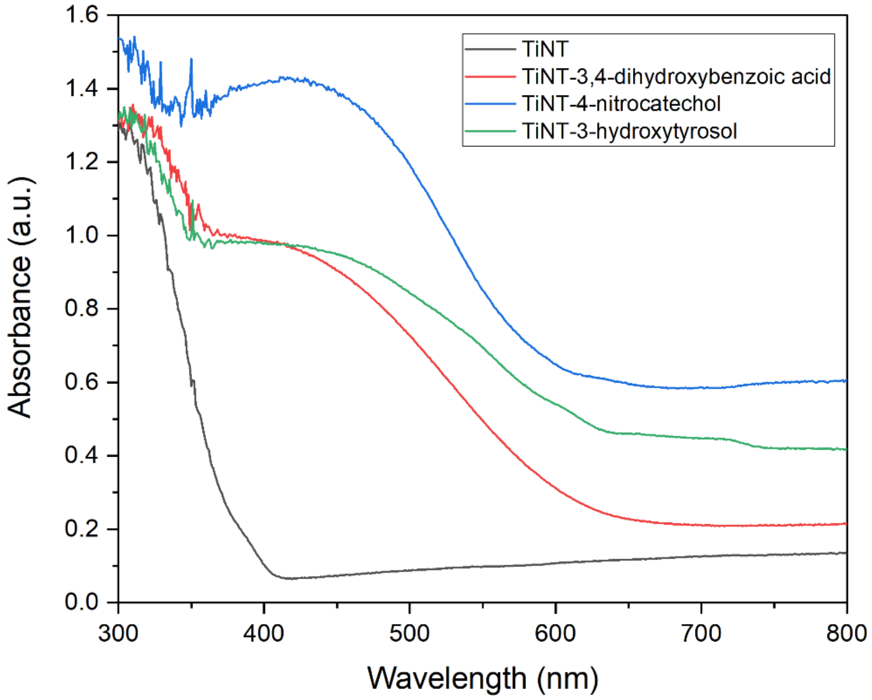

Figure 17 UV-Vis absorbance of catechol functionalized TiNT systems. TiNT-catechol samples show charge transfer band[124] dominating the visible range of the spectrum up to 600 nm and a shoulder at around 380 nm.

Solid-State NMR

To investigate the binding mode between catechol compounds and TiNT, ^{13}C NMR of organic molecules and TiNT-catechol samples were measured and compared. Because the modified TiNT samples could not dissolve in any common deuterated solvents, solid-state NMR was used instead of liquid-state NMR. The ssNMR spectra of modified TiNT samples and their starting materials are shown in Figure 18 (a)-(f), and the spectra indicated the attachment of organic molecules on TiNT, as previously observed for TiNT-dopamine.[33] This was identified through peaks shifting to higher ppm values, which were caused by the replacement of C-OH bonds by C-O-Ti bonds. In TiNT-dopamine[33] and these three TiNT-catechol systems, the peak of C-OH could still be found, which indicated the presence of monodentate attachment. Downshifting of an aromatic carbon signal was observed and explained by π-π stacking of the monomers on the nanotube surfaces.

For the starting material 3,4-dihydroxybenzoic acid shown in Figure 18 (a), the ^{13}C solid-state NMR peaks were assigned as follows: the carbon atom in the carboxylic acid group at δ = 174.7 ppm, the two aromatic carbon atoms attached to the hydroxyl groups at δ = 151.5 and 143.1 ppm, and the other four aromatic carbon atoms at δ = 126 (two peaks overlapped), 119.6 and 116.5 ppm. After functionalization, the signals of the carboxylic acid group shifted to a lower ppm value, which was 171.6 ppm. The two hydroxyl carbon signals shifted to larger ppm values, which were 163.6 and 156 ppm, and the shift indicated the replacement of the C-OH bonds to C-O-Ti bonds. The signals of the other four aromatic carbon atoms shifted to δ = 124.8, 121, 112 and 105 ppm, which were lower compared to the starting material.

For the starting material 4-nitrocatechol, shown in Figure 18 (c), the ^{13}C solid-state NMR were assigned as follows: the two aromatic carbon atoms attached to the hydroxyl groups at δ = 151.1 and 143.2 ppm, the nitro functionalized aromatic carbon at δ = 140.4 ppm, and the other three aromatic carbon atoms at δ = 119.6, 117.2, and 111.6 ppm. After functionalization, the two hydroxyl carbon signals shifted to larger ppm values, which were 167.2 and 156.8 ppm, and indicated the replacement of the C-OH bonds to C-O-Ti bonds. The other three aromatic carbon atoms' signals shifted to δ = 120.1, 111.8, and 107.6 ppm.

For the starting material 3-hydroxytyrosol, shown in Figure 18 (e), the peaks were assigned as follows: the two aromatic carbon atoms attached to the hydroxyl groups at δ = 144.9 and 143.5 ppm, the chain functionalized carbon at δ = 133 ppm, the other three aromatic carbon atoms at δ = 122.7, 119.2 and 116.8 ppm, and the carbon atoms in the carbon chain at δ = 64.2, and 37.8 ppm. After functionalization, the two hydroxyl carbon signals shifted to larger ppm values, which were 156.8 and 154.8 ppm, and indicated the replacement of the C-OH bonds to C-O-Ti bonds. The other three aromatic carbon atoms' signals shifted to δ = 132.6, 120.8 and 114.8 ppm. The peaks which stood for the carbon chain were still present.

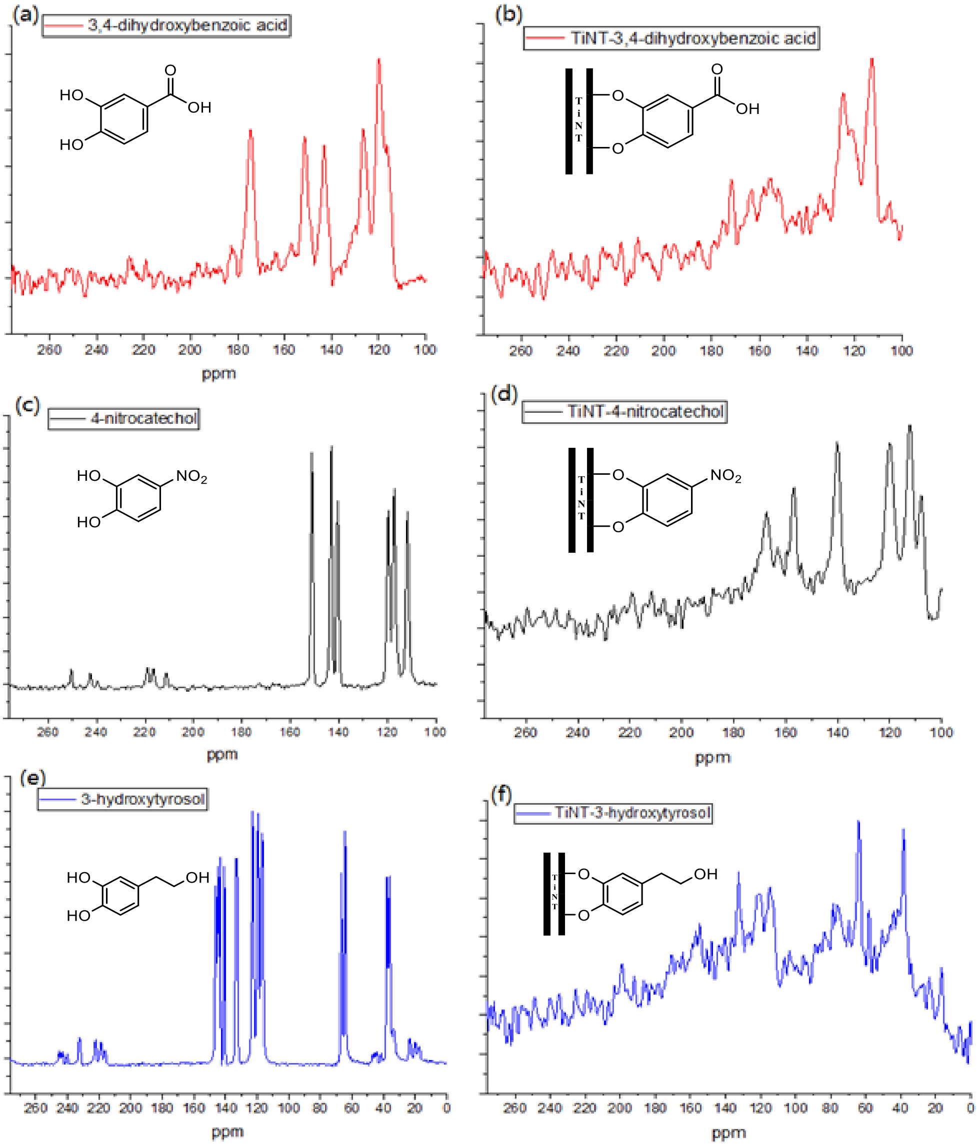

Figure 18 ssNMR spectrum of (a) 3,4-dihydroxybenzoic acid, (b) TiNT-3,4-dihydroxybenzoic acid, (c) 4-nitrocatechol, (d) TiNT-4-nitrocatechol, (e) 3-hydroxytyrosol and (f) TiNT-3-hydroxytyrosol. The spectra indicated the attachment of organic molecules on TiNT by the shifting of peaks.

Fourier Transfer Infrared Spectroscopy

To support ssNMR results, Fourier Transfer Infrared Spectroscopy was used to indicate the changes in functional groups upon surface modification. Figure 19 shows FTIR absorbance of (a) dopamine & TiNT-dopamine[33], (b) 4-nitrocatechol & TiNT-4-nitrocatechol, (c) 3,4-dihydroxybenzoic acid & TiNT-3,4-dihydroxybenzoic acid, and (d) 3-hydroxytyrosol & TiNT-3-hydroxytyrosol. It can be observed from Figure 19 (a) that after surface modification, the peak at about 1320 cm^{-1} disappeared, which was assigned as an OH bend.[33] This phenomenon was explained by the replacement of the C-O-H bond by the C-O-Ti bond.

FTIR absorbance of the other three organic modified TiNT samples and their starting materials were measured and compared. For TiNT-4-nitrocatechol system, which is shown in Figure 19 (b), the OH bend peaks exist in both unmodified and modified samples. The OH bend peak remaining in TiNT-4-nitrocatechol was explained as mono attachment of hydroxyl group on TiNT surface: one hydroxyl group attached to titanium, and the other hydroxyl group was still there. However, on the other side, the OH bend peak could not be found in the other samples. Because of the low loading amounts of organic molecules on the TiNT surface (below 10 wt.%), FTIR signals of modified TiNT samples were poor and not of a similar magnitude to the organic samples. As a result, the comparations of FTIR spectra were aimed to support the binding model proposed by ssNMR.

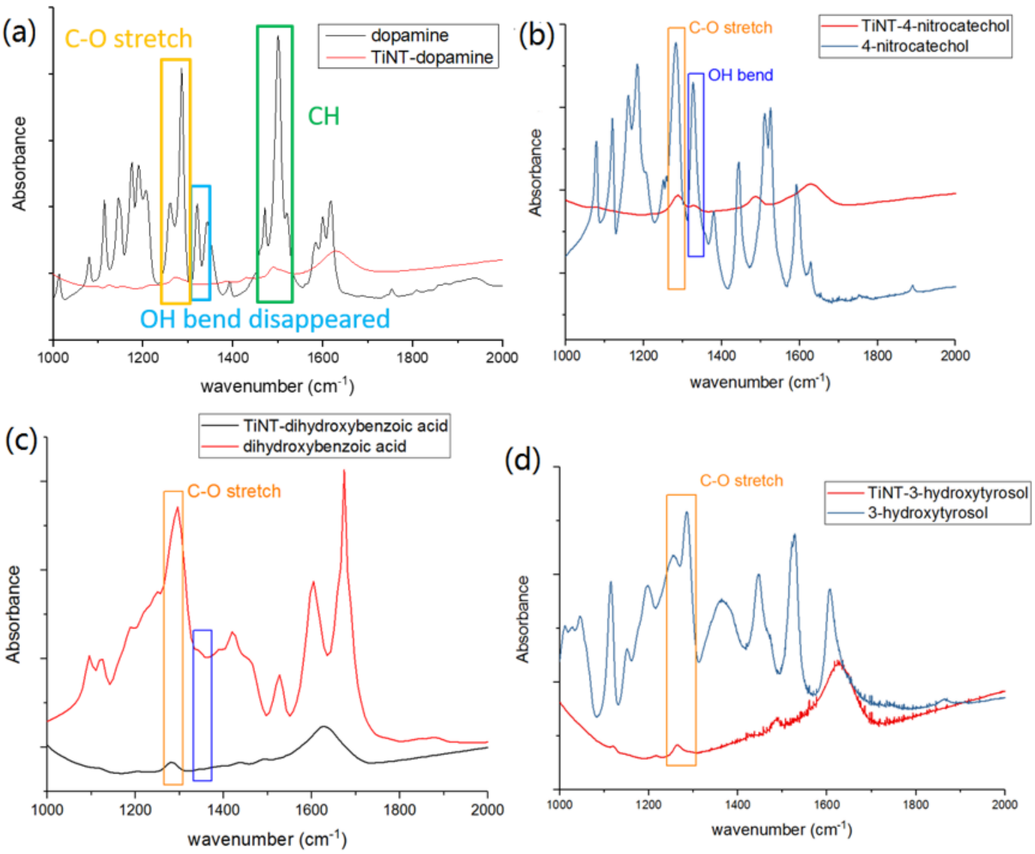

Figure 19 FTIR of (a) dopamine and TiNT-dopamine[33], (b) 4-nitrocatechol & TiNT-4-nitrocatechol, (c) 3,4-dihydroxybenzoic acid & TiNT-3,4-dihydroxybenzoic acid, and (d) 3-hydroxytyrosol & TiNT-3-hydroxytyrosol. The weakening of OH peaks indicated the replacement of the C-O-H bond by the C-O-Ti bond. (Figure reprinted with the permission of John Wiley and Sons, ref 33)

X-Ray Diffraction

XRD patterns of TiNT and catechol modified TiNT are shown in Figure 20. The spectrum of modified TiNT was assigned as follows[61]: the broad peak at 2θ = 25° and 28° corresponded to the nanotube interlayer spacing (110) and (310), and the peak at 2θ = 48° corresponded to the hydrogen titanate compounds

(020). Bragg's law[128] describes the relationship between scattering angle (θ) and interplanar distance (d): $n\lambda = 2d\sin\theta$. n is the order of diffraction which was 1, and λ is the wavelength of X-ray which was 0.15406 nm. After modification, a broad peak centred at 28° can be observed instead of sharp peaks. It can be calculated that the d spacing is 3.18 Å. This number is within the expected range for π-π stacking[129]. The peak at $2\theta = 48^{\circ}$ did not change upon modification, which indicated that the TiNT structure did not change. The new peak at $2\theta = 13^{\circ}$ was assigned as the interaction between the layers of nanotubes. No significant difference between the three modified samples was found, which means the crystal structure of modified samples were not determined by the ending functional groups of the modifier.

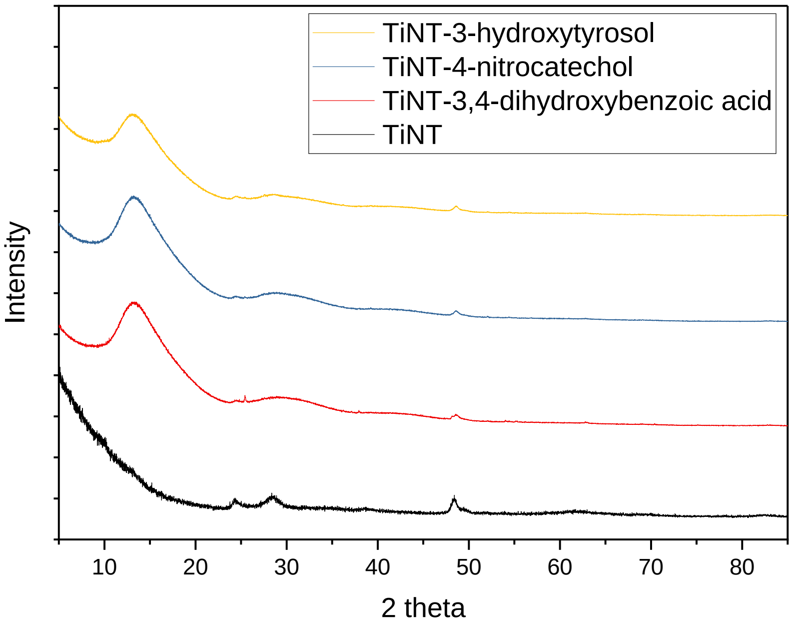

Figure 20 XRD patterns of TiNT and TiNT-catechol. TiNT: peaks at 25° and 28° are the nanotube interlayer spacing (110) and (310); peak at 48° is the hydrogen titanate compounds (020). TiNT-catechol: broad peak at 28° is caused by π-π stacking; new peak at 13° is the interaction between the layers of nanotubes

Transmission Electron Microscopy

Figure 21 shows transmission electron microscopy (TEM) images of (a) TiNT, (b) TiNT-dopamine[33] and (c) & (d) TiNT-4-nitrocatechol. TEM shows the morphology of unmodified and modified TiNT. It was observed that the single nanotubes had a diameter around 10 nm and various lengths around 100 nm. The morphology of nanotubes did not change upon surface modification. Walls of the scrolled nanotubes could be found as the dark area around nanotubes. Bright edges were found for the modified samples, which may be thin amorphous coatings of 1-2 nm. However, the lattice spacings of samples were indistinct. This was due to the poor crystallinity of TiNT, which was also shown from XRD patterns with low intensity.

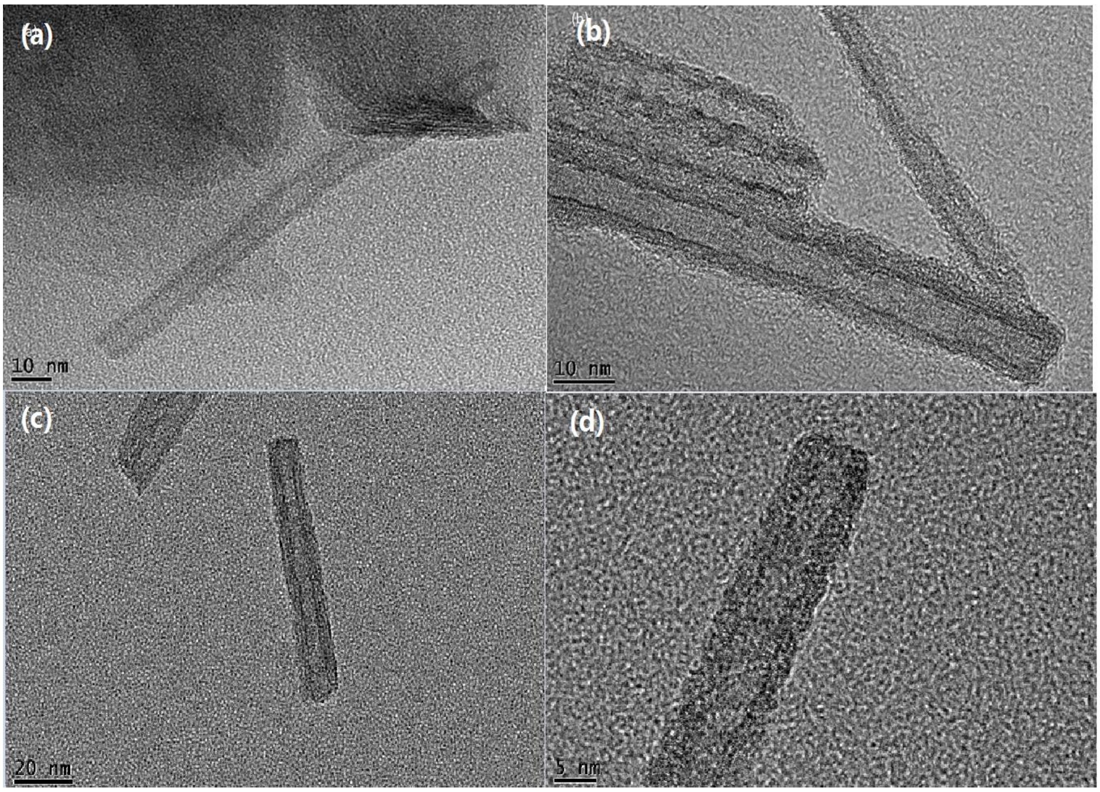

Figure 21 TEM images of (a) TiNT, (b) TiNT-dopamine[33] and (c) & (d) TiNT-4-nitrocatechol. The nanotube has a diameter around 10 nm and a length around 100 nm. The morphology of nanotubes did not change upon surface modification. (Figure 21 (b) was reprinted with the permission of John Wiley and Sons, ref 33)

Loading Amount

For identifying the loading amounts of organic compounds on the TiNT surface, thermogravimetric analysis (TGA) and CHN elemental analysis were used, and the results were compared. TGA is a technique for measuring the mass of a sample over time when the temperature changes[130]. During the heating process, surface water and organic compounds were lost and purged out from the crucibles. As a result, the weight changes given by TGA can indicate the weight of surface water and the loading amount of the organic modifier. Figure 22 shows the TGA temperature-weight% loss curve of TiNT (a) and TiNT-3,4-dihydroxybenzoic acid (b). Figure 22 (a) shows two segments: TiNT lost surface water up to around 150 °C and continuously lost water on the internal nanotube surfaces until around 350 °C. The total wt. % loss was 13.3%. This result was comparable to the results from our previous result of TiNT, which was 11 wt. % loss of water up to 300 °C[33]. From Figure 22 (b), it can be seen that TiNT-3,4-dihydroxybenzoic acid had an additional loss of 4.7 wt. %, which was attributed to the loss of 3,4-dihydroxybenzoic acid on the nanotube surfaces.

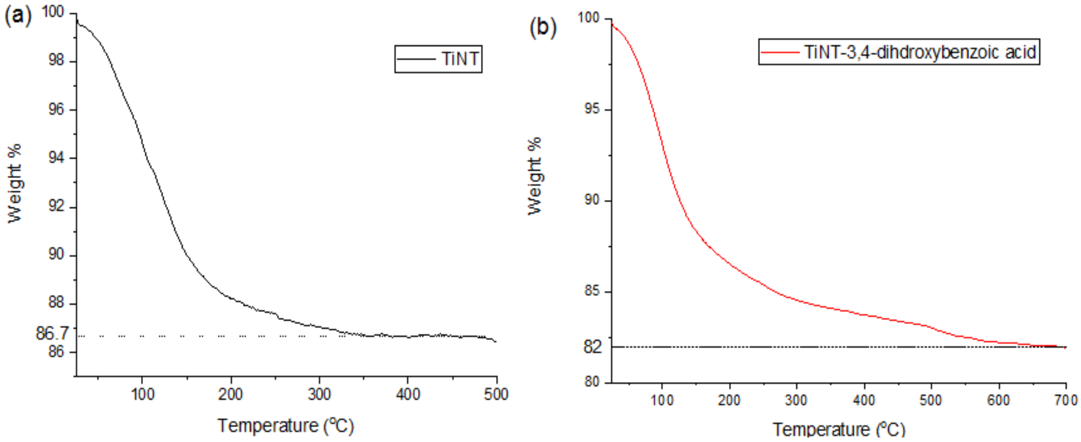

Figure 22 TGA Temperature-Weight % curves of (a)TiNT and (b)TiNT-3,4-dihydroxybenzoic acid. TiNT lost 13.3 wt. % of water up to 350 °C, when TiNT-3,4-dihydroxybenzoic acid had an additional loss of 4.7 wt. % as loss of 3,4-dihydroxybenzoic acid on the nanotube surfaces.

CHN elemental analysis measures the wt. % of elements by combustion of samples. Carbon, hydrogen, and nitrogen elements from the organic compound were oxidized in the air under 900 °C, and the element amounts were measured by detecting their oxide. By this method, wt. % of organic loaded on nanotubes were calculated and compared with the results from TGA. Table 2 shows the CHN element analysis results of modified TiNT samples, which were calculated based on the weight percent of carbon. The overall weight percent of organic were various from 2.07 to 4.3 wt. %. For 3,4-dihydroxybenzoic acid, CHN elemental analysis showed the weight percent of organic was 3.05 wt. %, which was lower than the result from TGA (4.7 wt. %). It was proposed to be caused by the status and accuracy of the two techniques, but the results fell within the expected range.

Table 2 CHN Elemental Analysis of modified TiNT samples

TiNT-+	N %	C%	H%	Organic Molecule Formula	MW	Calculated wt.%
3,4-dihydroxybenzoic acid	0.02	1.66	1.908	$C_7H_6O_4$	154.12	3.05
4-nitrocatechol	0.27	1.80	1.906	C_6H_5NO	155.11	3.88
3-hyroxytyrosol	0.02	1.29	1.879	$C_8H_{10}O_3$	154.17	2.07
dopamine[a]				$C_8H_{11}NO_2$	153.18	4.3

[a] Data from reference[33]

Surface Enhanced Raman Scattering

Surface Enhanced Raman Scattering (SERS) of enediol ligands including dopamine, salicylate, acetylacetone, and benzoate attached to TiO_2 nanoparticles was reported, which is caused by the formation of a charge transfer complex.[124, 131] In this project, a similar enhancement was observed on TiNT. However, it depended on the structure of the catechol ligands on TiNT. Raman signals of 3,4-dihydroxybenzoic acid and 3-hydroxytyrosol at concentrations of 0.1 M were recorded. Due to the poor solubility of 4-nitrocatechol, its concentration was lower than 0.1 M but was on the same order of magnitude. 0.1 M of modifiers equates to a wt.% of 1.5%, which was of a similar magnitude to the catechol modified samples compared with the above loading amounts results by CHN analysis and TGA.

Figure 23 (a) and (b) shows the enhanced Raman signals observed for TiNT-4-nitrocatechol and TiNT-3,4-dihydroxybenzoic acid. The enhancement of signals was ~10 fold for TiNT-3,4-dihydroxybenzoic acid and ~75 fold for TiNT-4-nitrocatechol. For the other two systems, which were TiNT-dopamine and TiNT-3-hydroxytyrosol, although they had shown similar UV-Vis spectra, no distinguishable Raman enhancement could be observed. The differences between 4-nitrocatechol, 3,4-dihydroxybenzoic acid, 3-hydroxytyrosol and dopamine (structures are shown in Figure 15) are the proximity and properties of side chains to the benzene ring. The nitro group is a strong withdrawing group, and the carboxylic acid group is a moderate electron withdrawing group, while the alkyl side chains with amide and hydroxyl groups are electron donating groups. In this project, only the catechol compounds which contained a directly attached functional group on the benzene ring showed SERS.

The assignment of Raman spectra was based on the literature.[132-134] For TiNT-4-nitrocatechol, the bands from 1100 cm^{-1} to 1600 cm^{-1} were assigned as follows: NO_2 bend (~823 cm^{-1}), phenolate C-O stretch (~1274 cm^{-1}), stretching between the two hydroxyl carbons on the benzene ring (~1475 cm^{-1}), and skeletal modes of the benzene ring (~1322 cm^{-1}, 1419 cm^{-1}, and 1564 cm^{-1}). Similarly, the bands of TiNT-3,4-dihydroxybenzoic acid were assigned as the phenolate C-O stretch (~1279 cm^{-1}), stretching between the two hydroxyl carbons (~1482 cm^{-1}), and skeletal modes of the benzene ring (~1330 cm^{-1}, 1430 cm^{-1}, and 1584 cm^{-1}). Bands in the range of 1100-1600 cm^{-1} showed enhancement and were the modes associated with ligand to metal charge transfer[124, 132, 133]. Figure 23 (c) shows the comparison of TiNT and TiNT-4-nitrocatechol. The bands of TiNT-4-nitrocatechol below 750 cm^{-1} were highly relevant to TiNT. Besides these bands, the peak at around 820 cm^{-1} was interesting. In 4-nitrocatechol and TiNT-4-nitrocatechol systems, this peak was assigned as a NO_2 bend. This peak was observed in TiNT-3,4-dihydroxybenzoic acid. However, there is no peak around this wavenumber observed in 3,4-dihydroxybenzoic acid or the unmodified TiNT. This peak was proposed to be caused by the changes of the symmetry of the nanotube surface upon attachment, so it was proposed to be Ti-O-Ti framework stretching.

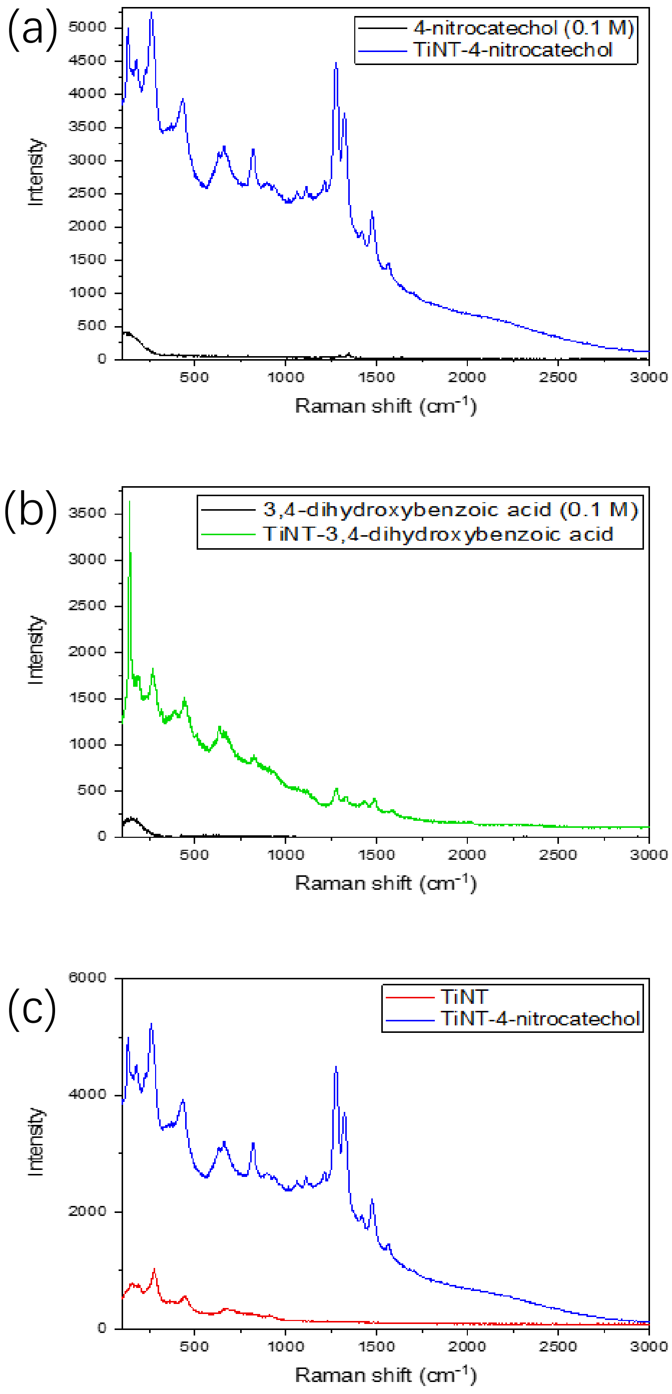

Figure 23 Raman spectra of (a) 4-nitrocatechol (0.1 M) and TiNT-4-nitrocatechol. (b) 3,4-dihydroxybenzoic acid (0.1 M) and TiNT-3,4-dihydroxybenzoic acid. (c) TiNT and TiNT-4-nitrocatechol. The enhancement of signals was ~10 fold for TiNT-3,4-dihydroxybenzoic acid and ~75 fold for TiNT-4-nitrocatechol.

The reason for enhancement was explained by the formation of the charge transfer complex, which is the chemical mechanism of SERS. The reason for selective SERS on TiNT was further investigated by DFT calculation. DFT calculation was carried out by a cooperative research group at the University of St. Andrews, and the results are shown in Figure 24[135]. In this figure, the HOMO of the TiNT-catechol system was given by the catechol compounds, and the LUMO was given by semiconductor LUMO. Thus, the charge transferred from organic HOMO to semiconductor LUMO and formed a charge-transfer complex. The HOMO and LUMO positions of TiNT-catechol, TiNT-4-nitrocatechol and TiNT-dopamine were computed, and the band gaps were 1.35 eV, 1.62 eV and 1.88 eV, respectively. In the experiments, the wavelength of the laser used for Raman was 785 nm, which corresponded to 1.58 eV. SERS was observed for TiNT-4-nitrocatechol but not for TiNT-dopamine. It was proposed that the energy of the excitation laser was not enough to promote the electrons from the valence band of TiNT-dopamine to cross the band gap. Thus, no SERS was observed for TiNT-dopamine.

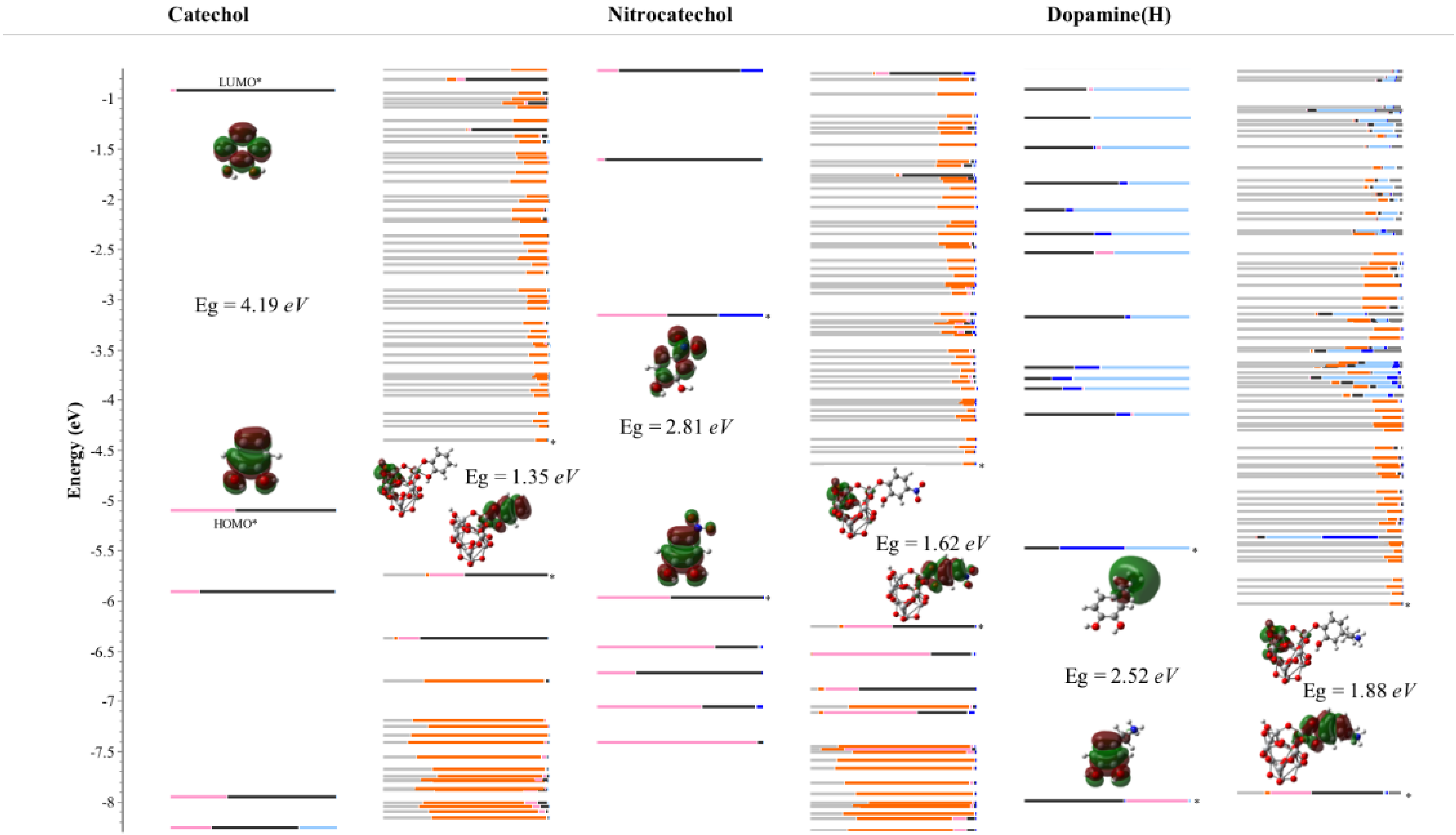

Figure 24 DFT calculation results. The HOMO and LUMO positions of TiNT-catechol, TiNT-4-nitrocatechol and TiNT-dopamine were 1.35 eV, 1.62 eV and 1.88 eV respectively

4.4 Conclusion

In this chapter, TiNT was firstly synthesized from anatase, then modified by organic modifiers including dopamine, 4-nitrocatechol, 3,4-dihydroxybenzoic acid and 3-hydroxytyrosol. The modified samples showed various colours when the TiNT was a white powder. UV-Vis absorbances of samples had shown no changes of the band gap when new absorbance shoulders were found and explained by the formation of charge transfer complex between TiNT and organic modifiers. Solid-State NMR was used for indicating the binding model, which was a monodentate attachment, of catechol compounds on TiNT. The binding model was also supported by FTIR. From XRD patterns were found poor crystalline and layer spacing peak of modified samples. The morphology of nanotubes does not change upon surface modification according to TEM and high resolution TEM images. TGA and CHN were used to identify the loading amount of catechol modifiers on TiNT, and their results were comparable and have supported each other. SERS was observed on TiNT, and it depended on the structure of the enediol ligands. Enhanced signals were reported for TiNT-4-nitrocatechol and TiNT-3,4-dihydroxybenzoic acid but not for TiNT-dopamine and TiNT-3-hydroxytyrosol. The enhancement was explained by the formation of the charge transfer complex from UV-Vis absorbance and DFT computation results. The organic compounds provided valence band when the semiconductor provided conduction band of the sub-band state. The selectivity was explained by the insufficient energy level of 785 nm laser for activating TiNT-dopamine, which has a larger HOMO-LUMO energy gap than TiNT-4-nitrocatechol based on DFT computation results.

Chapter 5: C_3N_4-TiNT Nanocomposite

5.1 Preface

Graphitic carbon nitride (g-C_3N_4) is a metal-free polymer n-type semiconductor. The band gap of g-C_3N_4 is 2.7 eV, which means it can absorb light with a wavelength smaller than 460 nm. However, it was reported that the efficiency of water splitting of g-C_3N_4 is low, which was caused by low surface area and high recombination rate of photo-generated electron-hole pairs.[81] In this chapter, g-C_3N_4 was mixed with TiNT to form a nanocomposite. Characterizations of composites were measured, and photodegradation of methylene blue by composites was tested. The phase transformation of TiNT by annealing was also investigated. TiNT-dopamine was used instead of TiNT for achieving better interaction with C_3N_4 via the amino ending group and for better dispersion and visible light absorbance.

5.2 Experimental Section

Materials

Urea and methylene blue were purchased from Tokyo Chemical Industry. Aluminium crucibles were purchased from Tansoole. Other materials used in this chapter were the same as the previous chapter.

Synthesis of g-C_3N_4

Synthesis of g-C_3N_4 was carried out based on literature method.[136] 10 g of urea was added into a 50 mL alumina crucible (with cover) then heated under 550 °C or 4 hours respectively in a muffle furnace. The heat-up rate was at 3 K/min. Then the crucible was left in the furnace until it cooled down to below 50 °C. Next, the resultant yellow loose solid was transferred to a mortar and ground to a fine powder. During this process, the product was easily lost because the powder was too light. As an improvement, the resultant solid in further reactions was transferred into clean storage bags instead to avoid losing. This synthesis was repeated several times, and the resultant amounts of product were various from 0.07 g to 0.31 g.

Synthesis of protonated g-C_3N_4 (p-C_3N_4)

0.2 g of g-C_3N_4 was dispersed in 40 mL of ultrapure water, then 40 mL of 1 M HCl solution was added dropwise. The mixture was sonicated at room temperature for 0.5 h. The mixture was transferred into centrifuge tubes, centrifuged for 10 minutes under 2000 rpm, then the liquid was removed, and the centrifuge tubes were refilled with ultrapure water. Centrifuge washing was repeated until the pH value of the liquid reached 4. The mixture was finally filtered, and the resultant yellow powder was collected and labelled as p-C_3N_4,

Synthesis of C_3N_4-TiNT nanocomposite

Following is a general synthesis method of C_3N_4-TiNT nanocomposite. The detailed using amount of chemicals varied depending on the sample. 0.05 g of g-C_3N_4 (or p-C_3N_4) was added into 200 mL of ultrapure water in a beaker, and the mixture was ultrasonicated for 30 minutes to produce C_3N_4 suspension. In another beaker, 0.15 g of TiNT (for 1:3 C_3N_4:TiNT sample) was dispersed in 500 mL of ultrapure water by ultrasonication and stirring. The well-dispersed suspension was added into the C_3N_4 suspension dropwise under vigorous stirring. The undispersed TiNT bulk was mixed with more water to disperse and added into C_3N_4 suspension later. The resultant mixture was stirred overnight at room temperature. Finally, the white solid was filtered off, washed with a small amount of water, dried at room temperature, and collected. These samples were labelled as a format 'p/g-C_3N_4-TiNT-ratio' like 'p-C_3N_4-TiNT'-1:2, where 'p' means protonation, and 'g' means graphitic. For C_3N_4-TiNT-dop samples, TiNT-dopamine (synthesis procedures were discussed in the previous chapter) was used instead of TiNT in syntheses.

Synthesis of heated C_3N_4-TiNT nanocomposite

The C_3N_4-TiNT samples were transferred into 50 mL crucibles (with cover) and heated under 300 or 400 ^{o}C in a furnace for 4 hours with a heat-up rate of

3K/min. The crucibles were left in the furnace until cooling down to below 50 ^{o}C, and then the resultant powder was collected without further treatment. These samples were labelled as a format ‘p/g-C_3N_4-TiNT-ratio-temperature’, such as ‘p-C_3N_4-TiNT-1:2-400’.

Synthesis of heated TiNT samples

0.5 g of as-prepared TiNT (synthesis procedures were discussed in the previous chapter) was added into a 50mL alumina crucible (with cover) and heated under 150/200/250/300/350/400/450/500/550/600 ^{o}C for 4 hours respectively in a muffle furnace. The heat-up rate was 3K/min for all samples. Then the crucible was left in the furnace until it cooled down to below 50 ^{o}C. The resultant powder was further ground and collected and labelled as TiNT-150, TiNT-200, etc.

Photodegradation of Methylene Blue

The setup of photodegradation is shown in Figure 25. The distance between reactor and light source was controlled at 120 cm, and the light was focused on the middle of the reactor. The current of the lamp was set to 13 A. For the photodegradation under visible light, a 400 nm cut-off filter was applied to the lamp holder. The light intensity was measured by a photoradiometer as 69.7 mW, and the detective pore diameter was 2 cm. The amount of incident light energy upon the detector was calculated as 22.2 mW/cm^2. The area of light illumination on the beaker was estimated as 35 cm^2, and thus the estimation of incident light energy was 0.78 W.

The photodegradation experiments were carried out in the same procedures. In the reactor, which was a quartz beaker, 10 mg of the photocatalyst was firstly weighted out by an analytical balance and mixed with 100 mL of methylene blue solution (10 mg/L), then the mixture was sonicated for 10 minutes for dispersion. Next, the mixture was stirred for 2 hours in darkness, followed by illuminating under light for 5 hours.

For the investigation of the photodegradation pathway, 100 mg of TiO_2 was mixed with 100 mL of methylene blue solution and illuminated under full-range light for 5 hours. Then the solid was filtered off then the filtrate was concentrated and transferred to a small vial for GC-MS testing.

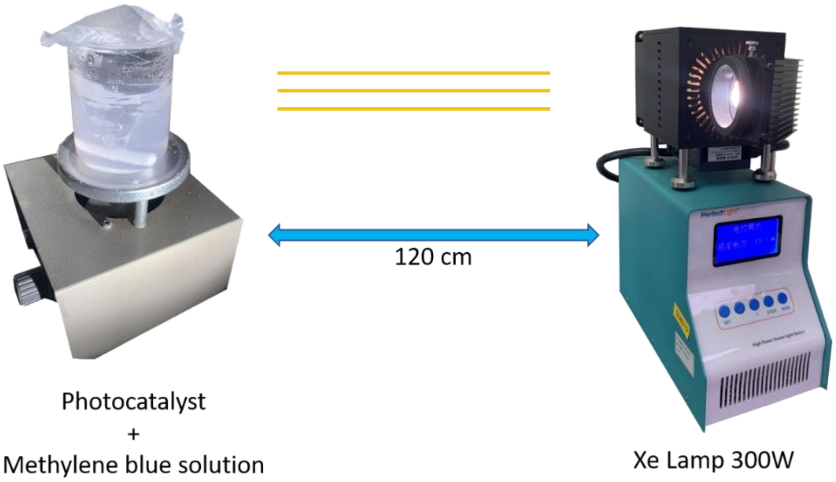

Figure 25 Setup of photodegradation. Total power of Xe lamp is 300 W, and the distance between reactor and lamp is 120 cm.

5.3 Results and Discussions

5.3.1 Protonation of g-C_3N_4

The protonation process aimed to improve the mixing of TiNT and carbon nitride. The Zeta potential of TiNT, g-C_3N_4 and p-C_3N_4 were measured, and the results are shown in Figure 26. TiNT has a negatively charged surface, which has a zeta potential of -27.3 mV. g-C_3N_4 showed a zeta potential of 1.6 mV, which means it has a nearly neutral surface. The zeta potential of p-C_3N_4 was 23.2 mV and proved that the protonation occurred. The alternation of neutral surface to positively charged surface indicated that the protonation could promote the electrostatic adhesion of TiNT and C_3N_4.

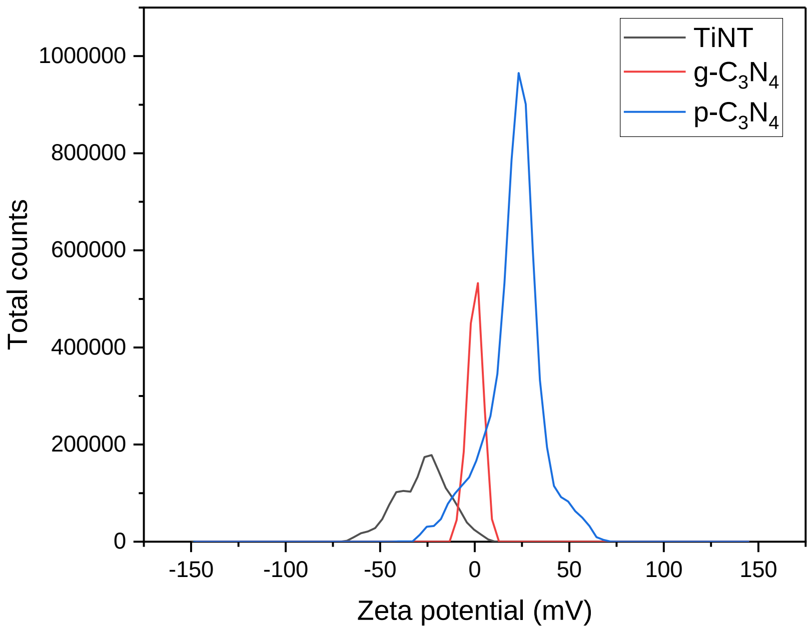

Figure 26 Zeta potential of TiNT (-27.3 mV, a negatively charged surface), g-C_3N_4 (1.6 mV, a nearly neutral surface) and p-C_3N_4 (23.2 mV, a positively charged surface).

For g-C_3N_4, it contains abundant nitrogen with lone pairs. The UV-Vis spectra of protonated C_3N_4 and composite prepared from p-C_3N_4 compared with unprotonated samples are shown in Figure 27 (a) and (b), respectively. From UV-Vis, no obvious difference of absorbance band position could be found for both p-C_3N_4 and the composite prepared from p-C_3N_4, which means the protonation process of g-C_3N_4 did not change the band gap. Figure 28 shows the XRD patterns of p-C_3N_4-TiNT-1:3 compared with the same ratio composite prepared from the unprotonated g-C_3N_4. From the patterns, no obvious differences could be found, which means the protonation process did not change the phase of samples. No property changes have been observed upon protonation, and thus the uses of p-C_3N_4 and g-C_3N_4 were not specifically mentioned in the following discussion.

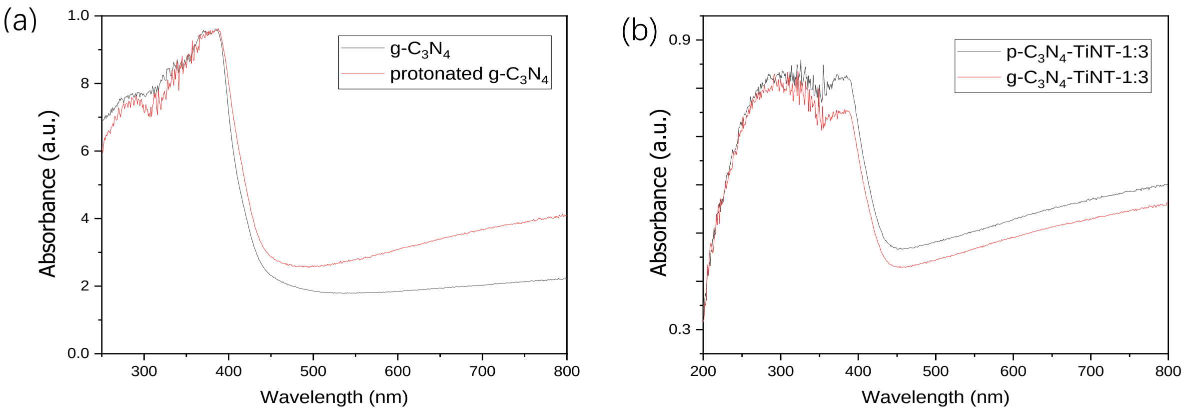

Figure 27 UV-Vis spectrum of (a)p-C_3N_4 compared with g-C_3N_4; (b)p-C_3N_4-TiNT-1:3 compared with g-C_3N_4-TiNT-1:3. No obvious difference of absorbance band position could be found for both p-C_3N_4 and the composite prepared from p-C_3N_4

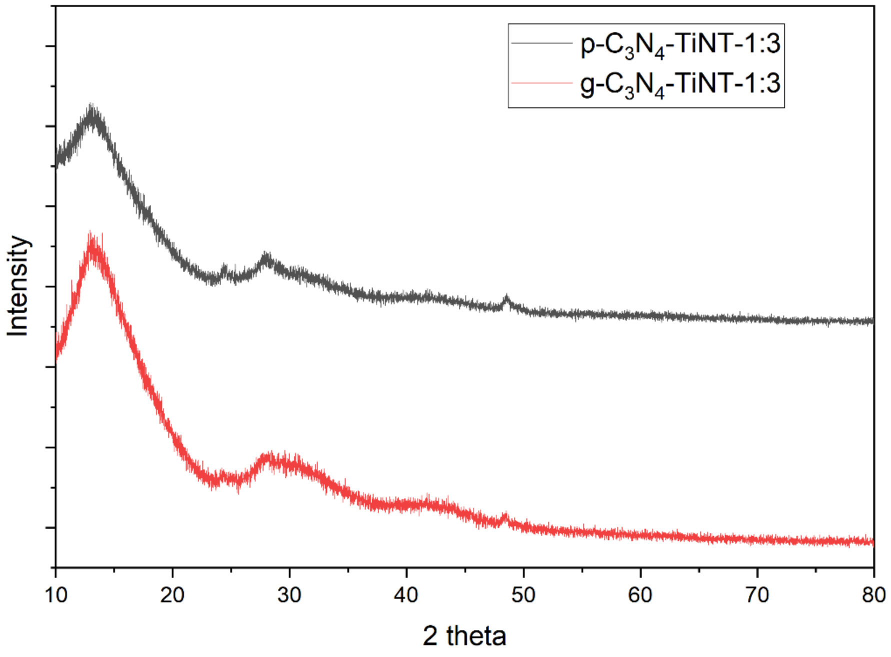

Figure 28 XRD of p-C_3N_4-TiNT-1:3 (top); g-C_3N_4-TiNT-1:3 (bottom). The XRD patterns show no obvious difference, which means the protonation process did not change the phase of samples

5.3.2 Characterization of C_3N_4-TiNT System

Samples were compared in groups. Firstly, composites with various ratios were compared with starting materials. Next, annealed samples were compared with non-annealed samples. Finally, samples prepared from TiNT-dopamine were compared.

UV-Vis Absorbance

UV-Vis absorbance of p-C_3N_4, TiNT, C_3N_4-TiNT-1:2 and C_3N_4-TiNT-1:3 are compared in Figure 29. TiNT shows a band gap of 3.2 eV. For p-C_3N_4, an absorbance band edge was found at 450 nm, which corresponded to a band gap of 2.76 eV. For the two composites, their absorbance bands were close to p-C_3N_4, which means their band gap was dominated by carbon nitride. It also noticed that a small band could be found at around 350 nm, which was attributed to the existence of TiNT.

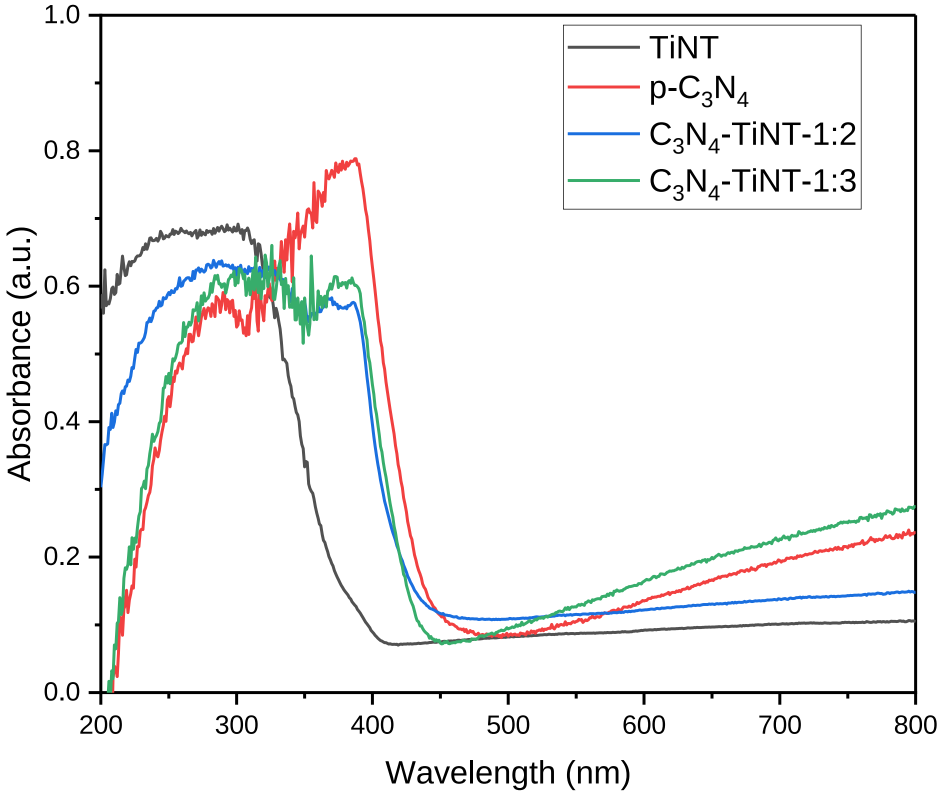

Figure 29 UV-Vis absorbance of TiNT, p-C_3N_4, C_3N_4-TiNT-1:2 and C_3N_4-TiNT-1:3. TiNT shows a band gap of 3.2 eV when the C_3N_4 composites show a similar band gap to carbon nitride, which is 2.76 eV.

UV-Vis absorbance of C_3N_4-TiNT-1:2 and annealed samples which were annealed under 300/400 ^oC were compared in Figure 30. From 250-350 nm, the TiNT profile dominated the absorbance, and it was the same for the three samples. From 350-400 nm, a peak from C_3N_4 was observed. This peak was strongest in the unannealed sample and weakest in the sample annealed under 400 ^oC. This was explained by the loss of C_3N_4 during the annealing process. Within the visible light range, all three samples have shown absorbance before 443 nm. This wavelength corresponds to a band gap of 2.8 eV, which was very close to the band gap of g-C_3N_4. The band gap from UV-Vis was close to the band gap from the Tauc plot shown in Figure 31. The position of the band gap indicated that the g-C_3N_4 absorbance band was dominating in the composite samples.

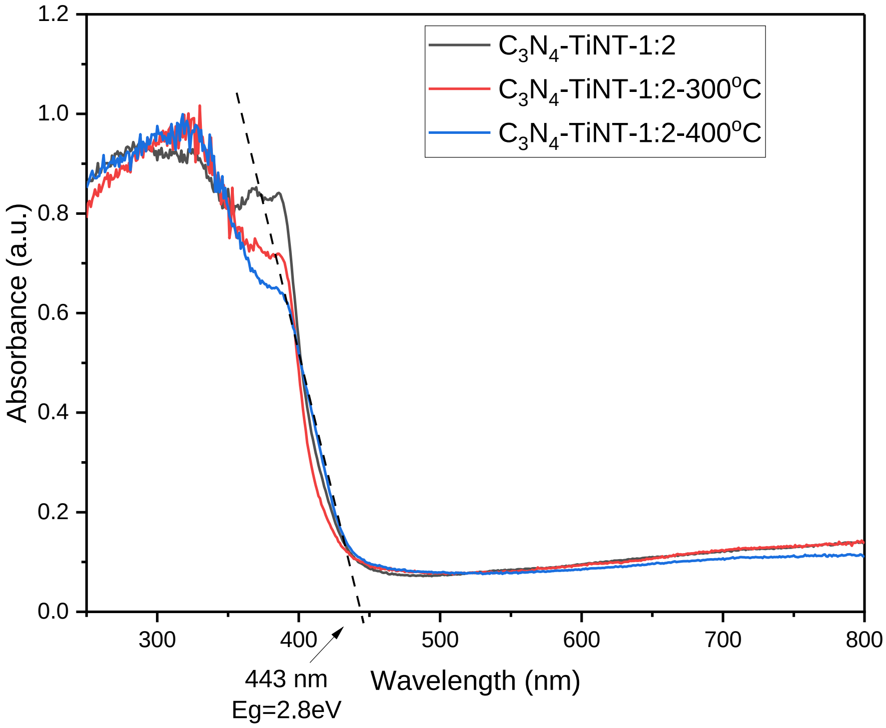

Figure 30 UV-Vis absorbance of C_3N_4-TiNT-1:2, C_3N_4-TiNT-1:2-300°C and C_3N_4-TiNT-1:2-400°C. All samples show the same band gap, which is 2.8 eV.

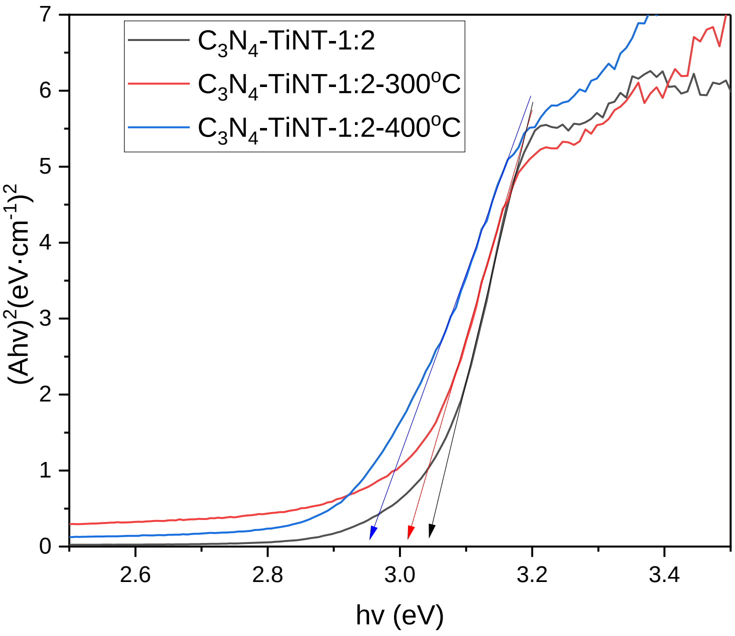

Figure 31 Tauc plots of C_3N_4-TiNT-1:2, C_3N_4-TiNT-1:2-300°C and C_3N_4-TiNT-1:2-400°C

UV-Vis absorbance of TiNT-dopamine, C_3N_4-TiNT-dop-1:2, C_3N_4-TiNT-dop-1:2-300°C and TiNT-dop-1:2-400°C were compared in Figure 32. TiNT-dopamine showed a significant absorbance band in the visible light range, which was due to the formation of the charge transfer complex (also discussed in Chapter 4). For C_3N_4-TiNT-dop-1:2, an absorbance band ended at 450 nm can be found, which was attributed to the band gap of carbon nitride. Moreover, an increase of absorbance from 450nm up to 600 nm could be found. This band was attributed to the presence of TiNT-dop, which indicated that this composite has the potential to show activity under visible light. The bands of C_3N_4-TiNT-dop-1:2-300°C and 400 °C samples were donated by both TiNT-dopamine and carbon nitride, which means these composites contained sub-bands, which may affect their properties.

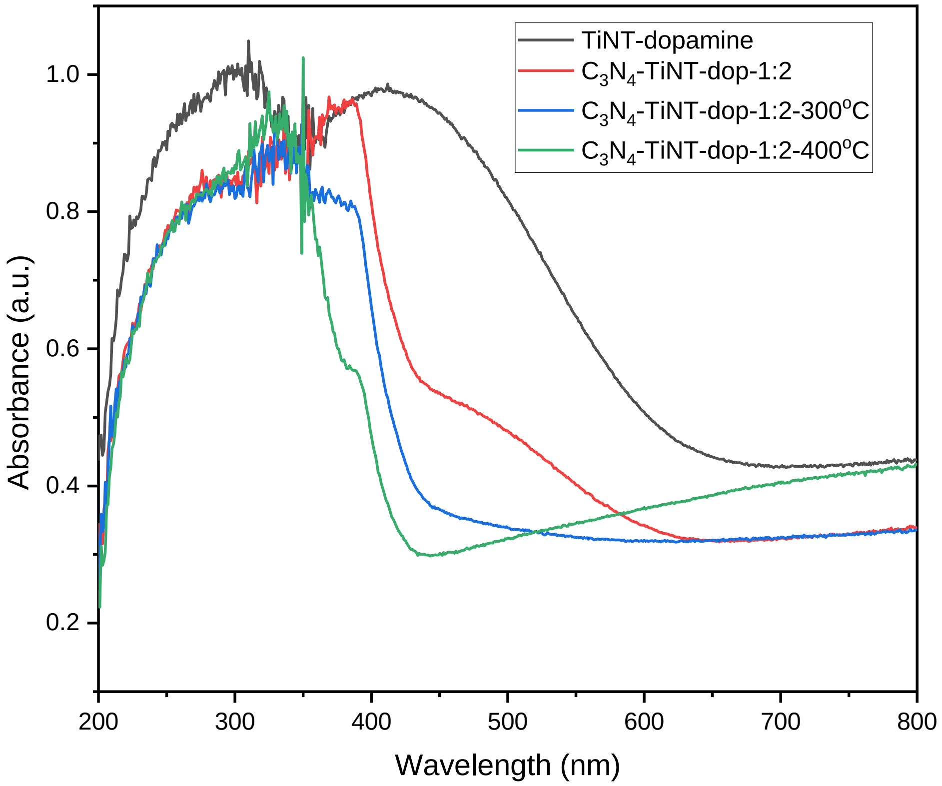

Figure 32 UV-Vis absorbance of TiNT-dopamine, C_3N_4-TiNT-dop-1:2, C_3N_4-TiNT-dop-1:2-300°C and TiNT-dop-1:2-400°C. TiNT-dopamine and C_3N_4-TiNT-dop-1:2 show absorbance in the visible light range. The bands of composites were donated by both TiNT-dopamine and C_3N_4.

Attenuated Total Reflectance – Fourier Transform Infrared Spectroscopy

Attenuated Total Reflectance-Fourier Transform Infrared Spectroscopy (ATR-FTIR) is a method different from normal FTIR. For the ATR method, powder and liquid samples can be directly used, and reflectance is measured. Moreover, based on total reflection, the IR beam reflects from the internal surface of the ATR crystal and creates an evanescent wave into the sample, partially absorbed by the sample, and the reflected light returned. As a result, information on the sample surface can be obtained. In this chapter, the ATR method was used instead of the traditional FTIR method.

ATR-FTIR spectra of heated C_3N_4-TiNT composites compared to g-C_3N_4 are shown in Figure 33. Overall, the samples with higher TiNT content showed a poorer signal-noise ratio because TiNT lacks bond vibrations; thus, its signal is low. The peaks were assigned as follows: The peak at 810 cm^{-1} was attributed to the breathing mode of tri-s-triazine[137] (monomer unit of g-C_3N_4), which is a characterization peak of g-C_3N_4. The peaks in the range from 1200 to 1650 cm^{-1} were attributed to stretching modes of CN heterocycles[138]. These peaks, along with the characterization peak, indicated that the basic structure of g-C_3N_4 did not change upon protonation, mixing, and heating process. Meanwhile, the sharp peak at 890 cm^{-1} from the 3:1 sample and g-C_3N_4 was assigned as deformation mode of N-H in amino groups[139], and the broad peaks in the range of 3000-3300 cm^{-1} were attributed to amino groups exists in the samples[138], as well as O-H bond from surface adsorbed water. However, these bands cannot be found in C_3N_4-TiNT 1:2 samples. It was proposed that as C_3N_4 was in excess in the 3:1 sample so the peaks can be seen.

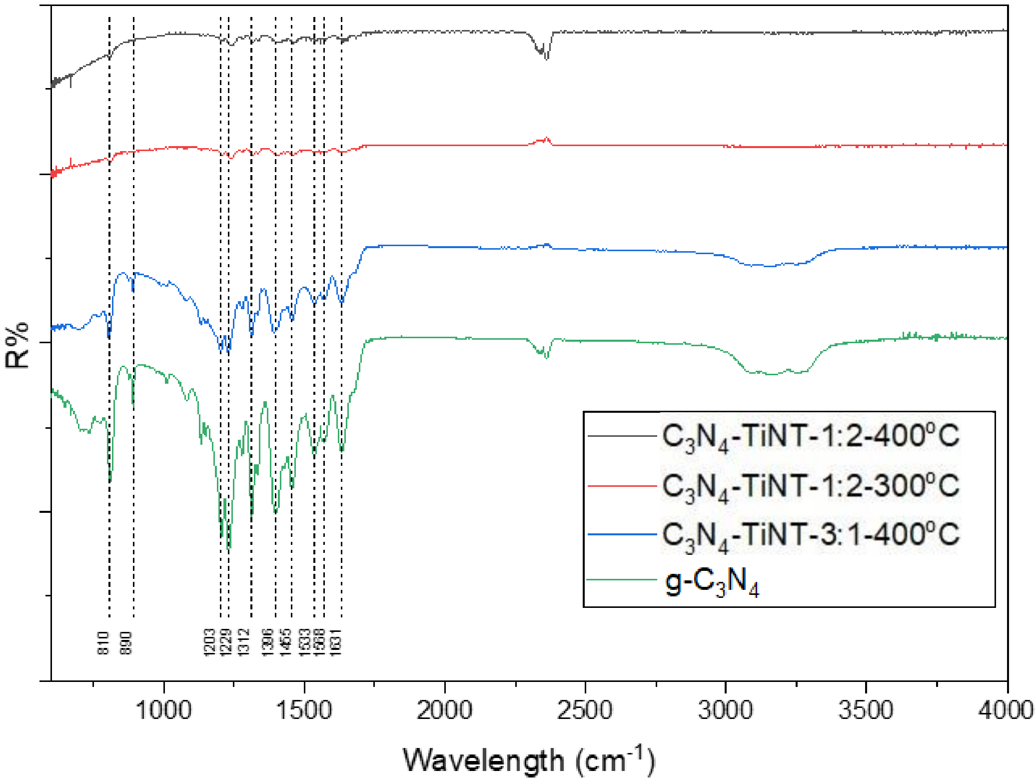

Figure 33 ATR-FTIR spectrum of g-C_3N_4, C_3N_4-TiNT-3:1-400°C, C_3N_4-TiNT-1:2-300°C, and C_3N_4-TiNT-1:2-400°C. The peak at 810 cm^{-1}: breathing mode of tri-s-triazine[137]; 890 cm^{-1}: deformation mode of N-H in amino groups[139]; 1200-1650 cm^{-1}: stretching modes of CN heterocycles[138]; 3000-3300 cm^{-1}: amino groups[138] exists in the samples, and O-H bond from surface adsorbed water.

TEM

For showing the changes in morphology and crystal structure, TEM images of a composite sample C_3N_4-TiNT-1:1 before and after heating are shown in Figure 34 (a)-(c). From Figure 34 (a) & (b), it was found that the tubular structure of TiNT was clear, which meant TiNT structure did not change upon mixing. Aggregated nanotubes were found because they are hard to disperse. The morphology of C_3N_4 was small nanosheets that overlapped with each other and TiNT. After heating under 550°C, as Figure 34 (c) shows, no tubular structures could be found, but lots of nanoparticles appeared. These particles were anatase transformed from TiNT, and the HRTEM of these particles are shown in Figure 34 (d). The d-spacing of the nanoparticle was found to be around 0.35 nm, which corresponded to the (101) surface of anatase as described above. Carbon nitride nanostructure could not be seen due to the decomposition of C_3N_4 heated under 550°C for 4 hours, and that was why composite samples were not heating to such a high temperature.

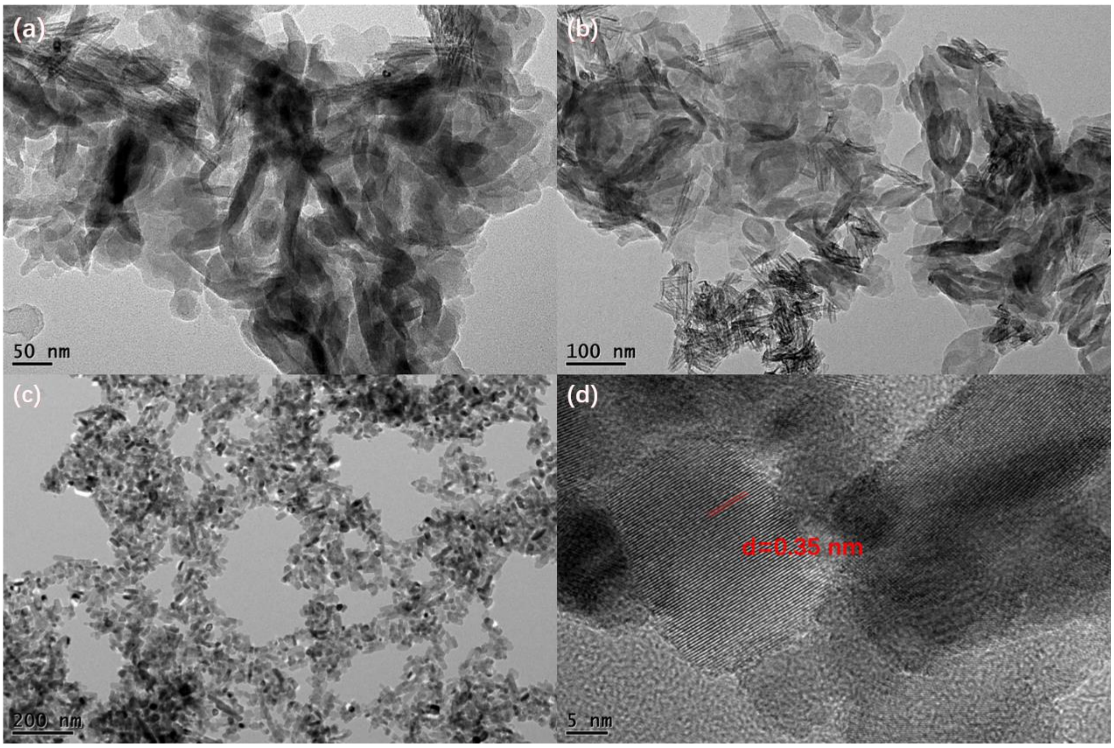

Figure 34 (a)-(b) TEM of C_3N_4-TiNT-1:1; (c) TEM of C_3N_4-TiNT-1:1 heated under 550^{o}C; (d) HRTEM of C_3N_4-TiNT-1:1 heated under 550^{o}C. (a) and (b) shows the morphology of TiNT did not change upon mixing. (c) shows the disappearance of tubular structures and the appearance of nanoparticles. (d) shows the d-spacing of nanoparticles which is 0.35 nm and corresponds to the (101) surface of anatase.

TEM and HRTEM images of C_3N_4-TiNT-dop-1:2, C_3N_4-TiNT-dop-1:2-300^{o}C and C_3N_4-TiNT-dop-1:2-400^{o}C are shown in Figure 35 (a) – (f). Figure 35 (a) and (b) show the sample before annealing. The tubular structure of TiNT and the nanosheet of C_3N_4 were found, which was similar to the images in Figure 34 (a) & (b). At this stage, no TiO_2 particles were observed from TEM. When this sample was annealed under 350 ^{o}C, from Figure 35 (c) - (d), the morphology of nanosheet and nanotubes did not change when few nanoparticles were found. The HRTEM of these nanoparticles gave a d-spacing of 0.37 nm, and the formation of nanoparticles was attributed to the transformation from TiNT to TiO_2 at the beginning stage. When the sample was annealed under 400 ^oC, a large number of nanoparticles were found along with TiNT and C_3N_4. HRTEM showed good crystalline of the nanoparticles with a d-spacing of 0.35 nm, which corresponded to the (101) surface of the anatase.

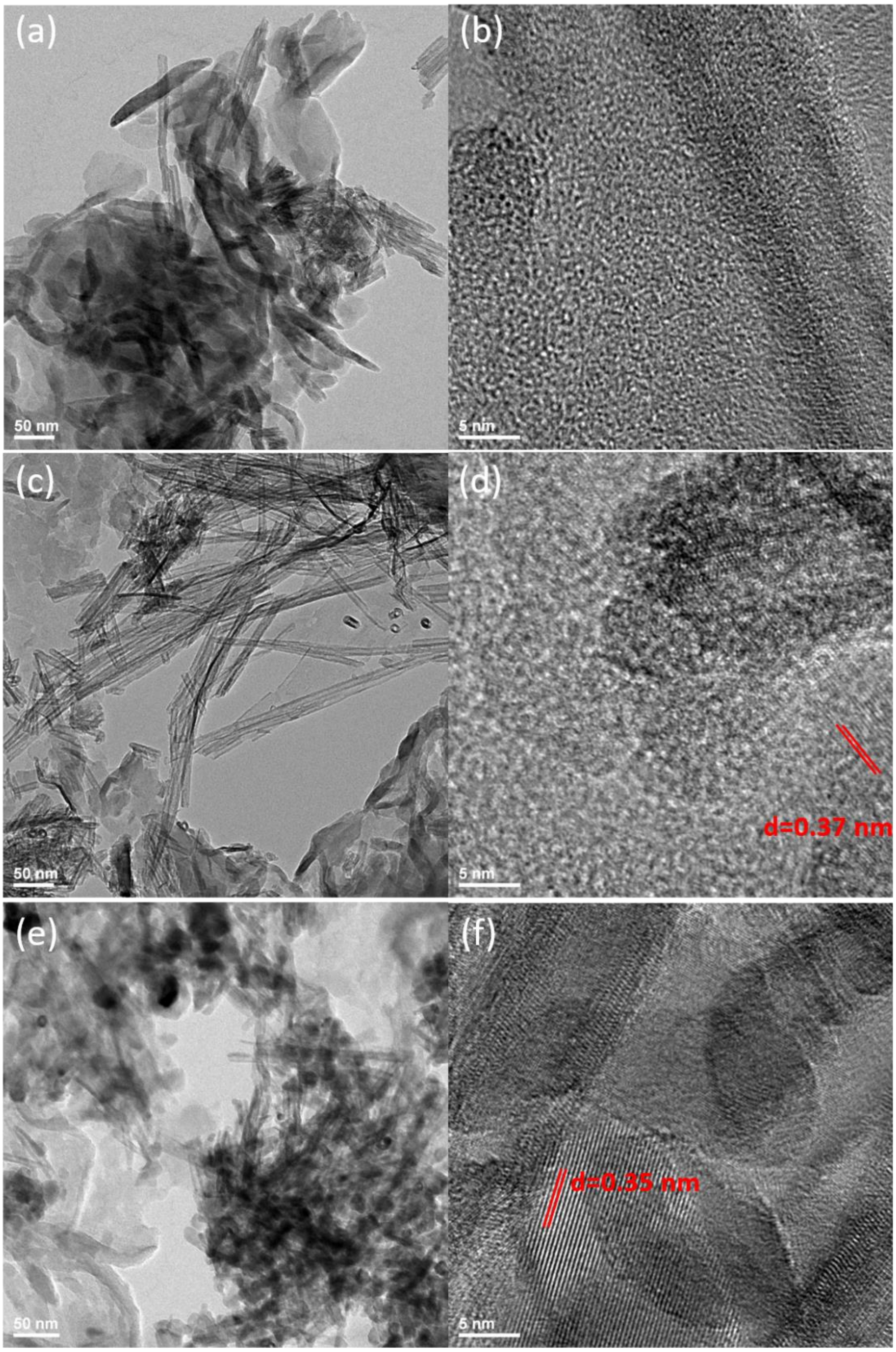

Figure 35 TEM (left) and HRTEM (right) images of (a)&(b): C_3N_4-TiNT-dop-1:2; (c)&(d): C_3N_4-TiNT-dop-1:2-300°C; (e)&(f): C_3N_4-TiNT-dop-1:2-400°C. (a) and (b) show the morphology of TiNT and C_3N_4 in the composite. (c) and (d) show the appearance of nanoparticles when the morphology of nanotubes and nanosheets did not change after annealing at 300 °C. (e) and (f) show the existence of nanoparticles with a d-spacing of 0.35 nm, which corresponded to the (101) surface of anatase.

XPS

XPS of C_3N_4-TiNT-1:2, C_3N_4-TiNT-dop-1:2 and their heated samples were measured and compared. The XPS results were calibrated by the C1s peak at 288.4 eV, which was given by external carbon for calibration purposes. Ti2p, N1s, O1s, C1s, and valence band were measured, and the results were discussed as follow.

Ti2p of the composites are shown in Figure 36. All six samples show the same Ti2p profile as TiNT: peak at 458.8 eV was assigned as Ti2p$_{3/2}$; peak at 464.5 was assigned as Ti2p$_{1/2}$; peak at 471.6 eV was assigned as Ti2p satellite peak. The spin-orbit splitting value between Ti2p$_{3/2}$ and Ti2p$_{1/2}$ was 5.7 eV, and the area ratio Ti2p$_{3/2}$:Ti2p$_{1/2}$ was 2:1, which fitted the common splitting value and area ratio of Ti^{4+} in titanium dioxide.[140] After heating and modification, the ratio of the three peaks remained the same, and the Ti2p$_{3/2}$ peak of all samples showed similar FWHM (1.15-1.3) to each other's when the positions of peaks shifted slightly (~0.1 eV). Considering the low resolution of the XPS machine, the shifting was not proposed as any changes of samples. Thus, the oxidation state of titanium in the composites did not change upon modification and heating.

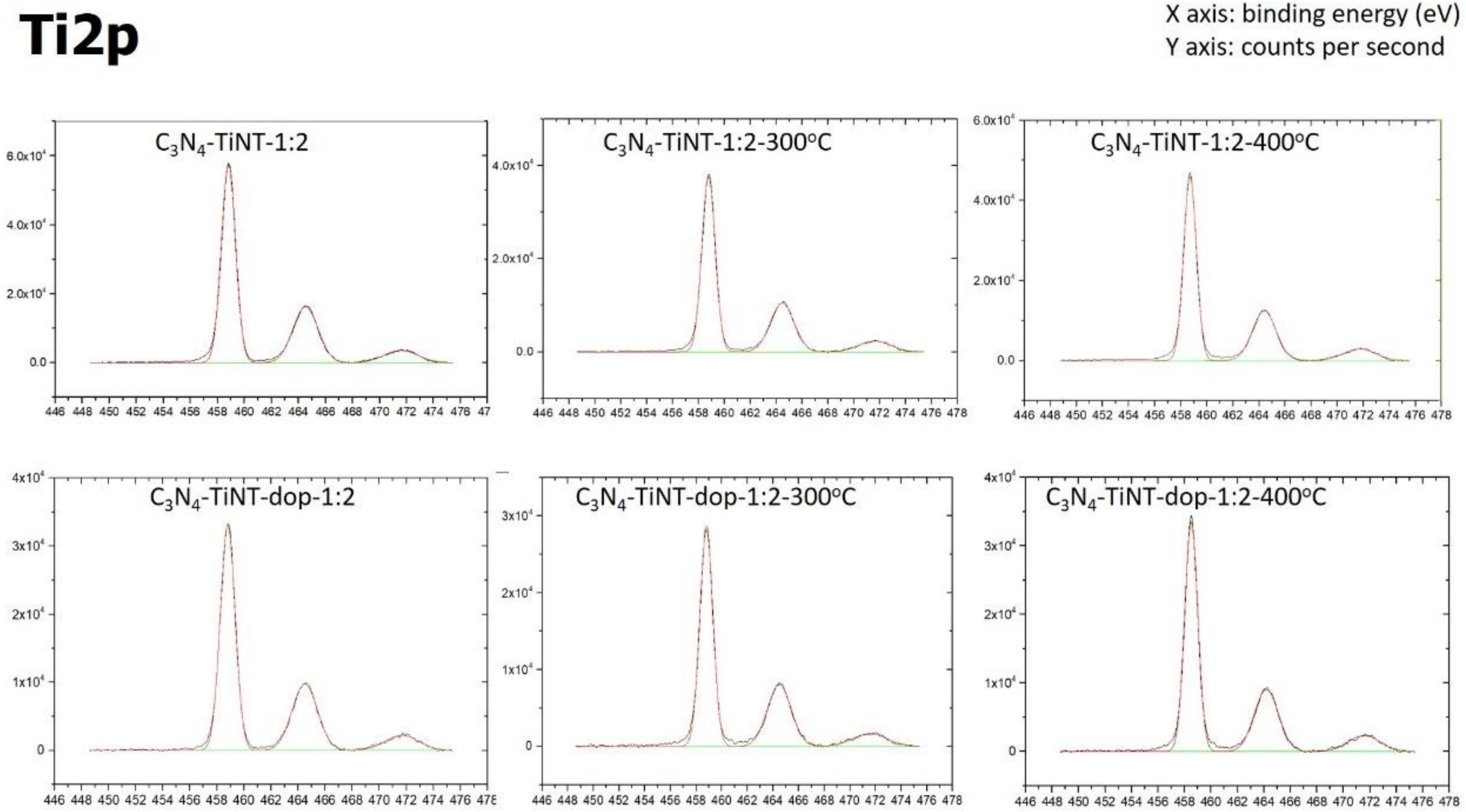

Figure 36 XPS Ti2p of C_3N_4-TiNT and C_3N_4-TiNT-dop Composites

N1s of the composites are shown in Figure 37. Four peaks for each sample were fitted and assigned.[140-142] The peak at 398.9 eV was assigned as pyridine N (C-N=C); the peak at 399.7 eV was assigned as pyrrolic N (C-NH); the peak at 401.5 eV was assigned as graphitic N (N-C3). The ratio of these three peaks did not change upon modification and heating. The peak at 404.9 eV was assigned as weak π-π* satellite features caused by the structure of nitrogen-containing aromatic polymers[140]. All the peaks showed the profile of g-C_3N_4, and no signal could be found for the nitrogen in the dopamine structure. This could be caused by the low loading amount (~ 5 wt.%) of dopamine in the TiNT-dopamine of the composites. It was mentioned in literature[141] that the shifting of peaks was reflecting the interfacial interaction between g-C_3N_4 and hollow box-shaped TiO_2, which would promote the electron transfer and therefore improve the photocatalytic efficiency[141]. However, no obvious shifting was observed for the composites. The small shifting (0.1 eV) could be electron density changes due to the formation of composites.

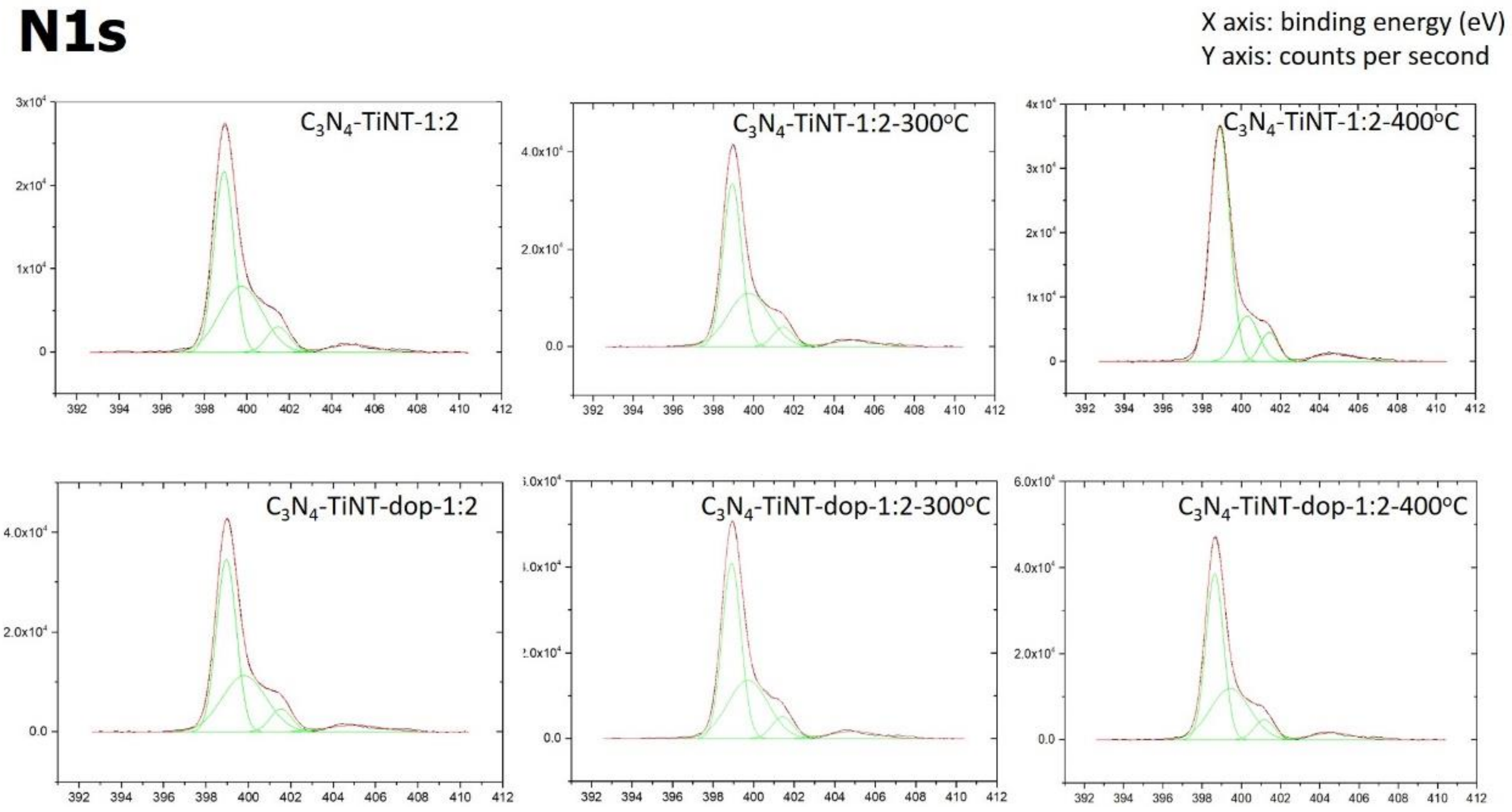

Figure 37 XPS N1s of C_3N_4-TiNT and C_3N_4-TiNT-dop Composites

O1s of the composites are shown in Figure 38. Two main peaks were fitted and assigned: the peak at 530.3 eV was a typical TiO_2 peak[143], and the peak at 531.2 eV was assigned as Ti-OH species[142]. The spin-orbit splitting value of these two peaks was 0.9-1.0 eV. For the samples which were unheated and heated under 300 ^oC, the area ratio of the TiO_2 peak to the Ti-OH peak was 3:2. However, this ratio was 2:1 for the samples heated under 400 ^oC. The changes in the ratio were explained by the loss of surface water as well as the transformation from $H_2Ti_3O_7$ to anatase, which led to a reduced amount of Ti-OH species in samples.

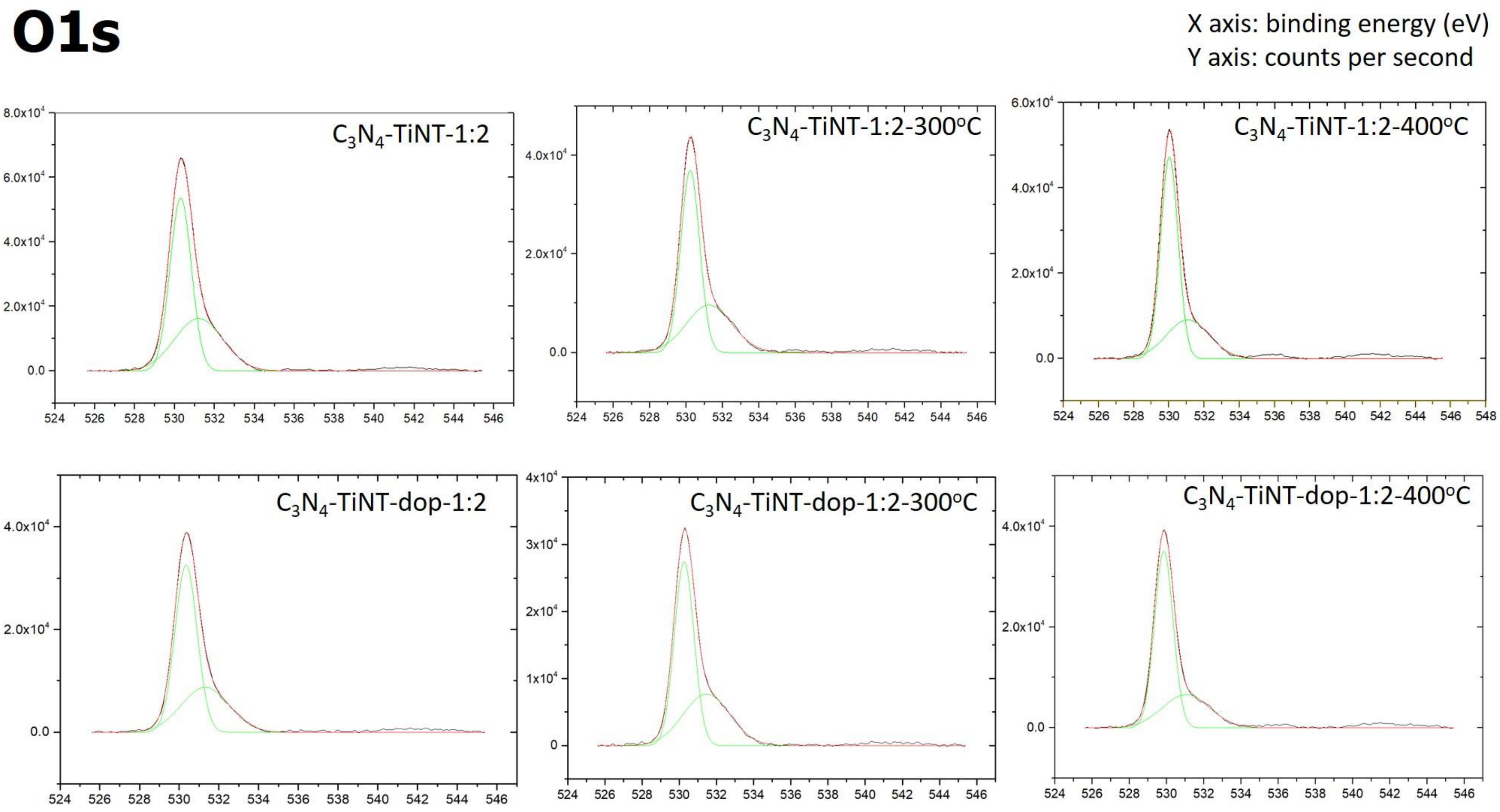

Figure 38 XPS O1s of C_3N_4-TiNT and C_3N_4-TiNT-dop Composites

C1s of the composites are shown in Figure 39. The peak at 288.4 eV was a C-C peak from carbon which was externally added as a calibration reagent. The peak at 284.8 eV was assigned as N-C=N, and the peak at 286.5 eV was assigned as a C-N peak.[142] The assignment of these two peaks fitted the result from N1s spectra. No Ti-C signal, which is normally around 282 eV[142], was found for the composites. That means no Ti-C bond formed on the surfaces of samples during modification and heating.

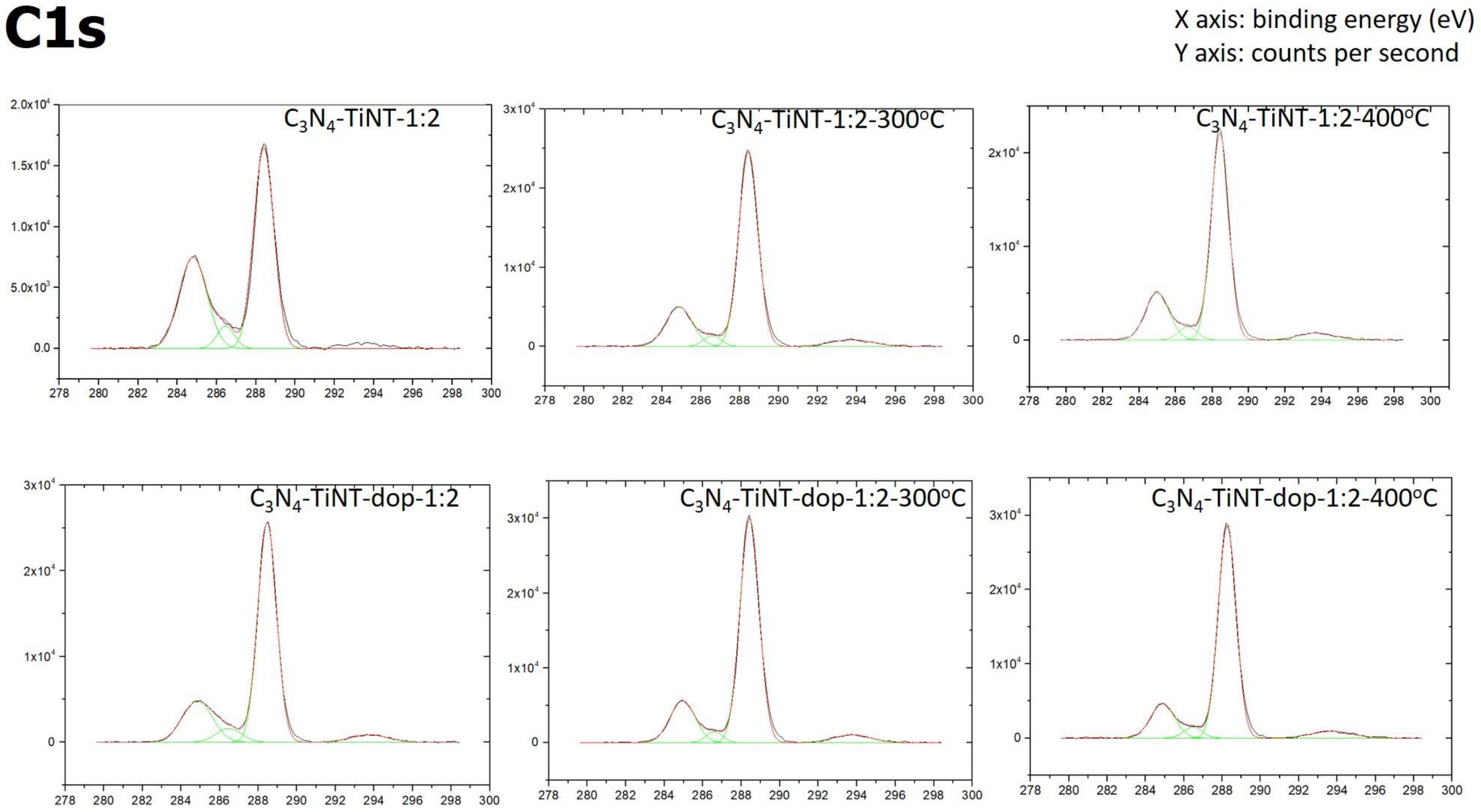

Figure 39 C1s of C_3N_4-TiNT and C_3N_4-TiNT-dop Composites

Band Position

The positions of CB and VB of TiNT were calculated based on the results of XPS-VB and UV-Vis. The valence band position from XPS-VB was 2.3 eV (shown in Figure 40) when the band gap of TiNT was 3.2 eV. Thus, the conduction band was at -0.9 eV. Similarly, the valence band and conduction band position of C_3N_4 was 1.0 eV and -1.76 eV, respectively. The band diagram of the C_3N_4-TiNT composite is shown in Figure 41.

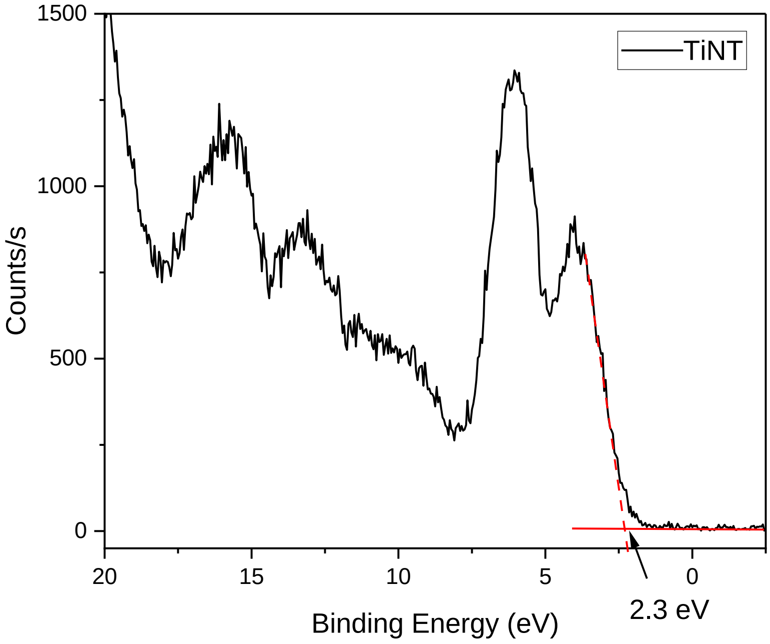

Figure 40 XPS-VB of TiNT. The valence band position of TiNT was 2.3 eV. The band gap of TiNT was 3.2 eV, and thus the conduction band was proposed to be at -0.9 eV.

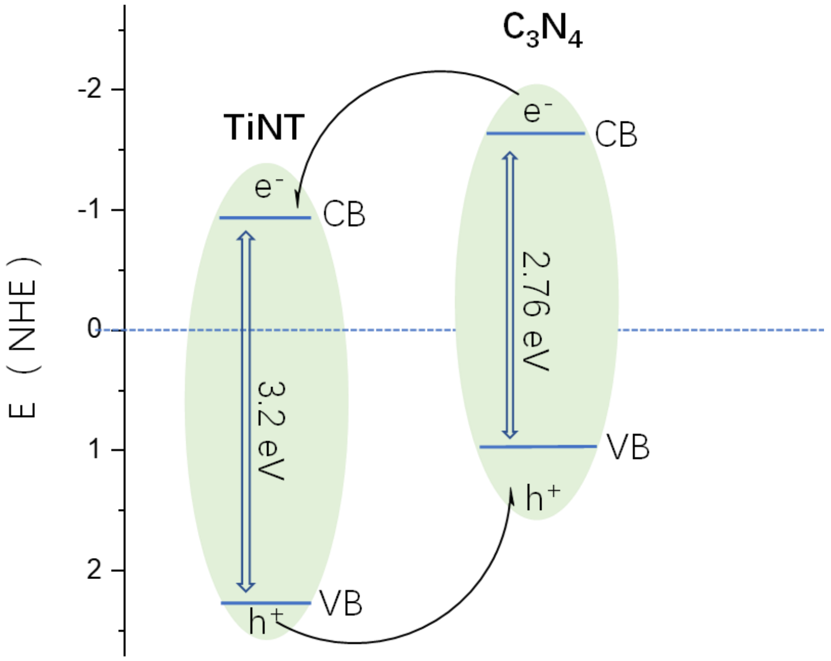

Figure 41 Band diagram of C_3N_4-TiNT composite. The band positions were proposed from XPS-VB spectra and band gaps of TiNT and C_3N_4.

The valence band position of C_3N_4-TiNT nanocomposites was attempted to be directly measured by XPS-VB. Two examples are shown in Figure 42. However, the resultant number was even larger than TiNT's valence band energy. It was proposed that the results did not make sense because no bonds formed between the C_3N_4 and TiNT, and the composites contained sub-band. Therefore, XPS-VB was not a suitable method for measuring the valence band positions of composites directly. DFT calculation can be used for identifying valence band position. However, it is not suitable for the composites due to the difficulty of identifying the model structure. Electrochemistry may be a suitable method. In our preliminary attempts, the position of the valence band was not successfully measured by the CV method. The reasons were proposed to be the poor conductivity and large band gap of composites.

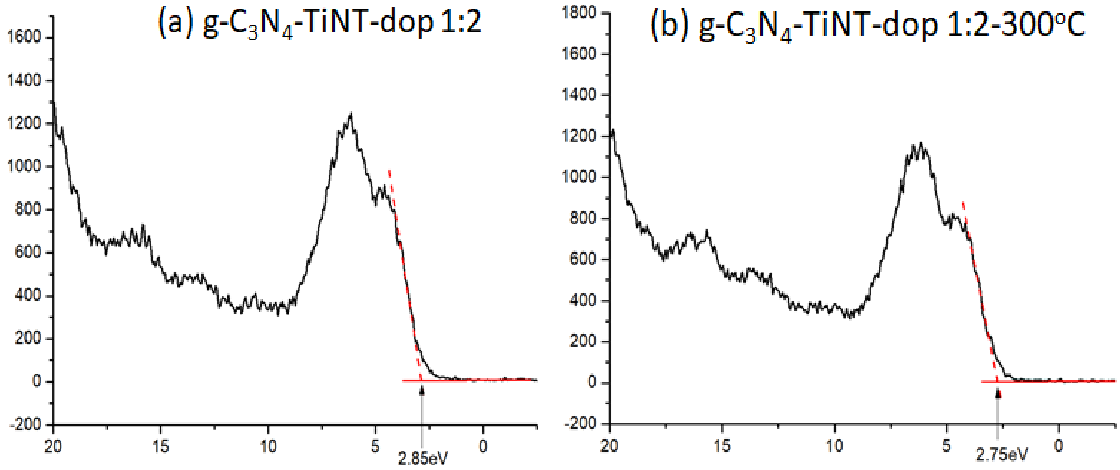

Figure 42 XPS-VB of (a) g-C_3N_4-TiNT-dop 1:2; (b) g-C_3N_4-TiNT-dop 1:2-300°C

X-Ray Diffraction

The XRD patterns of 1:2 ratio samples heated under 300/400 °C were compared with anatase and C_3N_4 and shown in Figure 43. For the 300°C sample, the intensity of peaks was low due to the low crystallinity of TiNT. However, when heated under 400 °C, obvious anatase peaks could be found with a larger breadth compared to pure anatase, and the breadth was because of sample size was in nanoscale. Carbon nitride peaks can hardly be seen in the composite samples, although C_3N_4 dominated the band gap of C_3N_4-TiNT. Figure 44 shows XRD patterns of 3:1 ratio samples. Similarly, the samples heated under 400°C gave better anatase signals than 300°C samples. The main difference was that C_3N_4:TiNT 3:1 samples had shown distinct g-C_3N_4 peaks with high intensity due to a higher level of C_3N_4 content. The XRD patterns have supposed that the crystal structure of carbon nitride was not changing upon heating to 400°C, and this was also supported by ATR-FTIR. What is more important, the appearance of anatase peaks in the annealed composites indicated that TiNT could transform to anatase under high temperatures. Based on this phenomenon, TiNT was annealed under different temperatures to find out the changes upon annealing.

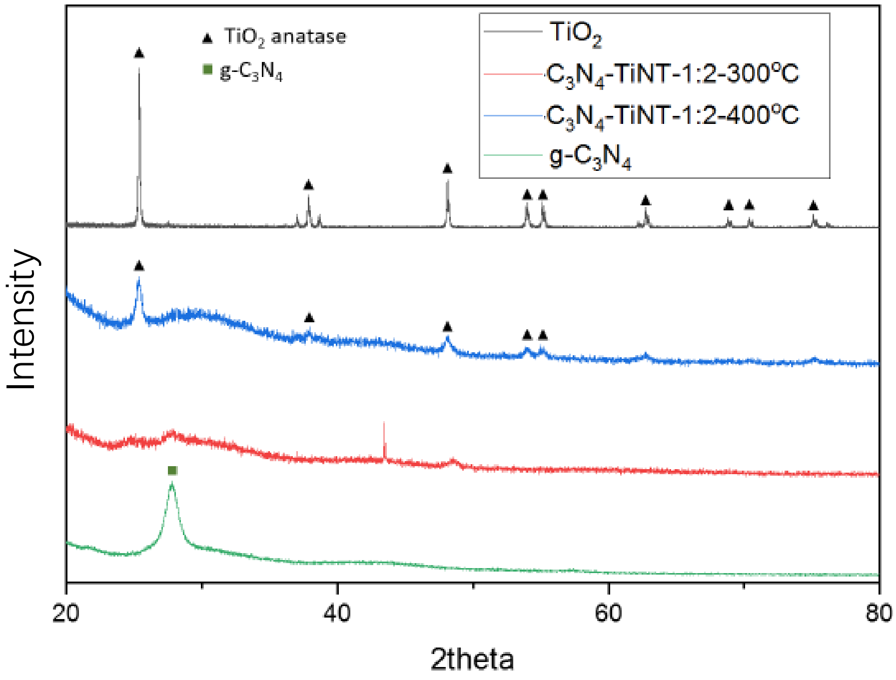

Figure 43 XRD patterns of TiO_2, g-C_3N_4, C_3N_4-TiNT-1:2-300°C and C_3N_4-TiNT-1:2-400°C. The composite annealed at 400 °C shows strong signals of anatase TiO_2 due to the transformation from TiNT to TiO_2 when the composite annealed at 300 °C shows poor signals due to the low content of TiO_2.

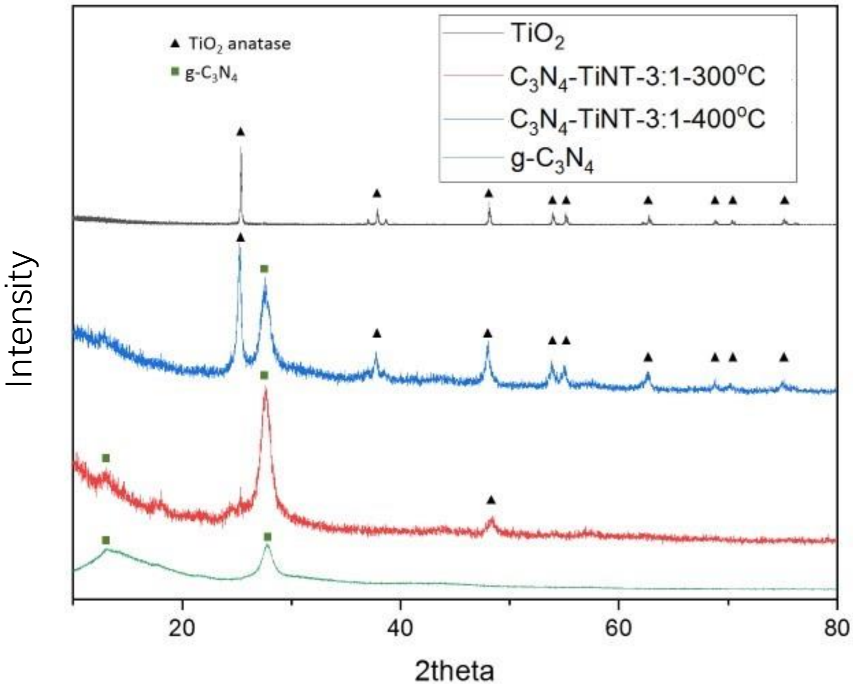

Figure 44 XRD patterns of TiO_2, g-C_3N_4, C_3N_4-TiNT-3:1-300°C and C_3N_4-TiNT-3:1-400°C. The composite annealed at 300 °C shows strong C_3N_4 peaks, but the intensities of anatase peaks are low. The composite annealed at 400 °C show strong anatase signals.

5.3.3 Investigation of Annealed TiNT

Optical Properties

Figure 45 shows photos of TiNT and heated samples. No colour change occurred during the heating process. The white colour fitted the UV-Vis absorbance of samples shown in Figure 46. All samples show poor absorbance in the visible light range (~380 nm – 800 nm) and have absorbance drops from ~300nm to 380 nm. The tangent of linear absorbance range has shown that the band gap was 3.1 eV, which was calculated from Eg (eV)=1240/λ. This method was used to estimate the band gap of the semiconductor.

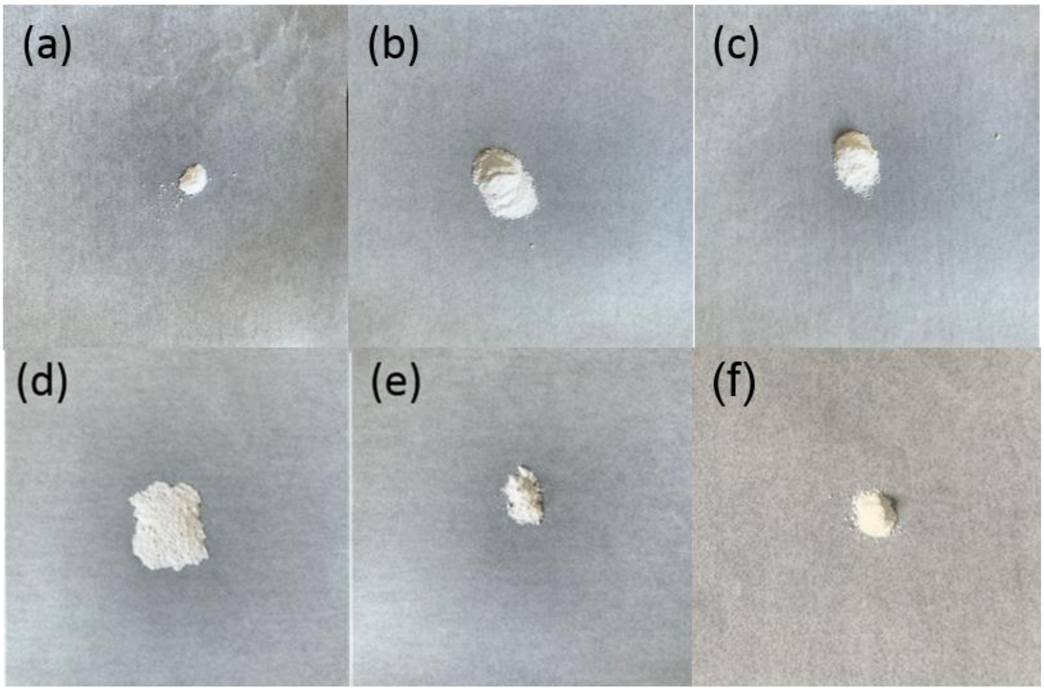

Figure 45 Photos of TiNT and heated TiNT samples (a) TiNT; (b) TiNT-150; (c) TiNT-250; (d) TiNT-350; (e) TiNT-450; (f) TiNT-550

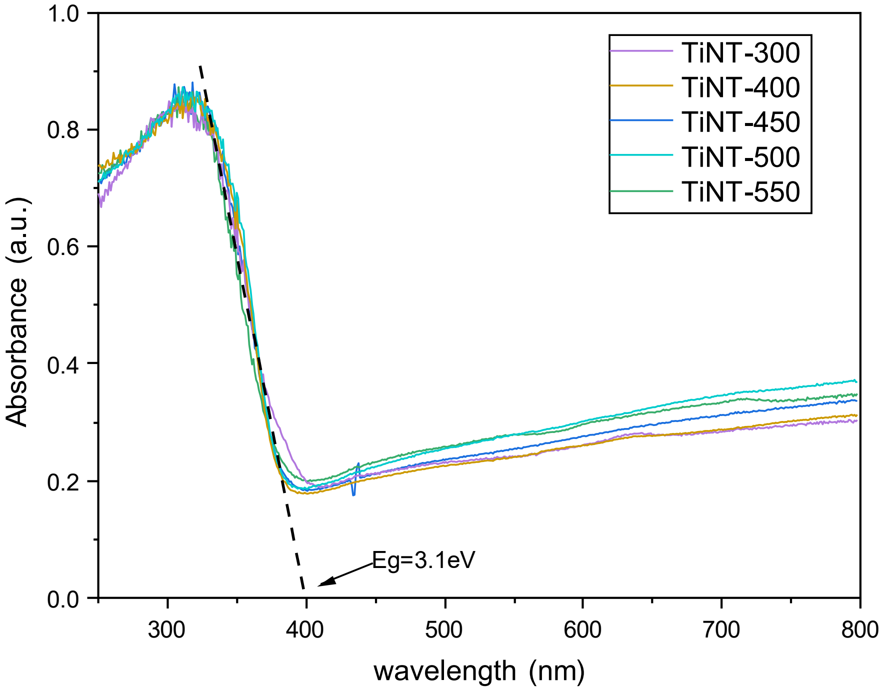

Figure 46 UV-Vis absorbance of TiNT and heated TiNT samples. Samples have no significant difference in absorbance, and the band gap of TiNT did not change upon annealing.

X-Ray Diffraction

To investigate the phase transformation of TiNT under heating, X-Ray Diffractions of a series of heated samples were measured and compared with TiNT and anatase TiO_2, as Figure 47 shows. TiNT (also discussed in Chapter 4) has shown peaks at 25.5^o, 28.4^o, 38.0^o and 48.2^o, which stood for (110), (310), (113), and (020) planes, respectivley[68]. The intensity, as well as signal to noise ratios of these peaks, were very low due to the poor crystallinity of nanotubes, and the peaks were broad because the size of tubes was nanometre level. When TiNT was annealed to up to 350 ^{o}C, the XRD did not show much difference from TiNT itself. However, when TiNT was annealed at 400 ^{o}C, the peaks showed differences in the aspect of intensity, signal to noise ratio, and broadness. When the annealing temperature reached 500 ^{o}C, the peaks could be assigned as anatase TiO_2 at 25.4^o, 37.0^o, 37.9^o, 38.7^o, 48.1^o, 53.9^o and 55.1^o, standing for (101), (103), (004), (112), (200), (105) and (211). The changes of peaks were caused by the destruction of the tubular structure and the formation of anatase crystals. The transformation in nanoscale was also found via the Transmission Electron Microscope (TEM).

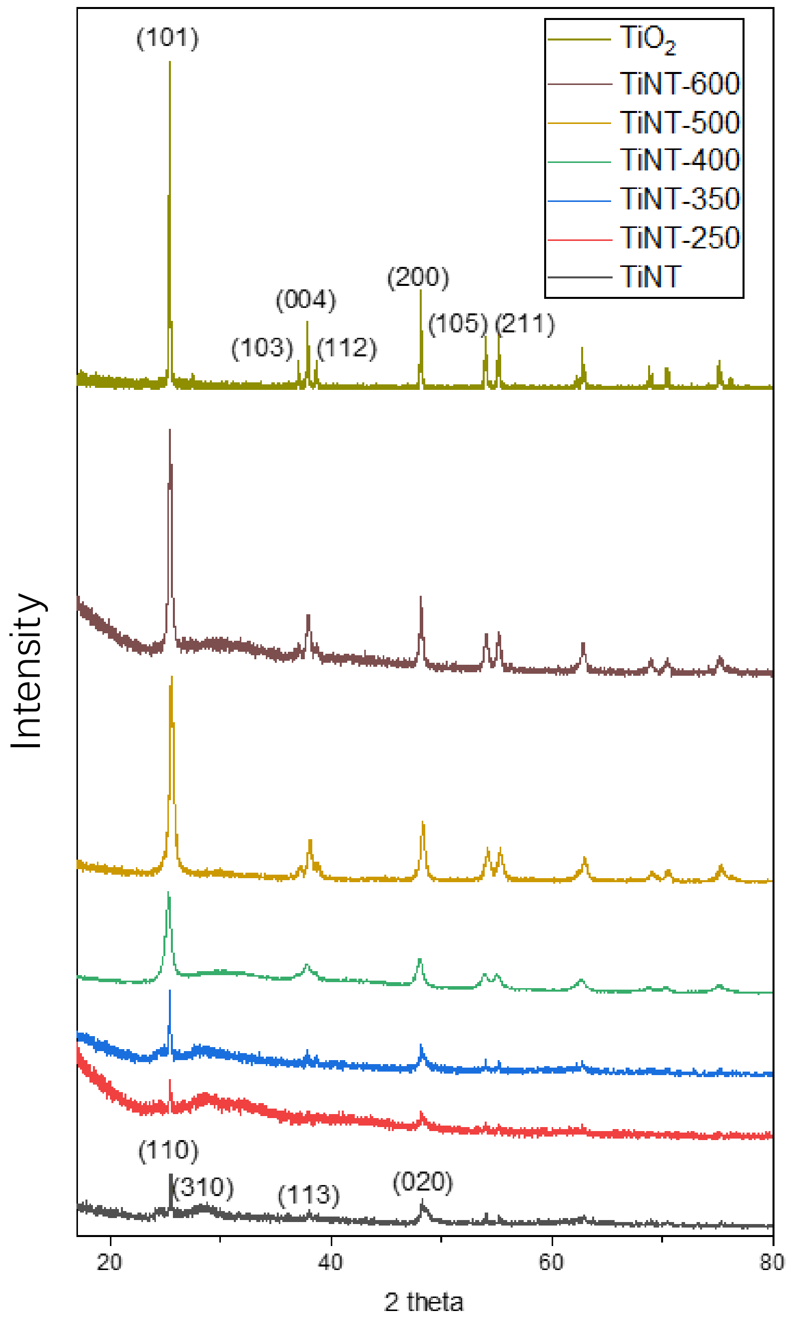

Figure 47 X-Ray Diffraction of TiNT, heated TiNT, and TiO_2. TiNT shows peaks at 25.5°, 28.4°, 38.0° and 48.2°, which stand for (110), (310), (113), and (020) planes, respectivley[68]. Anatase TiO_2 shows peaks at 25.4°, 37.0°, 37.9°, 38.7°, 48.1°, 53.9° and 55.1°, which stand for (101), (103), (004), (112), (200), (105) and (211). The annealing process of TiNT leads to the destruction of the tubular structure, and the formation of anatase crystal and stronger anatase signals can be observed for the TiNT annealed at higher temperatures.

Transmission Electron Microscopy

TEM and High Resolution TEM (HRTEM) were used to find out the morphology changes and crystalline changes of TiNT (shown in Figure 48(a)) and an annealed sample TiNT-550 (shown in Figure 48 (b)-(d)). TiNT has shown a tubular structure with a diameter of ~10nm and a length of ~100nm. However, TiNT-550 has shown three morphologies: long tubes like TiNT, small nanosheets, and nanoparticles. The long tubes were dehydrated TiNT keeping the morphology and transforming to rods. They had poor crystalline; thus, their XRD peaks were covered by anatase. The formation of small nanosheets was explained by unrolling of nanotubes powered by dehydration under high temperatures. The d-spacing of nanoparticle was measured as ~0.34 nm, which corresponded to the (101) surface of anatase when a d-spacing of nanotube was ~0.19 nm, which corresponded to the (020) surface[68] of TiNT.

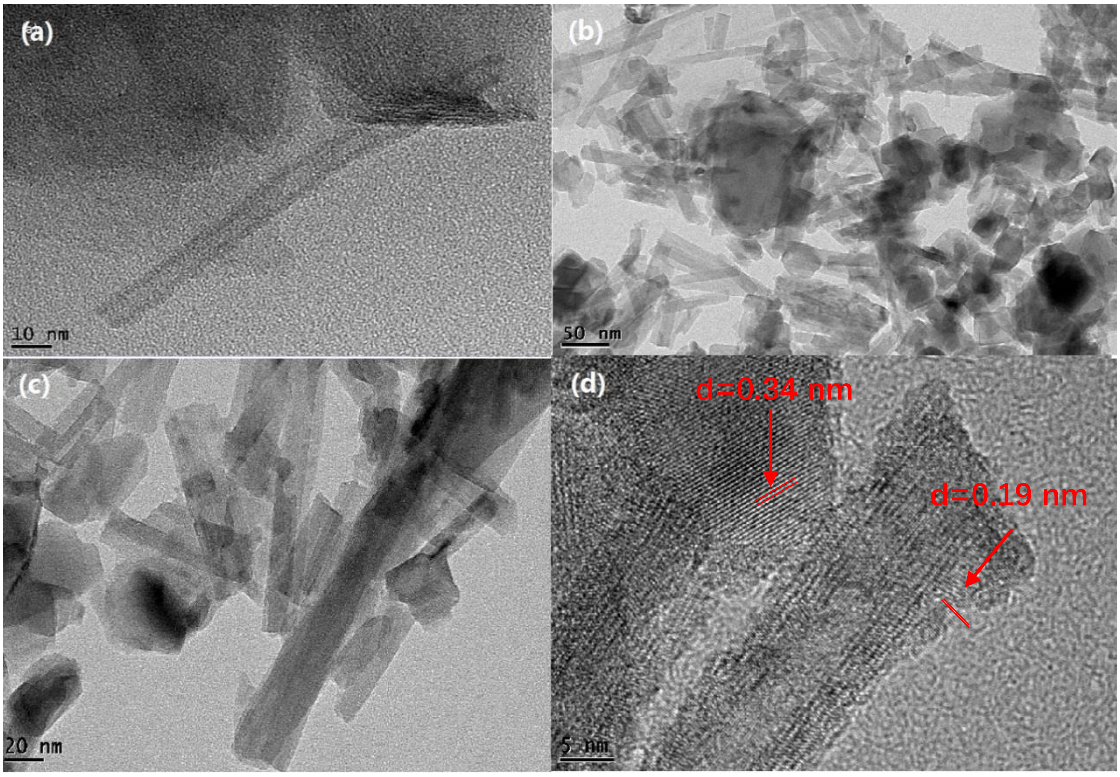

Figure 48 (a) TEM image of TiNT; (b)-(d) TEM and HRTEM images of TiNT-550. TiNT shows a tubular structure with a diameter of ~10nm and a length of ~100nm. TiNT-550 has shown three morphologies: long tubes like TiNT, small nanosheets, and nanoparticles. The d-spacing of nanoparticle was measured as ~0.34 nm, which corresponded to the (101) surface of anatase when a d-spacing of nanotube was ~0.19 nm, which corresponded to the (020) surface[68] of TiNT.

X-ray Photoelectron Spectroscopy

X-ray Photoelectron Spectroscopy (XPS) was used to investigate if the binding energies of the heated sample were different from TiO_2 or TiNT. From Figure 49, it can be seen that the peaks of TiO_2 and TiNT were highly overlapped with each other when TiNT-550 peaks have shifted 0.1 eV to lower binding energy. From TiNT to anatase, the oxidation state of Ti does not change; thus, this shift was considered to be a system error of the XPS equipment instead of changes in binding energy.

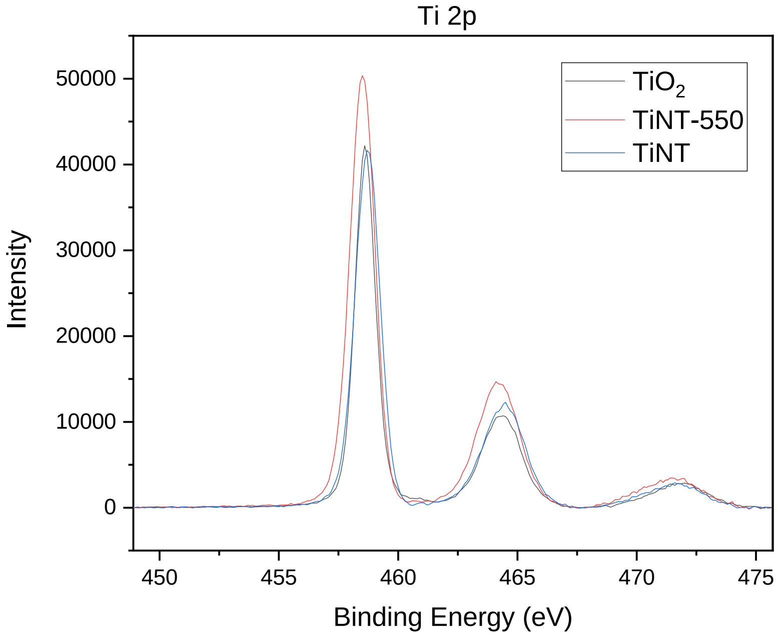

Figure 49 Binding energy of TiO_2, TiNT and TiNT-550

The above results have given a conclusion that TiNT can transform to anatase phase by heating with no changes in surface properties like optical absorption and binding energy and that the structure can be controlled. Inspired by these results, we have mixed TiNT and g-C_3N_4 and heated them together to allow TiNT to decompose to anatase TiO_2, which can then self-catalyse the attachment of g-C_3N_4 rather than decompose, thus making a more efficient catalyst for methylene blue degradation.

5.3.4 Methylene Blue Standard Curve

The degradant was 10 mg/L methylene blue solution diluted from the concentrated solution. A methylene blue standard curve was firstly plotted by measuring the UV absorbance of methylene blue solutions with weight concentrations ranging from 1 mg/L to 10 mg/L. The maximum absorbance peak of methylene blue was found at 665 nm, so the absorbance at 665 nm of samples was picked to give a standard curve. The linear fitting of data was based on the Beer-Lambert equation, which is $A=\varepsilon lc$, where A is the absorbance, ε is the molar attenuation coefficient, l is the optical path length, and c is the concentration of the sample. In principle, within a certain range, the data points should drop in one line that passes through the origin point. Thus the intercept of linear fitting was set as zero. The fitting result was Absorbance=0.21267*weight concentration, and R^2 is 0.99895, as Figure 50 shows. In degradation experiments, UV-Vis absorbance of samples was measured, and the actual concentrations of solution in experiments were calculated by this standard curve.

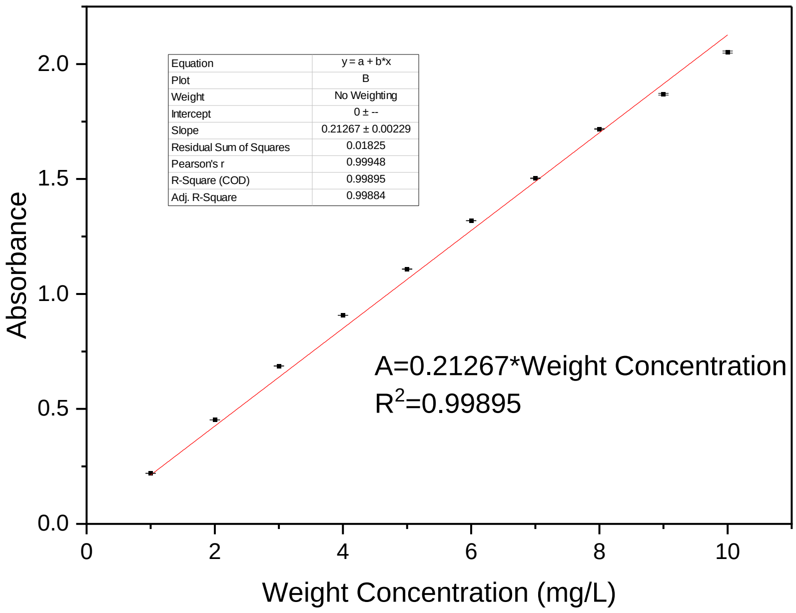

Figure 50 Methylene blue standard curve. Absorbance=0.21267*weight concentration and R^2 is 0.99895. This equation was used to calculate the weight concentration of samples.

5.3.5 Methylene Blue Degradation Pathway

The degradation pathway of Methylene Blue was discussed and proposed in literature mainly based on LC-MS and GC-MS analysis.[28, 144, 145] In this project, the Methylene Blue degradation pathway was investigated by GC-MS analysis of the product of photodegradation after being concentrated. Many compounds were detected, and the pathway was proposed in Figure 51. It was reported that the methylene blue could be oxidized[144], and here the same m/z value was detected for our sample. It was proposed that the N-C bond and S-C bond in the middle of methylene blue were broken at the early stage.[28] Here, we proposed two possible routes where the positions of breaking bonds were different. -N-$(CH_3)_2$ was proposed to be degraded into $-NH_2$ in the next stage. Finally, the compounds degraded into CO_2 and H_2O as well as possible mineralized products like NH_4^+ and NO_3^-.

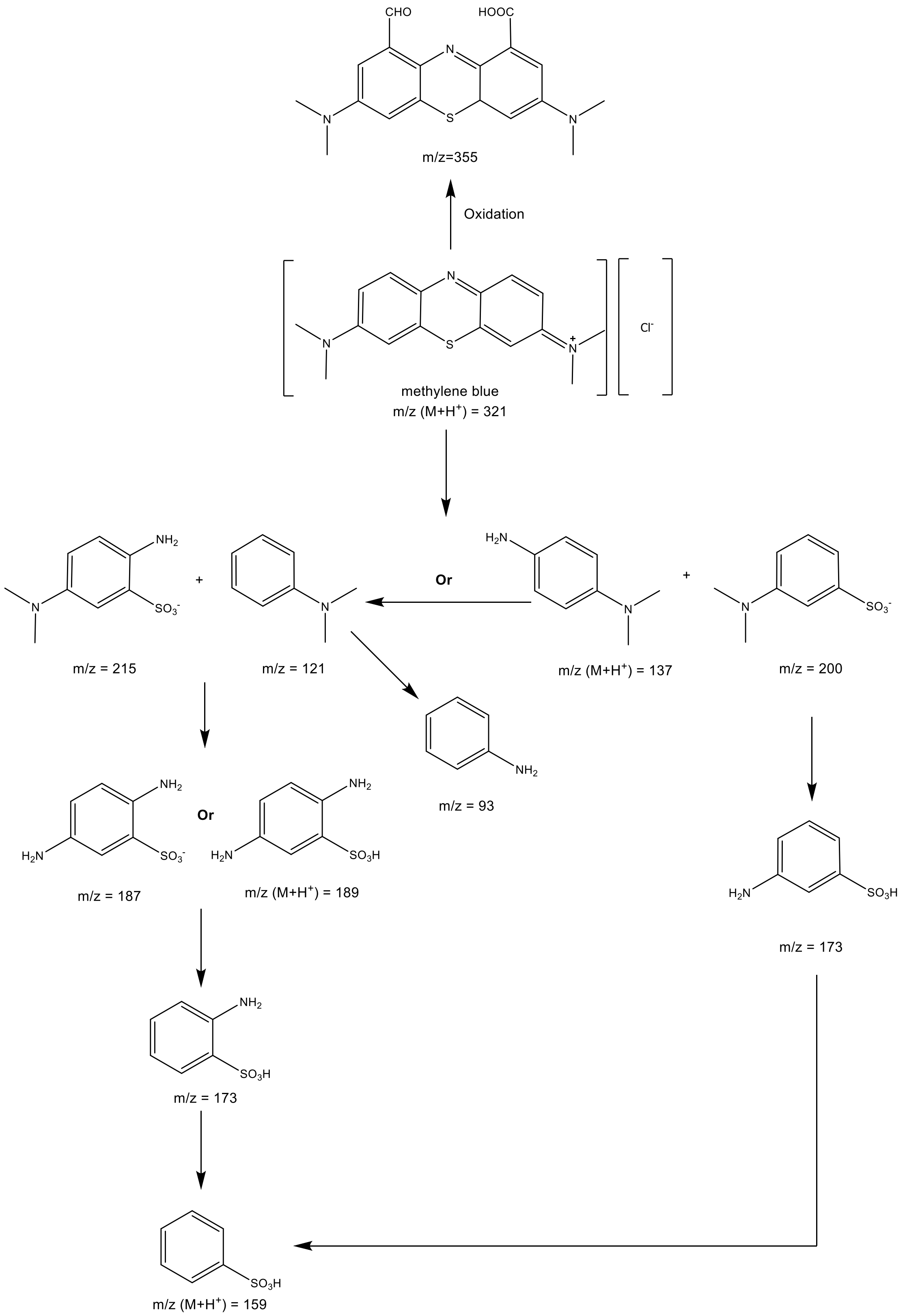

Figure 51 Proposed degradation pathway of Methylene Blue. The intermediates were determined by GC-MS.

5.3.6 Methylene Blue Self-Degradation and Degradation Catalysed by TiNT and g-C_3N_4

In a typical methylene blue degradation experiment, the mixture of MB solution and photocatalysts were stirred in darkness for 2 hours for adsorption before degradation, and the initial concentration after adsorption has determined the degradation rate. Each set of sample data is shown in two figures with emphases on adsorption and degradation.

MB self-degradation (baseline), as well as the photodegradation catalysed by TiNT and g-C_3N_4, are shown in Figure 52. Figure 52 (a) focused on the changes in weight concentration (WC) to show the adsorption ability of samples. WC was calculated from the absorbances of samples via the standard curve discussed above versus time. '-2' in the x-axis means the WC of starting MB solution, '0' stands for the MB adsorbed by catalysis within two hours. TiNT adsorbed 0.4 mg of MB within two hours, which was 12 times that g-C_3N_4. The kinetic adsorption reached equilibrium, so after switching on the light source, the concentration of MB decreased mainly because of photodegradation. WC of MB did not change so no self-degradation occurred in darkness. g-C_3N_4 has shown poor adsorption, which was caused by its small surface area (~10 m^2g^{-1} for bulk g-C_3N_4)[146].

Figure 52 (b) focuses on the degraded ratio of MB (weight concentration divided by the initial weight concentration). 41% of MB has self-degraded after 5 hours of illumination. g-C_3N_4 has shown a rapid degradation rate in the first hour, but later the degradation was slow. This was explained by the poor adsorption. Photodegradation is a process occurred on the catalysis surface, so the methylene blue molecules need to be adsorbed on the surface before being photodegraded by photocatalysis. In the fifth hour, the degradation rate of MB by g-C_3N_4 was even lower than the MB self-degradation rate. This was explained by a phenomenon observed that the fine g-C_3N_4 powder was stuck on the beaker wall, thus weakening the light intensity illuminated on the whole system. TiNT has shown better degradation than g-C_3N_4, which degraded 71% of MB in five hours.

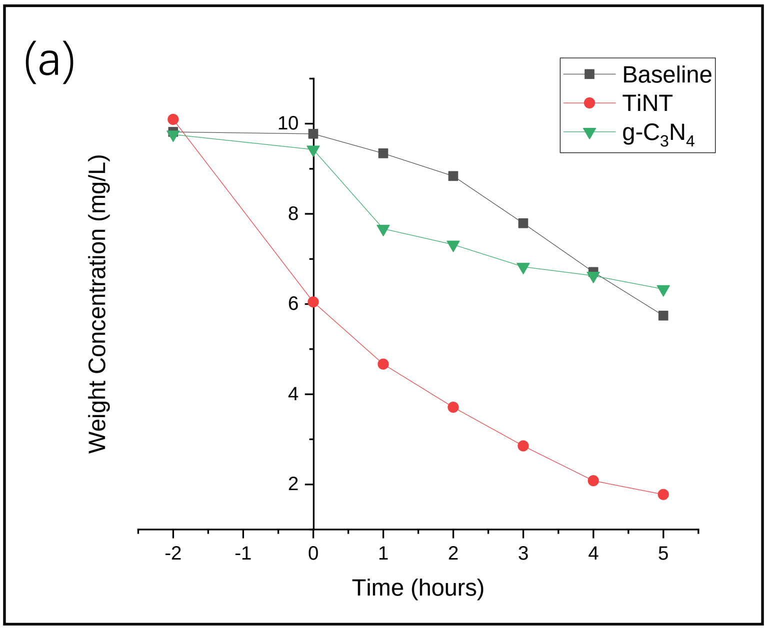

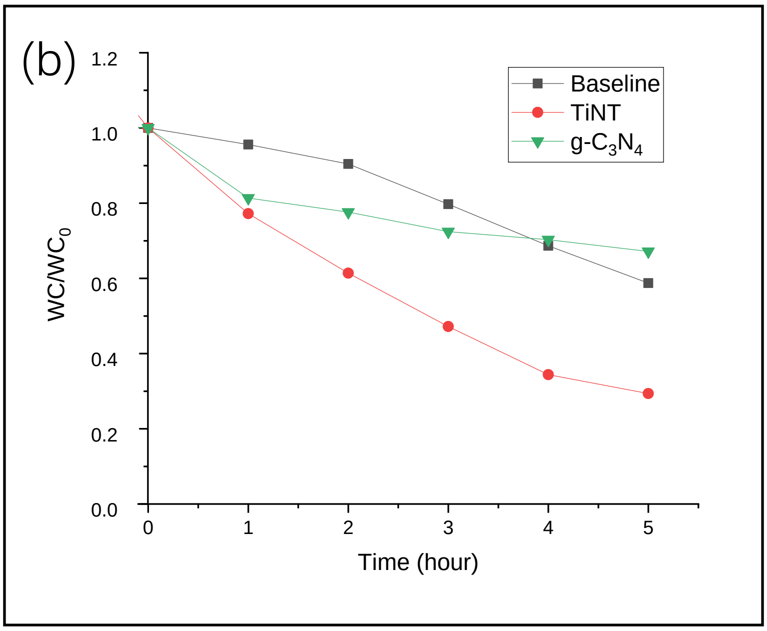

Figure 52 Baseline, TiNT and g-C_3N_4: (a) Weight concentration changed versus time; (b) Weight concentration ratio changed versus time. TiNT adsorbed 0.4 mg of MB within two hours which was 12 times than g-C_3N_4. 41% of MB has self-degraded after 5 hours of illumination. g-C_3N_4 has shown a rapid degradation rate in the first hour, but later the degradation was slow. TiNT has shown better degradation than g-C_3N_4, which degraded 71% of MB in five hours.

5.3.7 Methylene Blue Degradation Catalysed by TiNT-C_3N_4 and TiNT-dopamine-C_3N_4 Composites

MB degradation results of three samples that have different heating temperature/mixture ratios are shown in Figure 53 (a) and (b). The C_3N_4:TiNT 3:1 sample has shown the worst adsorption property and catalysis property among the three samples, and the reason was considered to be too much C_3N_4 in the system, which was not showing good activity. Compared to this high C_3N_4 content sample, the C_3N_4:TiNT 1:2 samples have shown promising photodegradation activity. C_3N_4-TiNT-1:2-400^{o}C has adsorption of 0.31 mg, which was smaller than that of TiNT (0.4 mg) and the similar sample heated under 300^{o}C (0.55 mg). However, even adsorbed less MB, it has the highest degradation activity. This sample degraded 78% of methylene blue in the first hour and 91% within two hours. After that, the rate was slowed down by the low concentration of MB that existed in the system. The reason was speculated that the carbon nitride and TiO_2 decomposed from TiNT could catalyse together to give better photoactivity than each of them, and this makes the heated samples interesting.

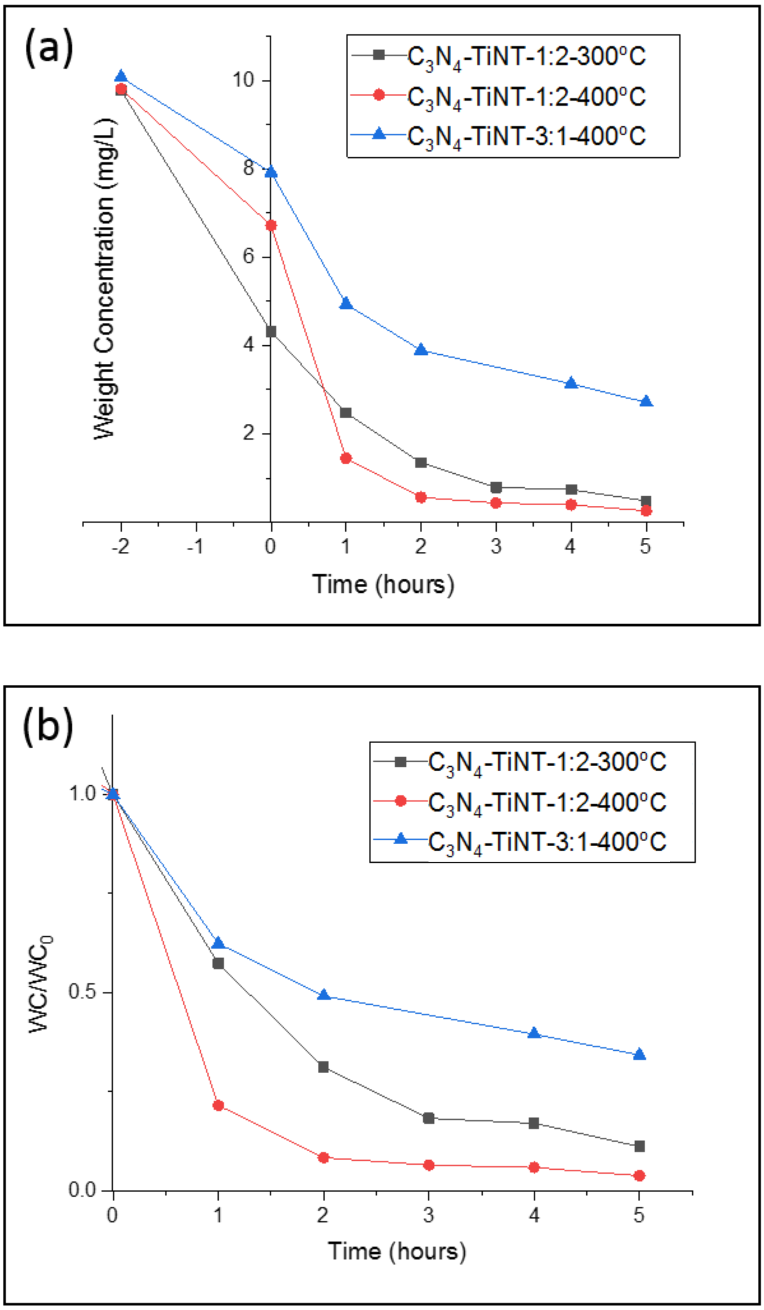

Figure 53 Methylene blue degradation catalysed by annealed C_3N_4-TiNT 1:2 and 3:1 composites: (a) Weight concentration changed versus time; (b) Weight concentration ratio changed versus time. The C_3N_4-TiNT-1:2 composite annealed at 300 °C shows the highest absorption ability, while the C_3N_4-TiNT-1:2 composite annealed at 400 °C shows the highest degradation ability. The C_3N_4-TiNT-3:1 sample shows poor absorption and degradation ability due to the high content of C_3N_4.

Since the above samples with higher TiNT ratio have performed well, C_3N_4-TiNT composites with mass ratios of 1:3 were synthesized and compared, and the degradation results are shown in Figure 54. The 1:3 sample annealed under 300°C has shown high adsorption of 0.55mg, which was the same as that of the 1:2 sample, and slightly higher degradation activity (46% removal rate in the first hour). The adsorption ability of the 1:3 sample annealed under 400 °C was very low, which was only 0.11 mg. However, this sample had a 71% removal rate in the first hour under light illumination and 88.5% within two hours. This result has indicated that all 1:2 and 1:3 ratio annealed C_3N_4-TiNT composites samples showed high photodegradation activity under full-range light when the samples annealed under 300 °C had higher adsorption ability when the samples annealed under 400 °C had higher photodegradation activity.

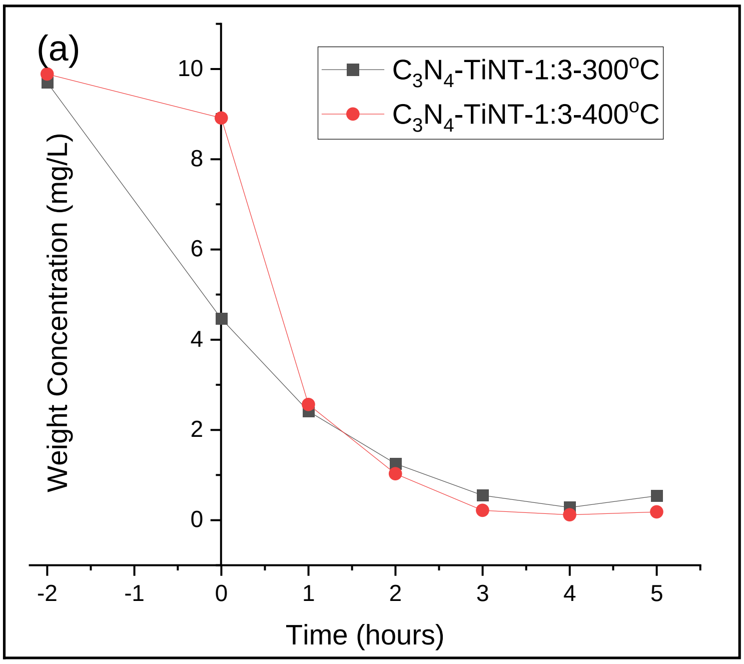

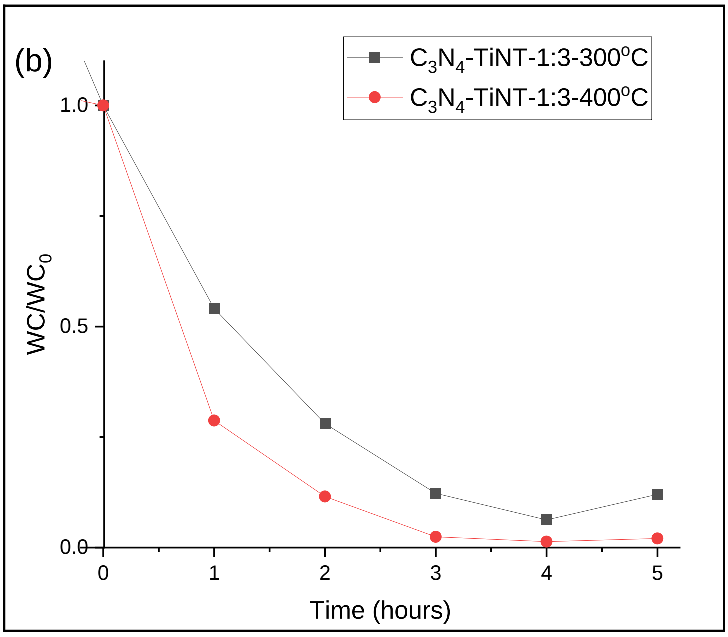

Figure 54 Methylene blue degradation catalysed by annealed C_3N_4-TiNT 1:3 composites: (a) Weight concentration changed versus time; (b) Weight concentration ratio changed versus time. The sample annealed at 300 °C shows high adsorption ability and removed 46% of methylene blue in the first hour. The sample annealed at 400 °C shows a very low adsorption ability (0.11 mg). However, this sample had a 71% removal rate in the first hour under light illumination and 88.5% within two hours.

TiNT modified by dopamine has shown improvement in visible light absorbance from the UV-Vis spectrum shown in the previous section (Figure 32). The methylene blue degradation catalysed by TiNT-dopamine and two composites are shown in Figure 55. TiNT-dopamine and C_3N_4-TiNT-dop-1:2 annealed under 300 ^oC have shown similar adsorption and photocatalytic ability to the composite without dopamine. The composite annealed under 400 ^oC shows poorer adsorption than C_3N_4-TiNT-1:2-400^oC, but no obvious difference in degradation rate.

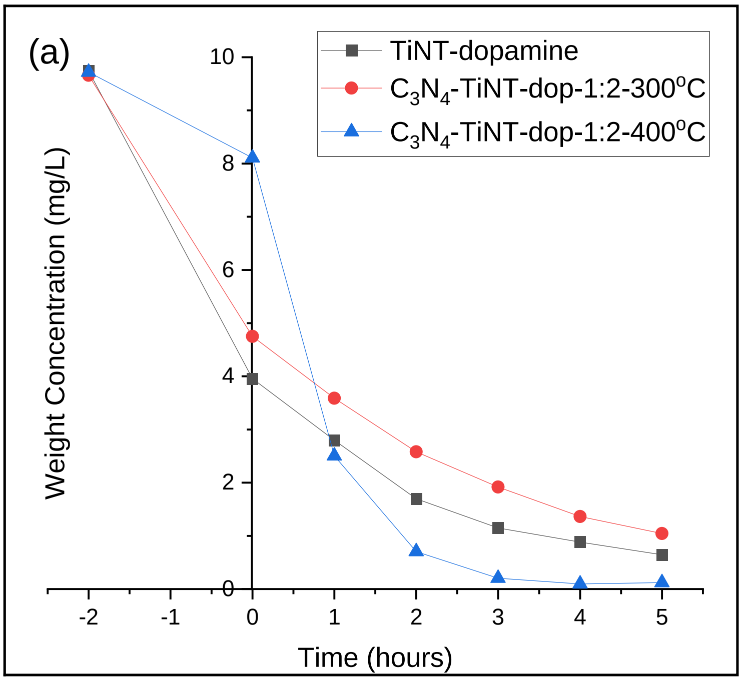

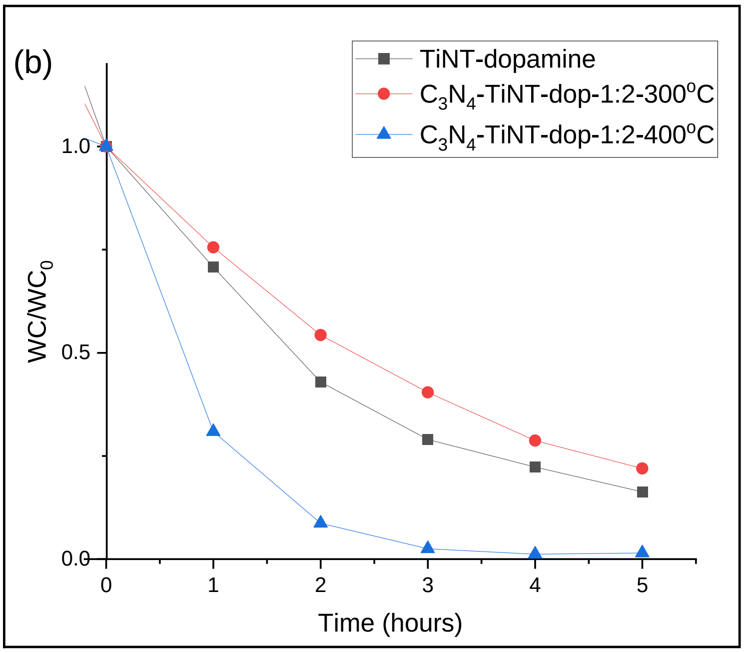

Figure 55 Methylene blue degradation catalysed by C_3N_4-TiNT-dopamine 1:3 composites: (a) Weight concentration changed versus time; (b) Weight concentration ratio changed versus time. TiNT-dopamine and C_3N_4-TiNT-dop-1:2 annealed under 300 °C have shown similar adsorption and photocatalytic ability to the composite without dopamine. The composite annealed under 400 °C shows poorer adsorption than C_3N_4-TiNT-1:2-400°C, but no obvious difference in degradation rate.

5.3.8 Methylene Blue Degradation Catalysed Under Visible Light

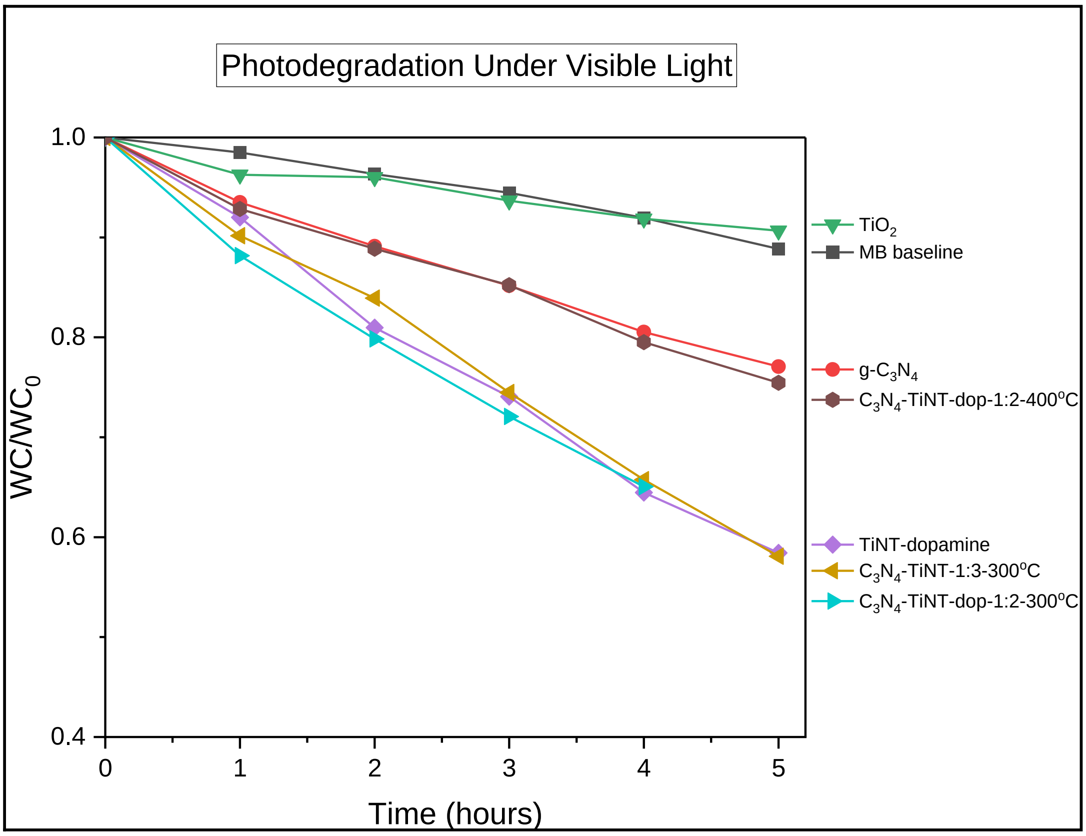

Figure 56 Photodegradation of methylene blue under visible light

Figure 56 shows the photodegradation of methylene blue under visible light catalysed by several samples. TiO_2 showed the same level of degradation ability as methylene blue self-degradation (baseline). TiO_2 has a band gap of 3.2 eV, which corresponded to 388 nm. Since the light filter applied for this light source was 400 nm, all UV light was filtered off. The visible light did not have enough energy to active TiO_2, and thus TiO_2 did not show photodegradation activity. g-

C_3N_4 has a band gap of 2.76 eV, which corresponds to 449 nm, and it means g-C_3N_4 can be activated by visible light. It removed 23% of methylene blue in five hours. C_3N_4-TiNT-dop-1:2-400^oC showed visible light absorbance from UV-Vis (shown in Figure 32). However, the degradation activity under visible light was at the same level as g-C_3N_4. This was explained by the formation of anatase under 400 ^oC, which showed poor activity and possibly reduced the interaction between the two components. TiNT-dopamine, C_3N_4-TiNT-1:3-300 ^oC and C_3N_4-TiNT-dop-1:2-300 ^oC showed similar degradation activity under visible light. The composites did not show improved activity compared with TiNT-dopamine though the composites had high activity under full-range light. It was proposed that the band gaps of composites were not small enough to show high activity under visible light.

5.4 Conclusion

In this chapter, g-C_3N_4 and synthesized by heating urea under 550 ^oC, and the C_3N_4-TiNT and C_3N_4-TiNT-dopamine nanocomposites were synthesized by electrostatic adherence. Different ratios of C_3N_4:TiNT composites were prepared and heated under 300/400 ^oC. g-C_3N_4 was protonated for better mixing with TiNT, which's surface was negatively charged. However, from the characterization results, no effect by protonation was observed. From the UV-Vis of C_3N_4-TiNT samples, a similar profile was found: from 250-350 nm, the

TiNT profile dominated the absorbance, and within visible light range, all three samples have shown absorbance before 443nm. This wavelength corresponded to a band gap of 2.8 eV and was dominated by C_3N_4. FTIR showed the characterization peak of C_3N_4, which was 810 cm^{-1} for all samples. XPS showed that the binding energy of Ti, C, and N had no obvious changes upon heating and modification and indicated the loss of H-O-Ti from the binding energy changes of oxygen. Band position of C_3N_4-TiNT composite was proposed based on XPS-VB and UV-Vis results. The morphology of the composite is shown by TEM. From XRD, it was found TiNT could transform to anatase under high temperature. The photodegradation pathway of methylene blue was proposed based on GC-MS. The photodegradation ability of samples was measured by degrading methylene blue, which was used as a probe molecule. It was found that for the samples heated under 400 ^oC, it showed high activity and low adsorption ability, which was caused by a high content of anatase in the samples. For the samples heated under 300 ^oC, the photoactivity was lower than previous samples but still high compared to the unmodified samples. Moreover, they showed high adsorption ability.

Chapter 6: AuNP-Organic-TiNT Composites and Organic Synthesis

6.1 Preface

In this chapter, due to the binding models of catechol structures on TiNT proposed above, organic compounds with catechol structures were specifically looked for. On the other side, due to the easy binding of thiol on gold nanoparticles (AuNPs), organic compounds with free thiol endings were desired. The scheme of desired nanocomposite structure is shown in Figure 4. The organic compounds were expected to bind to the TiNT surface via catechol structure and bind to gold nanoparticles via free thiol to achieve TiNT-Organic-AuNPs nanocomposites.

Typically, the synthesis of AuNPs involves a reductant for reducing Au^{3+} in $HAuCl_4$ and a stabilizer to exchange the chloride and hydroxyl ligands in $HAuCl_4$ aqueous solution with longer ligands. There are many methods for synthesizing AuNPs, and the sizes and surface properties are highly related to the adding amount of reducing agents and stabilizers/ligands. In this chapter, several typical literature methods were tried, and one of the methods was chosen for preparing TiNT-organic-AuNPs nanocomposites.

For the organic linker, no commercial compounds that contain both catechol and thiol were found. Thus, the organic compounds were synthesized from commercial catechol compounds, and the thiol groups were introduced. The structure of three organic linkers in Au-Organic-TiNT nanocomposites F2029, F2037, and F2050, are shown in Figure 57.

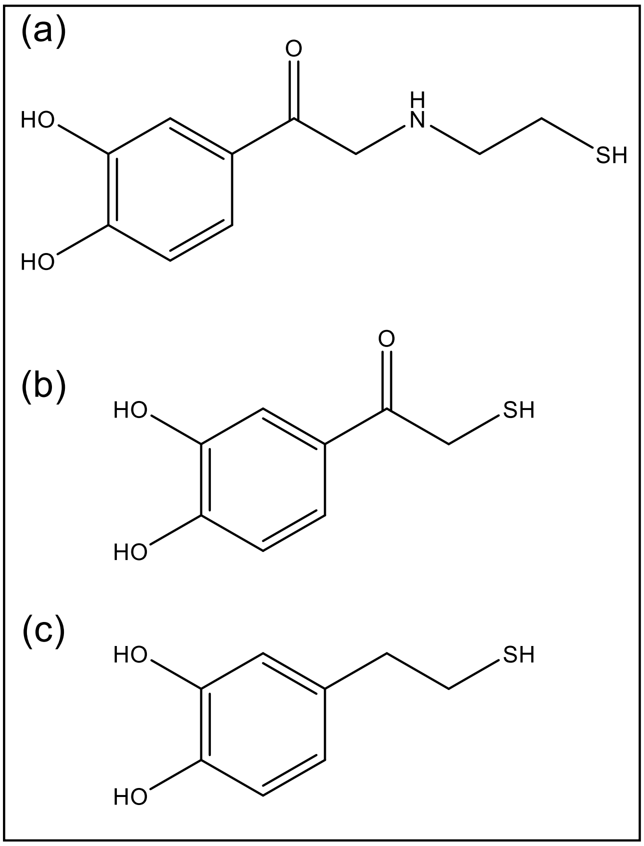

Figure 57 Organic linkers in Au-Organic-TiNT nanocomposites (a) F2029; (b)F2037; (c)F2050. They all have catechol structures and a free thiol group as an ending group.

6.2 Experimental Section

Materials

PPh_3 and $HAuCl_4 \cdot xH_2O$ (~50% Au basis) were purchased from Sigma-Aldrich. TOAB and DMF were purchased from J&K. Toluene, $NaBH_4$, DCM, PE, MeOH, Na_2CO_3, MeCN and EtOAc were purchased from Sinopharm. 1-dodecanethiol and potassium thioacetate were purchased from Aladdin. 4-(Chloroacetyl)catechol, Cysteamine, Et_3SiH and TFA were purchased from TCI. $CDCl_3$ was purchased from CIL. D_2O, DMSO-d_6, $MgSO_4$ and methanol-d_4 were purchased from Adamas. TLC Silica gel 60 F_{254} were purchased from Merck, and NMR sample tubes were purchased from Wilmad-LabGlass. Other materials used in this chapter were the same as previous chapters.

6.2.1 Gold Nanoparticles Synthesis

PPh_3 method

The synthesis of gold nanoparticles by the PPh_3 method was based on a literature process.[147] 0.2 g of $HAuCl_4 \cdot xH_2O$, 0.28 g of TOAB, 12 mL of water, 12 mL of toluene and a stirrer bar were added into a 250 mL round bottom flask. The mixture was stirred for 5 minutes, then 0.575 g of PPh_3 was added. The organic phase turned white. The mixture was left to stir for 10 minutes. Next, 0.4 g of $NaBH_4$ dissolved in 2 mL of water was added rapidly. The organic layer turned to brown quickly, and bubbles formed. The mixture was left to stir overnight under the protection of Argon and at room temperature. Then the mixture was transferred into a separation funnel with a small amount of toluene, and the organic layer was washed with water and brine. The organic layer was separated and evaporated to give crude. The crude was dissolved with minimum pre-heated DCM, and about 100 mL of PE was added to recrystallize the product. Then solid was filtered off and washed with 2*35 mL of PE then 2*35 mL of 2:3 MeOH: H_2O), 2*(20 mL of PE then 20 mL of 1:1 MeOH: H_2O), and finally with 20 mL of PE to form product 0.1 g.

Brust Method

The synthesis was based on a literature process that was reported by Brust in 1994[148]. This method uses $NaBH_4$ as a reductant and 1-dodecanethiol as ligands. Experimentally, 30 mL of $HAuCl_4$ solution (30 mmol/L) was firstly filtered by a 2.2 µm membrane. TOAB solution was prepared by dissolving 2.20g of TOAB into 81 mL of toluene, and the solution was mixed with $HAuCl_4$ solution. Colour changes were observed from gold to light brown for the aqueous layer and from colourless to dark red for the organic layer. After vigorously stirring, the aqueous layer became colourless, then 0.184 g of 1-dodecanethiol was added to the topper layer. 25 mL of fresh prepared $NaBH_4$ solution (0.4 mol/L) was added dropwise. The mixture was stirred for 3 hours, and then the organic layer was separated and concentrated to about 10 mL. Next, 400 mL of ethanol was added, and the mixture was kept under -26 ^oC

overnight. The black precipitate was filtered off and washed with 200 mL ethanol. The resultant crude was dispersed in about 12 mL of toluene and mixed with 400 mL of ethanol. The mixture was kept under -26°C for 4 hours, then the precipitate was filtered off and washed with 200 mL of ethanol. Finally, the black solid was dried in the air and 0.15 g of product was prepared.

Martin Method

Gold nanoparticles were synthesized based on the literature method.[149] Firstly, 10 mL of $HAuCl_4$/HCl stock solution (50 mM) was prepared by adding 0.43 g of $HAuCl_4•xH_2O$, 42 μL of HCl solution (36-38%) and ultrapure water into a 10 mL volumetric flask. Then, 15 mL of NaOH/$NaBH_4$ stock solution (50 mM) was prepared by mixing 0.034 g of NaOH, 0.033 g of $NaBH_4$ and 15 mL of ultrapure water. Fresh NaOH/$NaBH_4$ stock solution was used in the experiments. The synthesis was carried out by following procedures: to a 100 mL round bottom flask, under stirring, 48 mL of ultrapure water, 0.5 mL of $HAuCl_4$/HCl stock solution, and 1.5 mL of NaOH/$NaBH_4$ stock solution were added in order. As soon as the NaOH/$NaBH_4$ stock solution was added, bubbles formed, and the colour of the mixture changed from yellow to brown and later became 'wine red'. Another ratio of $HAuCl_4$/HCl stock solution to NaOH/$NaBH_4$ stock solution was tried, including 1:5 and 1:10, but the resulting mixture was not homogeneous.

6.2.2 Organic Synthesis

Experiment F2022: Synthesis of 1-(3,4-dihydroxyphenyl)-2-((2-mercaptoethyl)amino)ethan-1-one

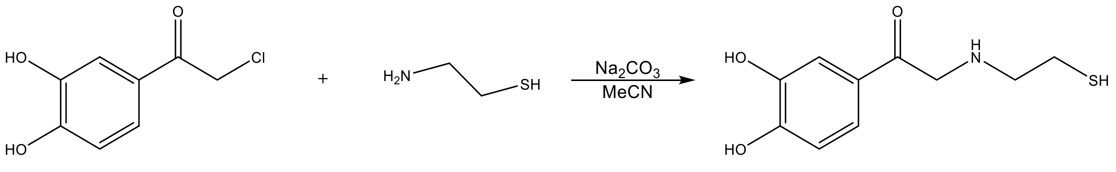

F2022

In a 250 mL round bottom flask, 1.866 g of 4-(Chloroacetyl)catechol (10 mmol), 0.772 g of cysteamine (10 mmol), 1.59 g of Na_2CO_3 (15 mmol), 100 mL of MeCN and a stirrer bar were added in. The mixture was stirred at room temperature and under Ar protection overnight. Then the solvent was evaporated, then the residue was diluted with EtOAc. TLC did not show any new spot and indicated that the reaction did not occur.

Experiment F2023: Synthesis of 1-(3,4-dihydroxyphenyl)-2-((2-mercaptoethyl)amino)ethan-1-one

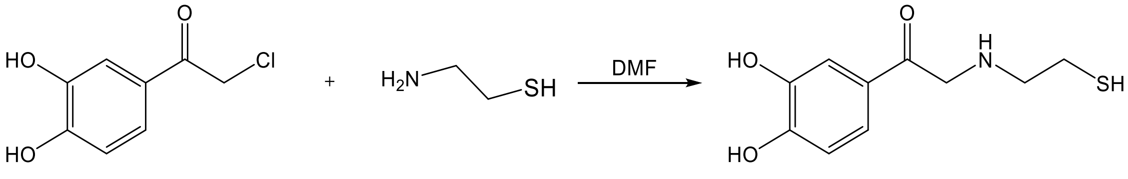

F2023

In a 250 mL round bottom flask, 1.867 g of 4-(Chloroacetyl)catechol (10 mmol), 0.773 g of cysteamine (10 mmol), 70 mL of dry DMF, and a stirrer bar were added. The mixture was stirred at room temperature and Ar protection overnight. TLC (EtOAc: PE=3:2) of the reaction mixture showed new spots and indicated that the reaction occurred. Then DMF was evaporated, and crude was dissolved in H_2O (~100 mL), washed with EtOAc (50 mL x 3). The aqueous phase was separated and finally evaporated and dried with EtOH. 2.4 g of red solid was prepared. Yield: 105.6% because the product was not completely dried. ^1H NMR (400 MHz, D_2O): δppm 7.51-7.54 (dd, 1H, Ar-H), 7.47 (d, 1H, Ar-H), 6.95-6.97 (d, 1H, Ar-H), 4.04 (s, 2H, CH_2), 3.17-3.20 (t, 2H, CH_2), 2.84-2.87 (t, 2H, CH_2). ^{13}C NMR (100 MHz, DMSO-d_6): δppm 193.29 (CH_2COAr), 150.99 (C-4), 145.14 (C-3), 126.84 (C-1), 121.92 (C-6), 115.27 (C-2), 114.94 (C-5), 37.85 ($COCH_2NH$), 36.68 ($NHCH_2CH_2$), 28.46 (CH_3SH). ($M+H^+$) m/z: 228.071.

Experiment F2031: Synthesis of S-(2-(3,4-dihydroxyphenyl)-2-oxoethyl) ethanethiol

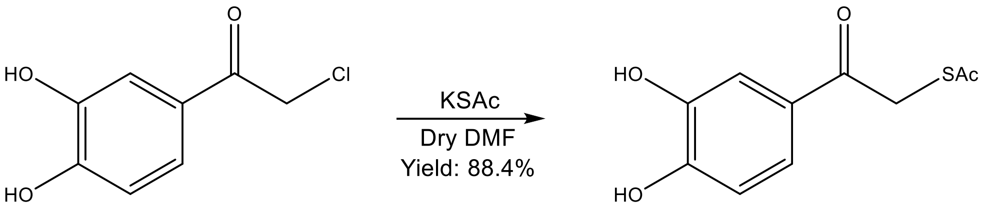

F2031

In a 100 mL round bottom flask, 1.87 g of 4-(Chloroacetyl)catechol (10 mmol), 1.37 g of potassium thioacetate (12 mmol), 50 mL of dry DMF and a stirrer bar were added. The mixture was stirred at room temperature overnight. The solid was filtered off, and the filtrate was rotatory evaporated at 90 °C. The residue was diluted with H_2O and EtOAc and transferred into a separation funnel. Then the aqueous phase was washed with EtOAc 3*50 mL. Next, all organic phases were combined, washed with water and brine, dried over $MgSO_4$, and finally concentrated to give 2.66 g of crude. The crude was further purified by flash chromatography (EtOAc: PE=1:1) to give 2 g of the final product F2031. Yield: 88.4%. ^1H NMR (400 MHz, Methanol-d4): δppm 7.49-7.52 (dd, 1H, Ar-H), 7.45 (d, 1H, Ar-H), 6.85-6.87 (d, 1H, Ar-H), 4.39 (s, 2H, CH_2), 3.39 (s, 3H, CH_3). ^{13}C NMR (100 MHz, Methanol-d_4): δppm 194.55 ($SCOCH_3$), 192.60 (CH_2COAr), 151.39 (C-4), 145.22 (C-3), 127.75 (C-1, 122.16 (C-6), 114.78 (C-2), 114.49 (C-5), 35.50 (CH_2S), 28.60 (CH_3CO). (M+Na^+) m/z: 249.02.

Experiment F2035: Synthesis of 1-(3,4-dihydroxyphenyl)-2-mercaptoethan-1-one

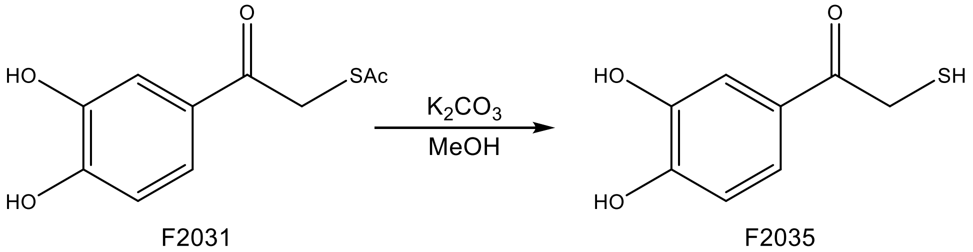

In a 100 mL round bottom flask were added 0.226 g of F2031 (1 mmol), 0.167 g of K_2CO_3 (1.2 mmol), 30 mL of MeOH and a stirrer bar. The mixture was heated at 60 °C for 1 hour. Then the reaction was quenched by 1 M HCl solution until pH<7. Next, the solvent was evaporated to form a crude. TLC and NMR of the crude showed the formation of the product. ^{1}H NMR (400 MHz, Methanol-d4): δppm 7.39 (d, 1H, Ar-H), 7.37-7.38 (d, 1H, Ar-H), 6.71-6.73 (d, 1H, Ar-H), 4.06-4.09 (s, 2H, CH_2).

Experiment F2040: Synthesis of 4-(2-chloroethyl)benzene-1,2-diol

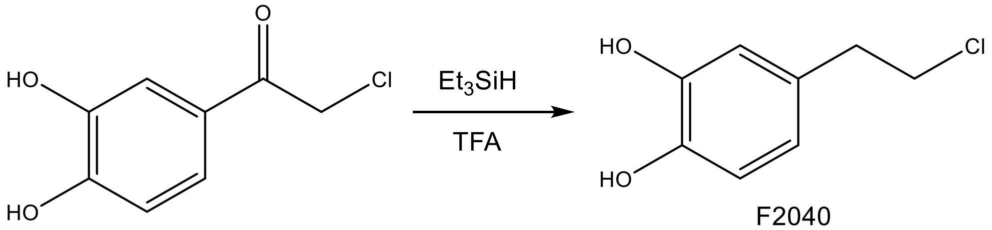

F2040

This reaction was operated based on literature procedures[150] with modifications. In a 250 mL round bottom flask, 9 g of 4-(Chloroacetyl)catechol (48 mmol) was dissolved in 60 mL of TFA. Next, 28 mL of Et_3SiH (180 mmol) were added dropwise. The mixture was stirred at room temperature overnight. Then the mixture was poured into ice water, extracted with 3*150 mL DCM, dried over $MgSO_4$ and given a pink crude. Next, the crude was further purified by flash chromatography (EtOAc: PE=1:3) to give 6.09 g of the product F2040. Yield: 73.5%. ^{1}H NMR (400 MHz, $CDCl_3$): δppm 6.80-6.82 (dd, 1H, Ar-H), 6.75 (d, 1H, Ar-H), 6.64-6.67 (m, 1H, Ar-H), 3.64-3.68 (t, 2H, CH_2), 2.93-2.97 (t, 2H, CH_2). ^{13}C NMR (100 MHz, $CDCl_3$): δppm 143.62 (C-3), 142.36 (C-4), 131.20 (C-1), 121.31 (C-6), 115.90 (C-2), 115.44 (C-5), 45.17 (CH_2Cl), 38.53 (CH_2Ar).

Experiment F2048: Synthesis of S-(3,4-dihydroxyphenethyl) ethanethioate

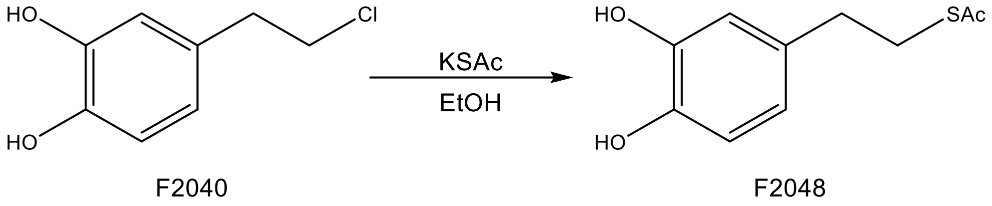

1.08 g of F2040 (6.26 mmol) was dissolved in 300 mL of EtOH in a 500 mL round bottom flask. 3.57 g of KSAc (31.3 mmol) was added to the solution. The mixture was heated at reflux for 5 hours, and the TLC showed no starting material left in the mixture. The mixture was filtered, and the filtrate was concentrated to give a yellow solid. The solid was dispersed in 200 mL of H_2O, then extracted with 4*70 mL of diethyl ether. The organic phases were combined, and the rotatory evaporated to give the product F2048. H NMR (400 MHz, $CDCl_3$): δppm 6.60-6.80 (m, 3H, Ar-H), 3.05 (t, 2H, CH_2), 2.73 (t, 2H, CH_2), 2.33 (s, 3H, CH_3). ^{13}C NMR (100 MHz, $CDCl_3$): δppm 196.45 ($SCOCH_3$), 143.65 (C-3), 142.25 (C-4), 132.89 (C-1), 121.08 (C-6), 115.90 (C-2), 115.38 (C-5), 35.11 (CH_2Ar), 30.71 (CH_2S), 30.67 (CH_3CO).

6.2.3 Au-Organic-TiNT Nanocomposites Synthesis

F2029 & F2030 Synthesis

From F2023, the thiol was firstly bound to the AuNPs prepared from the Martin method. The fresh prepared AuNPs mixture was 100 mL and contained 0.1

mmol of Au. 0.23 g of F2023 was added all at once, and the mixture was stirred at room temperature for 2 hours. The atomic ratio of Au:S was 1:10. 10 mL of the AuNP-F2023 mixture was diluted by 40 mL of water in a new 125 mL conical flask, and a stirrer bar that was washed by aqua regia was added. Under stirring, 0.23 g of TiNT was added. The weight percentage of F2023:TiNT was 10 wt.%. The mixture was ultrasonicated for 5 minutes and stirred at room temperature overnight under the protection of Ar. The precipitate was filtered off, washed with H_2O and finally dried in the air. The resultant solid was labelled as F2029. This synthesis was repeated with 100 wt.%. of F2023:TiNT. The resultant solid was labelled as F2030.

F2037 I and II Synthesis

These two compounds were synthesized by the reaction between TiNT, F2037 and AuNPs in a different order. Deprotection of F2031 was firstly carried out in MeOH under 60 °C. The end of the reaction was confirmed by TLC, then HCl was added to quench the reaction and form free thiol. Next, the mixture was separated into two flasks. In one flask, as F2037 I, the mixture was diluted by water and gold nanoparticles were synthesized by the reduction of $HAuCl_4$ using $NaBH_4$, under the existence of free thiol in the mixture. This process resultant in a dark purple mixed with black & brown solid on the flask wall. By further dilution and addition of $NaBH_4$, the colour of the mixture turned dark red, which indicated the formation of AuNPs. Finally, TiNT was added to isolate the composite. The catechol ending of AuNP-thiol could easily bind on the TiNT surface. Thus TiNT was able to capture soluble catechol compounds and isolate composite as solid phase. The resultant powder was filtered off and washed. However, during filtration, it was found the colour of the powder was not uniform. It was explained by a lack of purification. Thus, impurities were isolated with TiNT together. In addition to this, AuNPs prepared by $NaBH_4$ reduction was a colloid in water. Thus the purification of AuNPs was difficult. As a result, a mixture was gotten.

In another flask, as F2037II, the organic mixture was firstly diluted by water and mixed with TiNT. The colour of powder has changed from white to orange once mixing due to the binding of the catechol compound on the TiNT surface. Next, the solid was filtered off and washed to remove any soluble impurities, including unreacted organic compounds, MeOH, and other by-products. Then the solid was redispersed in water, and gold nanoparticles were synthesized by the reduction of $HAuCl_4$ using $NaBH_4$. During this process, orange dispersion turned to brown at the beginning caused by the reduction of $HAuCl_4$. Later the mixture turned to dark red, which indicated the formation of gold nanoparticles. After stirring overnight, the purple solid was finally filtered off and washed with water. Compared with the previous sample, F2037II contained fewer impurities due to two washing processes.

F2041B (TiNT-F2040) Synthesis

F2041B was synthesized by mixing 0.5 g of TiNT with 0.05 g of F2040 in 100 mL water. The mixture was stirred over the weekend. The solid was filtered off then washed with water and ethanol. The orange solid was further dried to give F2041B.

F2050 Synthesis

In a 100 mL round bottom flask, 0.3 g of KSAc was firstly mixed with 50 mL of EtOH, and the mixture was stirred for 5 minutes. Then 0.3 g of F2041B was added, and the mixture was stirred overnight. Next, the solid was filtered off and washed with water and ethanol. Then 0.2 g of produced solid was mixed with 20 mL of MeOH and 0.2 g of K_2CO_3 in a 50 mL round bottom flask. The mixture was heated under 60^oC with stirring under the protection of Ar for 240 minutes. Then the solid was filtered off and washed with water and methanol. Next, the solid was dispersed in 100 mL of water to form a slurry. 0.04 g of $HAuCl_4 \bullet 3H_2O$ was added. Then, fresh prepared $NaBH_4$ solution (0.1 M) was added in portions (0.2 mL * 5). The mixture was stirred at room temperature and Ar protection overnight. Finally, the purple solid was filtered off and washed with a small amount of water.

Organic compounds used for photodegradation

The organic compounds used for photodegradation were listed as follow:

F2023

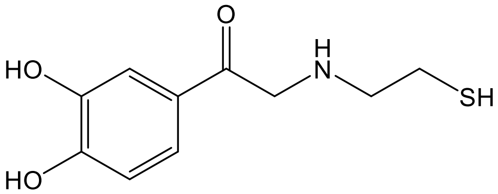

F2035

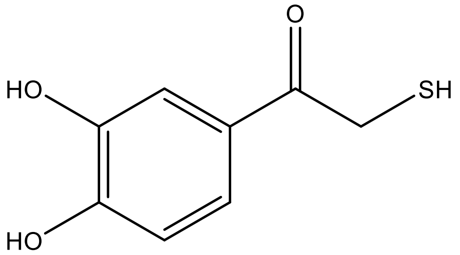

F2040

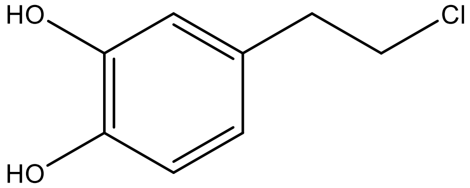

F2048 reacted with K_2CO_3

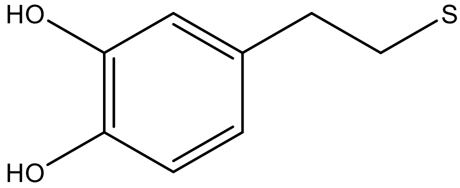

All of them have a catechol structure, a carbon chain, and a thiol group as an ending group. Their photodegradation abilities were tested and compared.

6.3 Results and Discussions

6.3.1 Gold Nanoparticles

AuNP was expected to show the LSPR effect to help harvest visible light, as well as bind to synthesized thiol compounds. The SPR peak of AuNPs on the UV-Vis spectrum is usually around 520 nm and is highly related to the sizes of AuNPs.[151]

AuNP-PPh_3 was produced by using $NaBH_4$ and PPh_3, which worked as a reducing agent and stabilizer ligand, respectively. The resultant AuNPs were black powder and could be easily redispersed in some organic solvents like toluene and DCM. It was reported that this kind of AuNP was able to undergo the ligand exchange process easily, and it was expected that PPh_3 ligands could be replaced by synthesized thiol compounds in this project, according to similar ligand exchange reactions in literature[152]. However, the UV-Vis spectrum of AuNP-PPh_3 shown in Figure 58 did not show an obvious absorbance peak at around 520 nm but a broad, low-intensity increase between 400 and 600 nm. This phenomenon was also reported by other researchers[152, 153]. It was explained by the quantum confinement effect, which limits the motion of randomly moving electrons when the size of particles is too small to be comparable to the wavelength of the electrons. In this synthesis, the average size of AuNP-PPh$_3$ was considered to be around 1.5 nm, according to a similar reaction in literature[153]. However, the SPR peak at ~520 nm played an important role in the scheme that it helped absorb visible light. As a result, other methods which were able to produce larger AuNPs were tried.

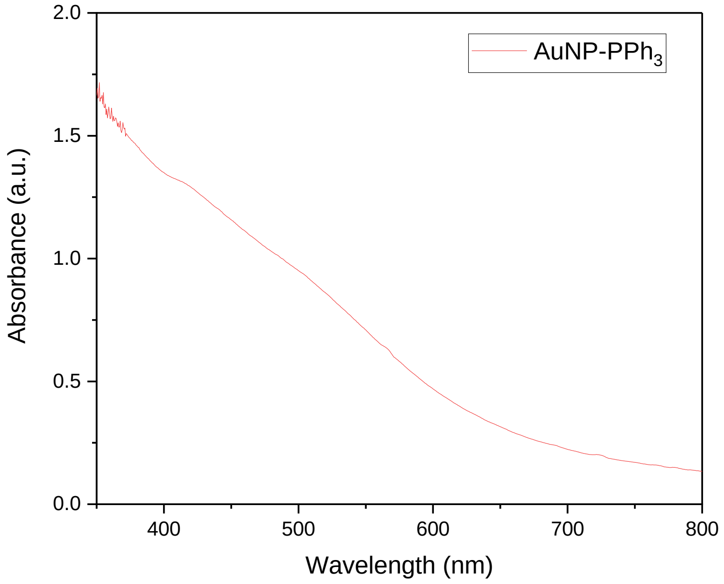

Figure 58 UV-Vis absorbance of AuNP-PPh$_3$. No obvious SPR peak was found.

For the gold nanoparticles synthesized by the Brust method[148], the UV-Vis absorbance is shown in Figure 59. An SPR peak at ~515 nm can be seen from the figure, which means the AuNPs were successfully formed. However, it was found that the resultant brown powder could not dissolve in water, and it was hard to be dispersed in water. This was explained by the stabilizer 1-dodecanethiol, which was a hydrophobic compound with a long carbon chain. Gold nanoparticles were expected to link to organic molecules with thiol group as ending group and work in an aqueous system; thus, hydrophobic AuNPs were not preferred, and other methods were tried.

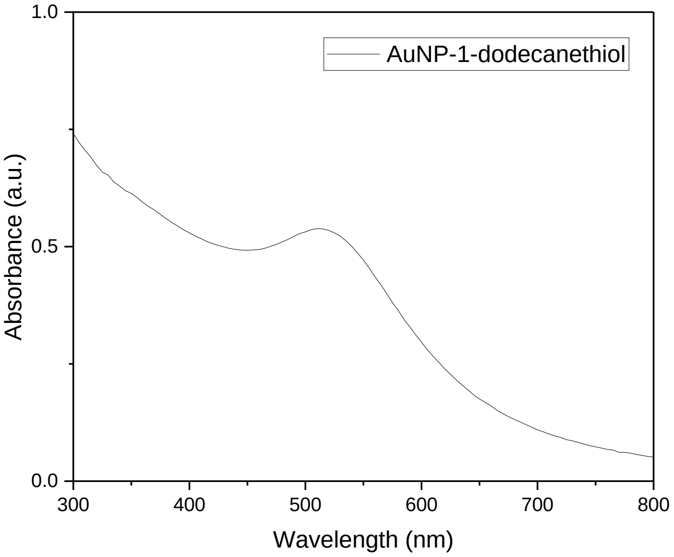

Figure 59 UV-Vis absorbance of AuNPs prepared by Burst method. An SPR peak at ~515 nm was found.

Martin method was tried for synthesizing gold nanoparticles.[149] The main reason for choosing this method was that the whole reaction occurred in an aqueous system. On the other side, no additional stabilizer in the solution means the gold nanoparticles could be easier to link to organic molecules with the thiol group. Usually, stabilizers like sodium citrate and 1-dodecanethiol are added to the gold colloids to avoid aggregation. However, without an additional stabilizer, the prepared gold nanoparticles had not shown obvious aggregation for approximately three months since synthesized. The UV-Vis absorbance of the prepared gold nanoparticles colloids was measured and shown in Figure 60.

The spectrum shows an SPR peak at around 515 nm, which suggests the average diameter of gold nanoparticles is less than 10 nm[151].

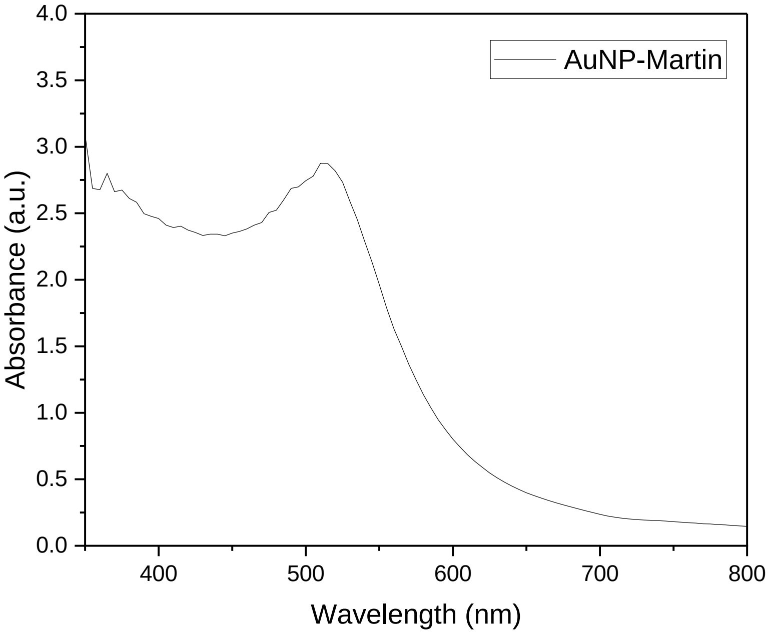

Figure 60 UV-Vis absorbance of AuNPs prepared by Martin method. An SPR peak at ~515 nm was found.

6.3.2 Discussion of Organic Reactions

F2023

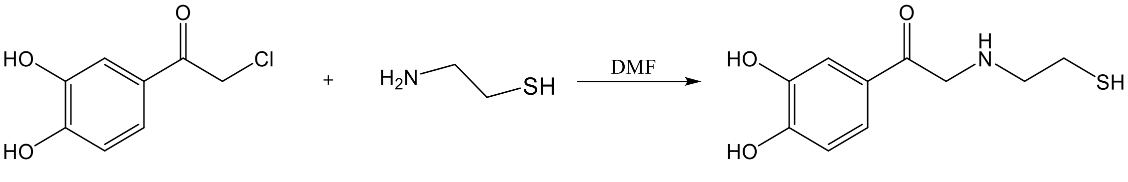

F2023

The starting material, 2-chloro-1-(3,4-dihydroxyphenyl)ethan-1-one, is commercial and has a catechol structure and a chloride. By the leave of chloride, the molecule can react with another nucleophile like cysteamine. It was an SN_2 reaction, and HCl was produced. The synthesis was firstly carried out in MeCN under the presence of Na_2CO_3 (Experiment F2022), which was used as a base to neutralize HCl to promote the reaction. However, this reaction did not work. The reason was that the solubility of Na_2CO_3 in acetonitrile was too poor to react with H^+ in the reaction system, and the water in undried MeCN reduced the reactivity of amine groups. Then the synthesis (Experiment F2023) was carried out in dry DMF without adding a base. This reaction successfully produced the product. The reason was explained by the interaction between DMF and HCl[154], which reduced the amount and reactivity of H^+ in the reaction mixture, thus promoting the reaction.

Cysteamine has an amine group and thiol group, which are both nucleophiles and possible to substitute the chloride group in the starting material. This resulted in a question of the priority of reaction. The difference between the two possible products could not be distinguished by mass spectrum or ^1H NMR because they have the same molecular formula, and the environment of hydrogens on these two compounds was very close. The priority was identified by a stain called ninhydrin. Ninhydrin is a chemical used to detect amines. For the cysteamine on the TLC plate, ninhydrin made it show a purple colour in a short time. However, when the product was contacted with ninhydrin, no purple colour was observed. This was considered to be a piece of circumstantial evidence that the amine group attacked as a nucleophile, and the ending group was free thiol. This product was labelled as F2023 and used in the further reaction with TiNT and AuNPs.

F2035

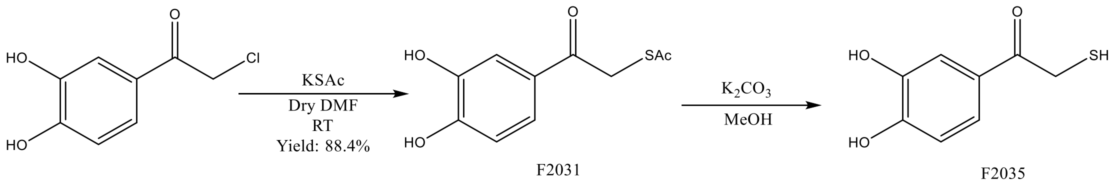

Potassium thioacetate is a commercial compound that can introduce thioacetate by substitution in organic reactions. By substitution of chloride, F2031 was produced with a yield of 88.4%. The reaction was also carried out in dry MeCN, which gave a yield of 85.4%. As a protection group, the acetyl group can be removed by both acid and base. The deprotection of the thiol group was carried out in MeOH by potassium carbonate. For the first time, the reaction was carried out at room temperature and stirred overnight. The TLC showed reaction occurred. However, it was found the colour of the product changed after storing overnight because the product contains free thiol and it had high activity. The reaction was repeated at 60 ^{o}C, and the reaction time was shortened to 1 hour to reduce the effect of unstable thiol. For the first time, the reaction was carried out at room temperature and stirred overnight. The TLC showed reaction occurred. However, it was found the colour of the product changed after storing overnight because the product contains free thiol and it had high activity. The reaction was repeated at 60 °C, and the reaction time was shortened to 1 hour to reduce the effect of unstable thiol. After purification by flash chromatography (EtOAc: Petroleum Ether 3:1 v:v), the product was collected and confirmed by NMR. However, it was found the product was still unstable, even stored under the protection of Ar. To solve this problem, the further synthesis of AuNP-F2035-TiNT composite was operated as a one-pot reaction together with deprotection of thiol on F2031.

F2040

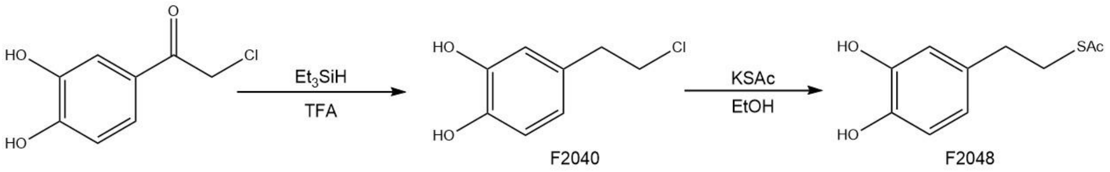

F2040 was synthesized based on a literature reaction[150]. The reaction was a reduction of the carbonyl group by triethylsilane under TFA. TFA worked as a Lewis acid and protonated the oxygen on the carbonyl group, then the minus hydrogen on triethylsilane attacked the carbon on the carbonyl group and reduced the carbonyl to a secondary alcohol. Next, the secondary alcohol was protonated and reduced by triethylsilane via a similar mechanism to give F2040. There are several other methods for reducing the carbonyl group, such as Clemmensen Reduction, which uses Zinc/Mercury[155]; Wolff-Kishner Reduction, which uses hydrazine[156]; $NaBH_4$/$LiAlH_4$ as reductant. The chloride group on

F2040 was substituted by potassium thioacetate in anhydrous ethanol to form F2048, and the reaction was further repeated on the TiNT surface. The mechanism of the reaction was an SN_2 reaction. F2040 showed good solubility in ethanol when the potassium chloride did not dissolve, and thus the reaction was moved forward. It was attempted to remove the thioacetate group for forming a free thiol. However, the product was quite unstable. Therefore, the further deprotection of thiol was operated in one pot followed by synthesizing the composite

6.3.3 Results and Discussion of AuNP-Organic-TiNT Composite

Characterization Results

F2029 & F2030

The main difference in the synthesis of these two samples was the addition amount of the F2023-AuNP mixture. F2029 contained less organic linker and gold compared to F2030. Figure 61 shows the UV-Vis absorbance of F2029 and F2030. Before 270 nm, both samples showed the same profile of TiNT. For F2029, the TiNT profile was found up to 350 nm. The increase of absorbance within 350-500 nm was attributed to the charge transfer complex formed between TiNT and the catechol linker F2023 when the broad peak at around

540 nm was dominated by the LSPR peak of AuNPs. F2030 showed a similar profile, but the overall intensity was much stronger due to the higher content of F2023 and AuNPs.

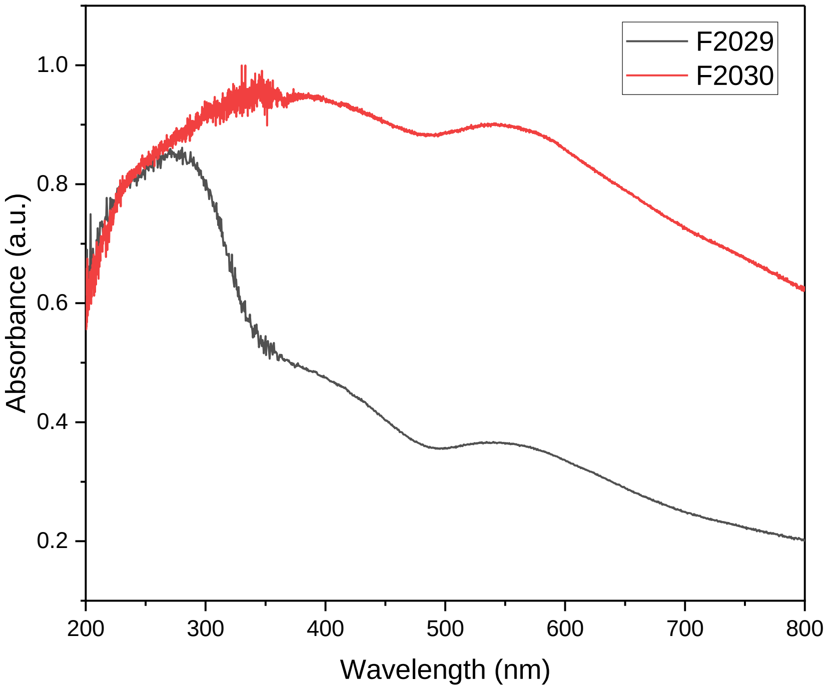

Figure 61 UV-Vis absorbance of F2029 and F2030. F2029 shows the TiNT profile, a charge transfer band, and SPR peak of AuNPs. F2030 shows a charge transfer band and similar SPR peak with higher overall intensities.

TEM and HRTEM images of F2029 and F2030 are shown in Figure 62. Figure 62 (a)&(b) shows the morphology of F2029. Nanotubes were assigned as TiNT, and nanoparticles were assigned as AuNPs. The length and shape of TiNT did not change upon binding with the organic linker (F2023). AuNPs were located around nanotubes. HRTEM of F2029 (shown in Figure 62 (c)) showed that the d-spacing of AuNP was 0.24 nm, which corresponded to the (111) surface of

Au[153]. TEM and HRTEM images of F2030 are shown in Figure 62 (d)&(e) and Figure 62 (f), respectively. It showed similar morphology and same d-spacing compared with F2029.

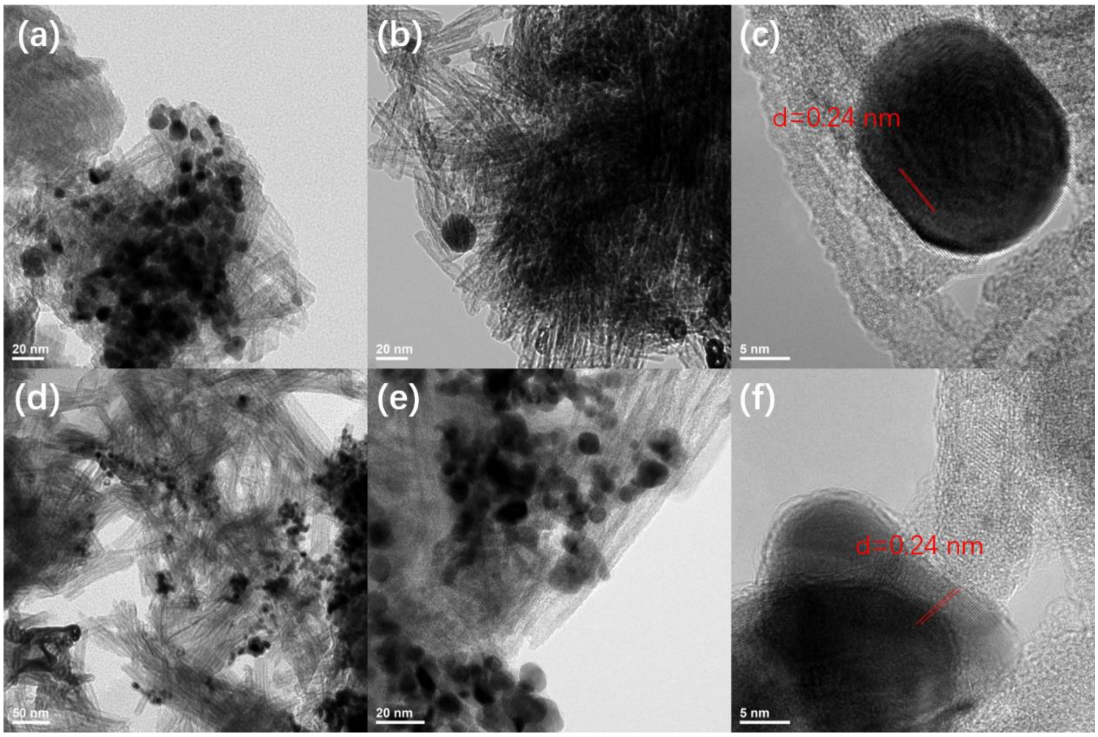

Figure 62 TEM and HRTEM images of (a)-(c): F2029; (d)-(f): F2030. (a) and (b) shows the morphology of F2029, which contained nanotubes from TiNT and nanoparticles from AuNPs. (c) indicated the d-spacing of the nanoparticle, which was 0.24 nm and corresponded to the (111) surface of Au[153].(d)-(f) shows the morphology and HRTEM of F2030, which were similar to F2029.

F2037 I & II

The UV-Vis absorbance of F2037 I and F2037 II is shown in Figure 63. The two samples have shown the same profile within the range of 200-300 nm. For F2037 I, a TiNT band between 300-350 nm and a shoulder started from 350nm could be found. This profile was the same as other TiNT-catechol systems (discussed in Chapter 4), which shows successfully binding between TiNT and deprotected F2031 compound. However, no peak around 520 nm could be seen, which stands for the SPR peak of AuNPs. This indicated that AuNPs existed in the mixture did not bind to TiNT but remained in the filtrate instead. As a result, it was proposed that F2037 I was not an ideal composite. For F2037 II, an increase at 350-450 nm was contributed by the binding between TiNT and the catechol compound. In addition to this, a broad peak at ~550 nm was found, which was the SPR of AuNPs, and the broadness indicated that the size distribution of AuNPs was broad. The morphology of the F2037 II composite was further investigated based on TEM.

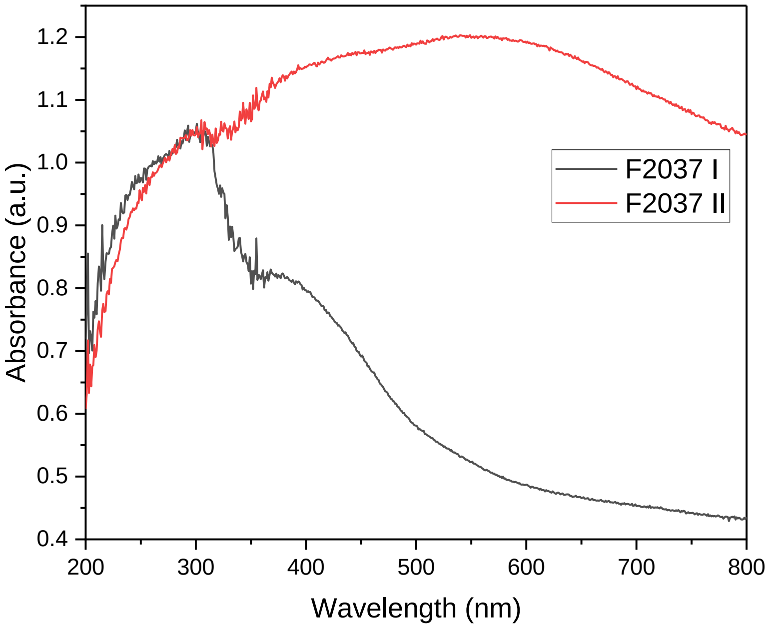

Figure 63 UV-Vis absorbance of F2037 I and F2037 II. TiNT profile and charge transfer band can be found for F2037 I but no SPR peak. Compared to F2037 I, F2037 II has a broad peak at ~550 nm.

Figure 64 (a) & (b) show TEM and Figure 64 (c) & (d) show high resolution TEM images of F2037 II. The tubular structure was TiNT, and it did not change upon modification. AuNPs were found on the nanotube surface. The sizes of nanoparticles observed were from 3-12 nm with an average diameter of 5.6 nm, and the sizes were not quite uniform. From HRTEM, the d-spacing of AuNPs was 0.23 nm, which corresponded to the (111) surface of Au[153].

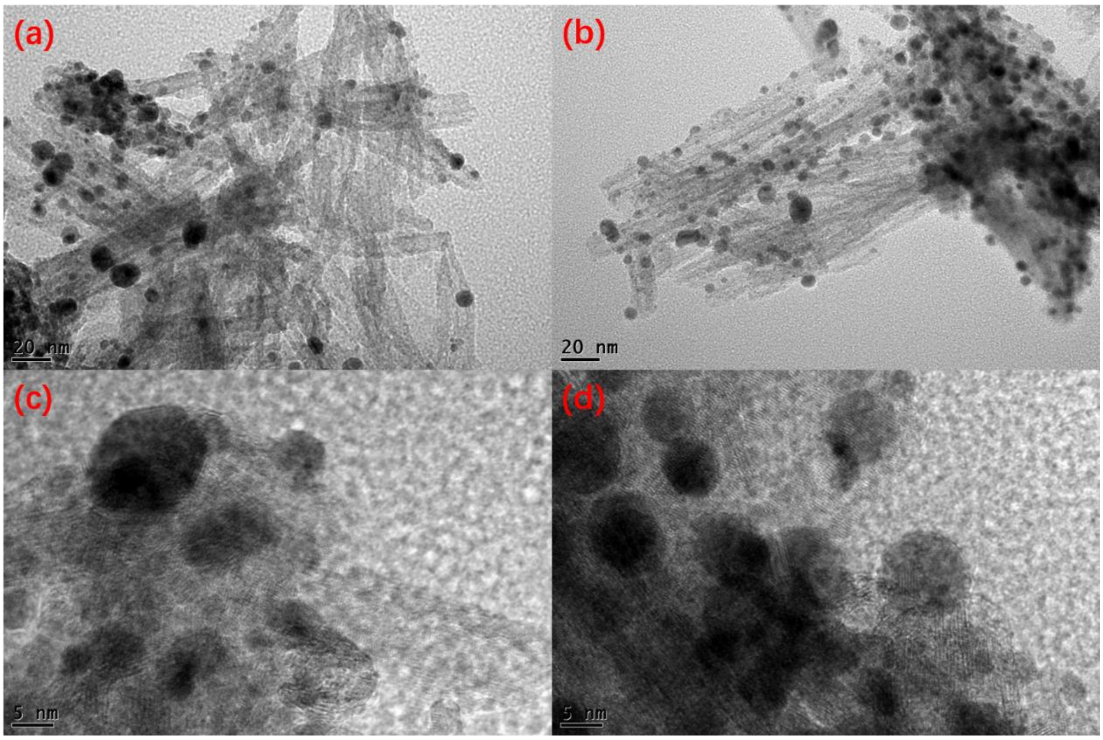

Figure 64 TEM and HRTEM images of F2037 II. (a) and (b) shows the morphology of composite, which contained nanotubes and nanoparticles. (c) and (d) indicated the d-spacing of nanoparticles, which corresponded to the (111) surface of Au[153].

F2050

F2040 is a catechol structure with chloride as the ending group (the structure is shown in the above section). This compound was binding to TiNT first via two hydroxyl groups and resulted in F2041B. Next, a surface reaction, which was a substitution of chloride by thioacetate, was carried out in anhydrous EtOH under room temperature. Potassium thioacetate can dissolve in EtOH when the solubility of product KCl is very low in EtOH[157]. After stirring overnight, a large amount of undissolved solid, which was KCl, was found in the reaction mixture. Thus the reaction occurred. All solid was filtered off, and KCl was washed off by water to give the following product F2042:

Next, the thiol group was deprotected by potassium carbonate in MeOH, and AuNPs were synthesized in the presence of TiNT-thiol. Finally, the purple powder was filtered off and washed to give F2050. UV-Vis absorbance of F2041B, F2042 and F2050 are shown in Figure 66. All three samples have shown a semiconductor band from 300-350 nm, which means the band gap of TiNT did not change. For the two samples without gold, both have shown shoulders at a range of 350-500 nm. This was caused by the charge transfer complex formed between TiNT and the catechol compound.[124, 127] For F2050, the shoulder was not obvious but still could be seen, and a strong SPR peak at ~527 nm was found. Compared with the previous TiNT-thiol-AuNP composite F2037II, the LSPR peak was sharper, which means narrower distribution of AuNPs.

TEM and HRTEM images of F2050 are shown in Figure 65 (a) – (d). From Figure 65 (a) and (b), it was found the sizes of nanoparticles were not uniform, which were from several nanometers to around 100 nm. Figure 65 (c) and (d) showed HRTEM of a large nanoparticle (diameter = 28.5 nm) and a small nanoparticle (diameter = 5nm). Both of them showed similar d-spacing (0.23-0.24 nm), which corresponded to the (111) surface of Au[153].

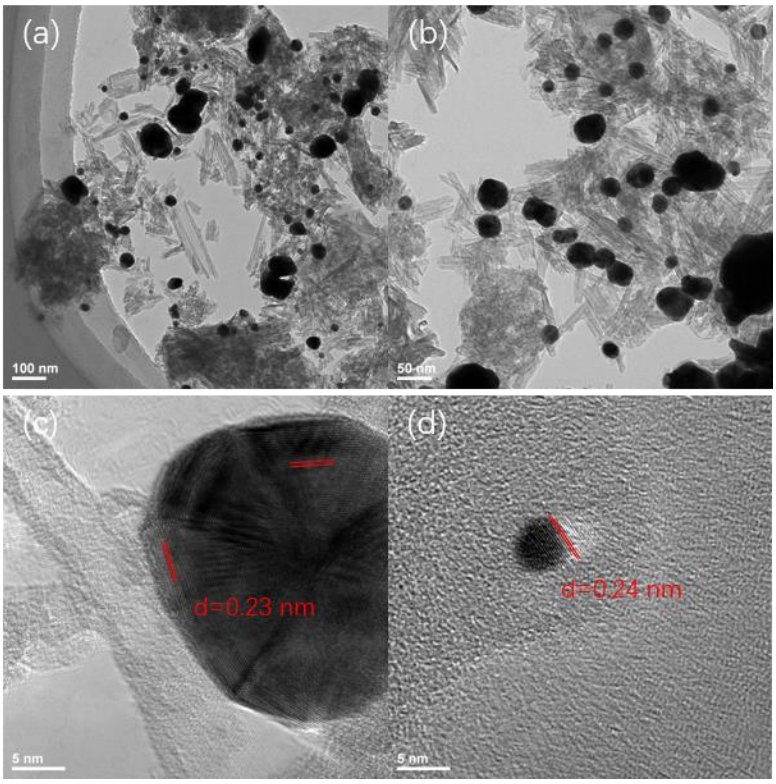

Figure 65 TEM and HRTEM images of F2050. (a) and (b) shows the morphology of composite, which contained nanotubes and nanoparticles. (c) and (d) indicated the d-spacing of nanoparticles, which corresponded to the (111) surface of Au[153].

UV-Vis of F2050 was compared with F2041B and F2042 in Figure 66, which were the precursor of F2050 without adding gold. All three samples showed the TiNT profile, which was a band gap of 3.2 eV. F2041B and F2040 showed an absorbance within the range 350-600 nm, which was caused by the formation of charge transfer complex and the same as other TiNT-catechol samples (discussed in Chapter 4). F2050 showed a significant peak at 526 nm. This peak was a characterization peak of gold nanoparticles, which was attributed to the LSPR effect of AuNPs.

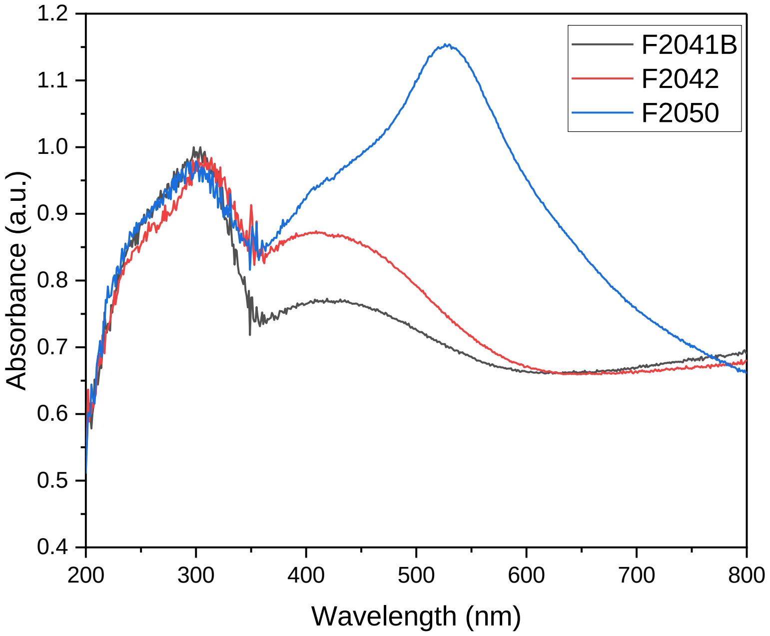

Figure 66 UV-Vis absorbance of F2041B, F2042 and F2050. F2041 B and F2042 show TiNT profile and charge transfer profile, which was similar to other TiNT-catechol systems. F2050 shows a strong peak at 526 nm, which was attributed to the LSPR effect of AuNPs.

XPS results of F2050

Figure 67 shows C1s of F2050. The experimental spectrum was divided into three peaks. The peak at 284.4 eV was assigned as C-C and C=C from both aromatic ring and carbon chain[158], as well as carbon addiction for calibration purposes. The peak at 286.6 eV was dominated by C-O/C-S[159], which was from the hydroxyl groups on the catechol structure and thiol ending group. 288.9 eV was assigned as a C=O double bond. From the proposed F2050 structure, there is no C=O bond. However, the synthesis of organic linker involved substitution by potassium thioacetate as well as hydrolysis of thioacetate group. The existence of C=O signals was explained by residual F2042, in which a contained thioacetate group remained in F2050. The organic linker was bound to TiNT surface thus it remained in F2050 and can hardly be removed.

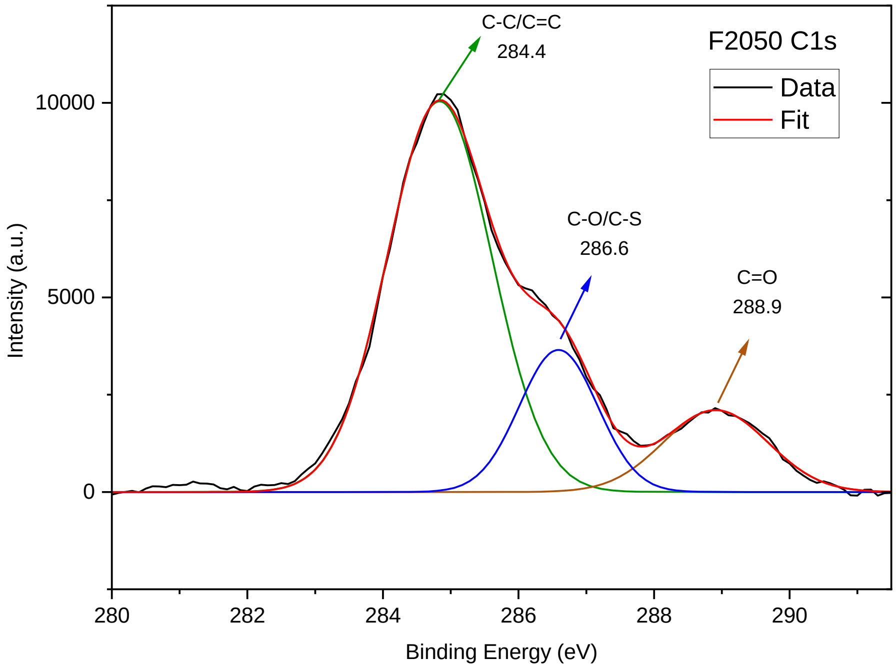

Figure 67 XPS C1s spectrum of F2050. The peak at 284.4 eV was assigned as C-C and C=C from both aromatic ring and carbon chain[158], as well as carbon addiction for calibration purposes. The peak at 286.6 eV was dominated by C-O/C-S[159], which was from the hydroxyl groups on the catechol structure and thiol ending group. 288.9 eV was assigned as a C=O double bond.

Figure 68 shows the XPS O1s spectrum of F2050, and two peaks were fitted. On the one hand, the strong peak at 530.4 eV was also observed at the same position as in TiNT, which was given by O-Ti bonds in the TiNT structure. Upon surface modification of TiNT, the O-Ti peak did not shift, which means the oxidation state of oxygen on the sample surface did not change. On the other hand, a broad peak at 531.4 eV was found in modified samples, which was within the range of binding energy of O-C bonds from organic structure. What is more, it was reported that the binding energy of O-H bonds was within this range as well. O-H bonds exist in the TiNT structure. However, when compared this spectrum with TiNT, it was found that this peak was not at the same position as the O1s peak of TiNT. It was explained that the broad peak at 531.4 eV was contributed by both O-H and O-C bonds from F2050. XPS Ti2p spectrum of F2050 is shown in Figure 69. Compared to TiNT, no obvious difference could be found, which means the oxidation state of Titanium did not change upon adding $NaBH_4$, which was a strong reducing agent for producing AuNPs.

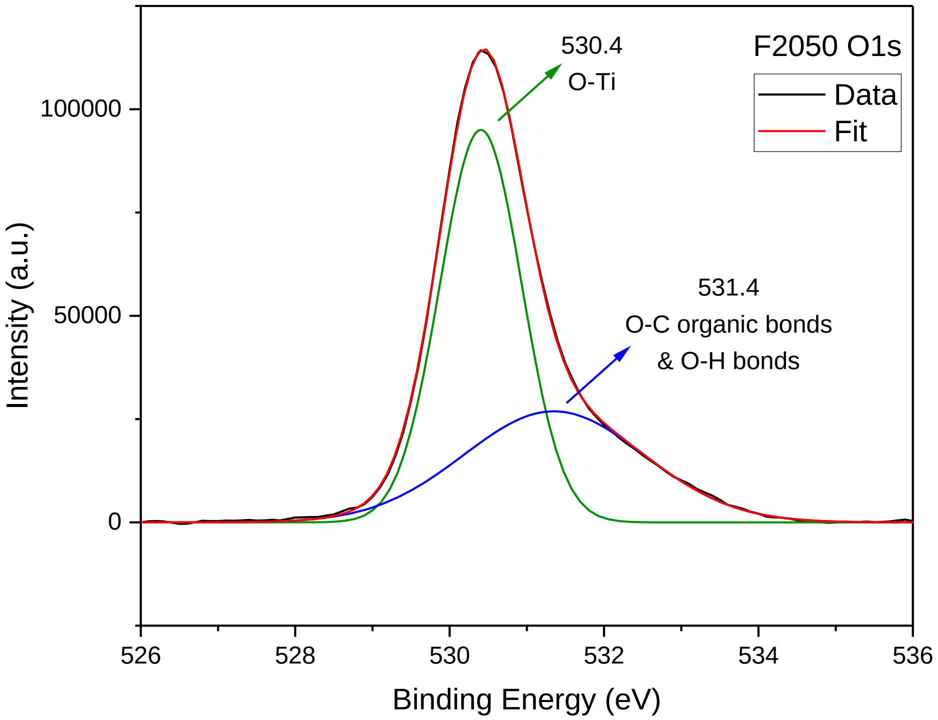

Figure 68 XPS O1s spectrum of F2050. The peak at 530.4 eV was assigned as O-Ti. The broad peak at 531.4 eV was donated by O-C organic bonds and O-H bonds.

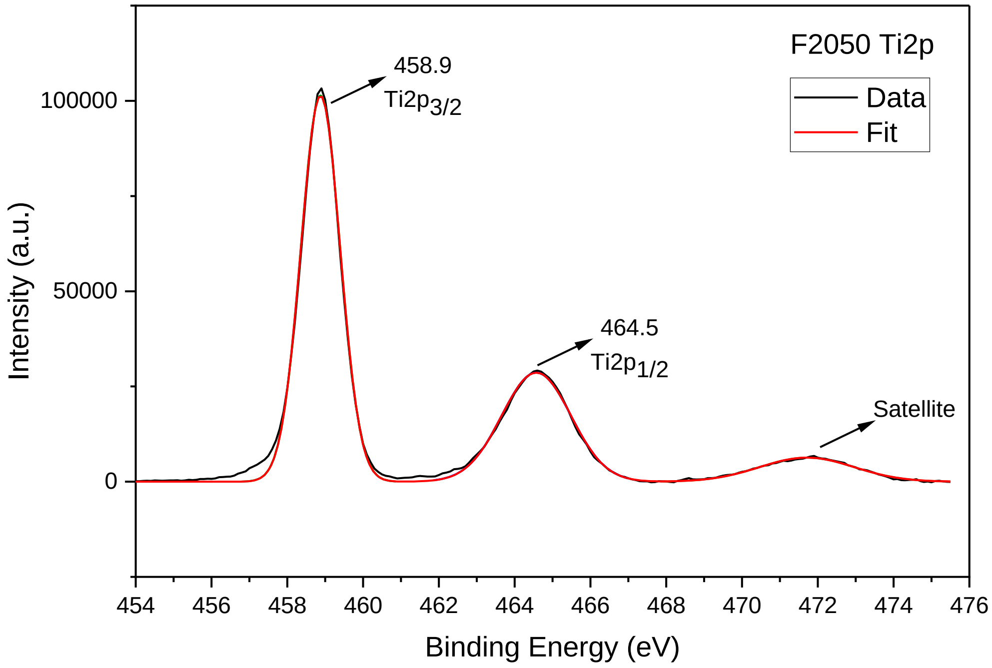

Figure 69 XPS Ti2p spectrum of F2050

Au4f spectrum is shown in Figure 70. The peaks at 83.4 eV and 87.1 eV stands for Au4f$_{7/2}$ and Au4f$_{5/2}$ of Au^0 respectively.[159, 160] No significant signal of Au^1 and Au^3 could be found in the spectrum, which indicated that Au^{3+} from $HAuCl_4$ was successfully reduced to Au^0 by $NaBH_4$. The binding energy of Au4f$_{7/2}$ for Au-S was reported to be 85.05 eV and 85.35 eV for specific samples.[159] However, an additional peak at such position was not able to be fitted to the spectrum, which means Au-S signals were not efficient enough to be detected by XPS. This phenomenon was explained by the principle of XPS as well as the steric structure of the sample. XPS can only provide information on the surfaces of samples. The organic linker, which contains thiol, was bound to the TiNT surface as a thin layer. When AuNPs were produced and bound through thiol, the Au-S bonds formed only between TiNT and AuNPs. Since TiNT and AuNPs were in nanoscale, the Au-S signals were hindered, which could be shown by XPS.

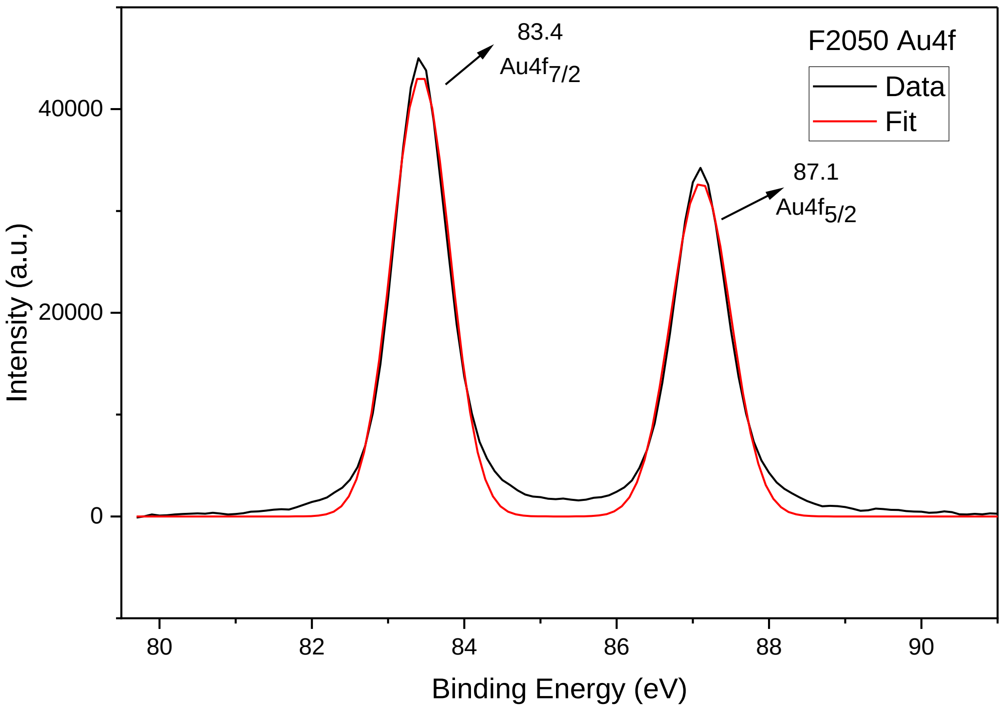

Figure 70 XPS Au4f spectrum of F2050. The peaks at 83.4 eV and 87.1 eV stands for Au4f$_{7/2}$ and Au4f$_{5/2}$ of Au^{0,} respectively.[159, 160]

S2p and Cl2p spectra are shown in Figure 71 (a) and (b). Both spectra have shown very poor signals. From S2p, the signals at range 160-162 eV were higher than other positions. This was explained by the loading of sulphur to the sample. No Cl2p signals could be found, which indicated that all chloride groups were substituted by thioacetate in the previous process.

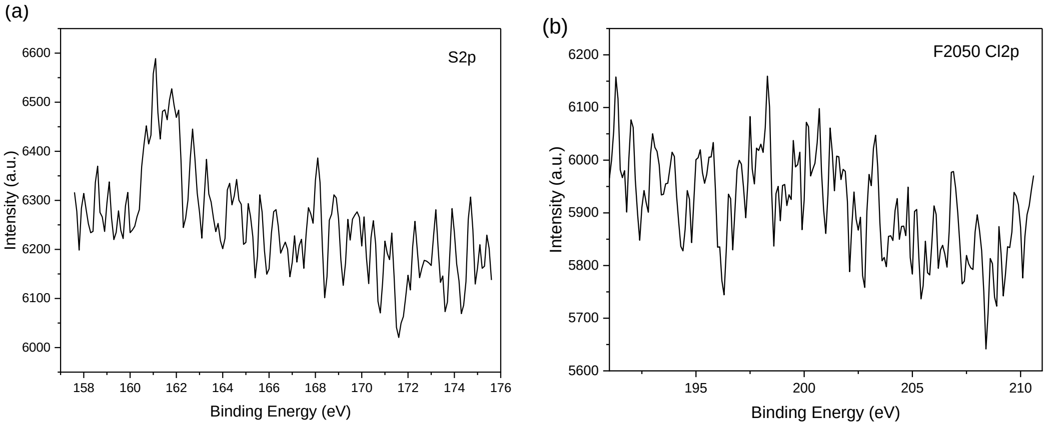

Figure 71 XPS (a) S2p ;(b) Cl2p spectra of F2050

Photodegradation of MB by Au-Organic-TiNT System

Photodegradation of MB catalysed by F2029 and F2030 is shown in Figure 72. Both samples showed good adsorption ability, which removed ~60% of methylene blue. However, their photocatalytic ability was poor.

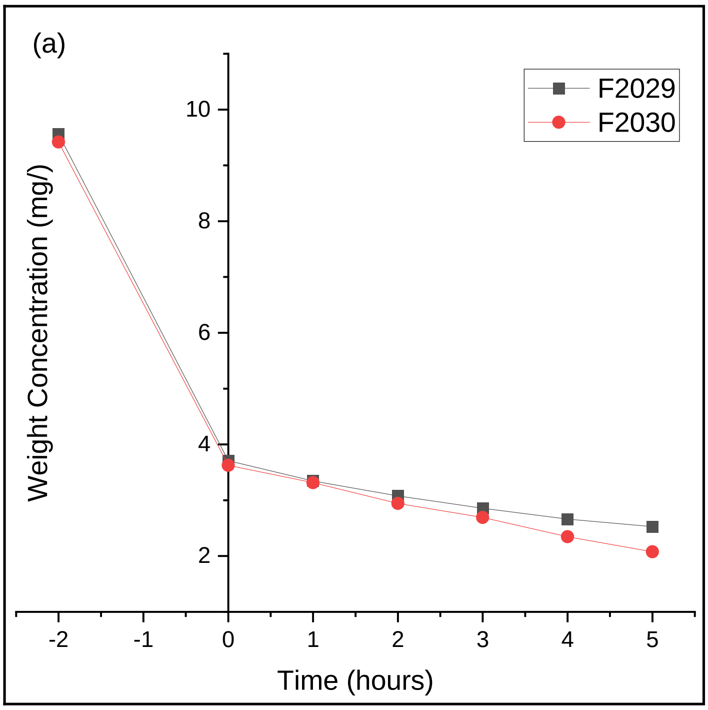

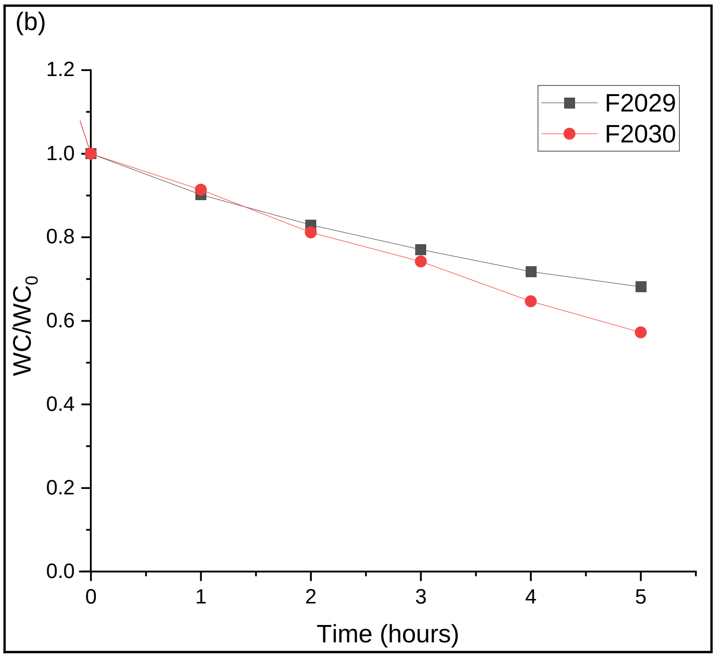

Figure 72 Photodegradation of methylene blue catalysed by F2029 and F2030: (a) Weight concentration changed versus time; (b) Weight concentration ratio changed versus time. Both samples show high adsorption ability, which removed ~60% of methylene blue. However, their photocatalytic ability was poor.

Photodegradation of MB catalysed by F2037 II, F2041B and F2050 are shown in Figure 73. F2037 II and F2050 were TiNT-organic-AuNP composites, and F2041B was for comparison. F2037 II has shown a high adsorption ability. However, all the samples did not show high photodegradation activity. The poor activity was proposed to be caused by the poor charge transfer and weak linking between gold nanoparticles and TiNT, contrary to our hypothesis.

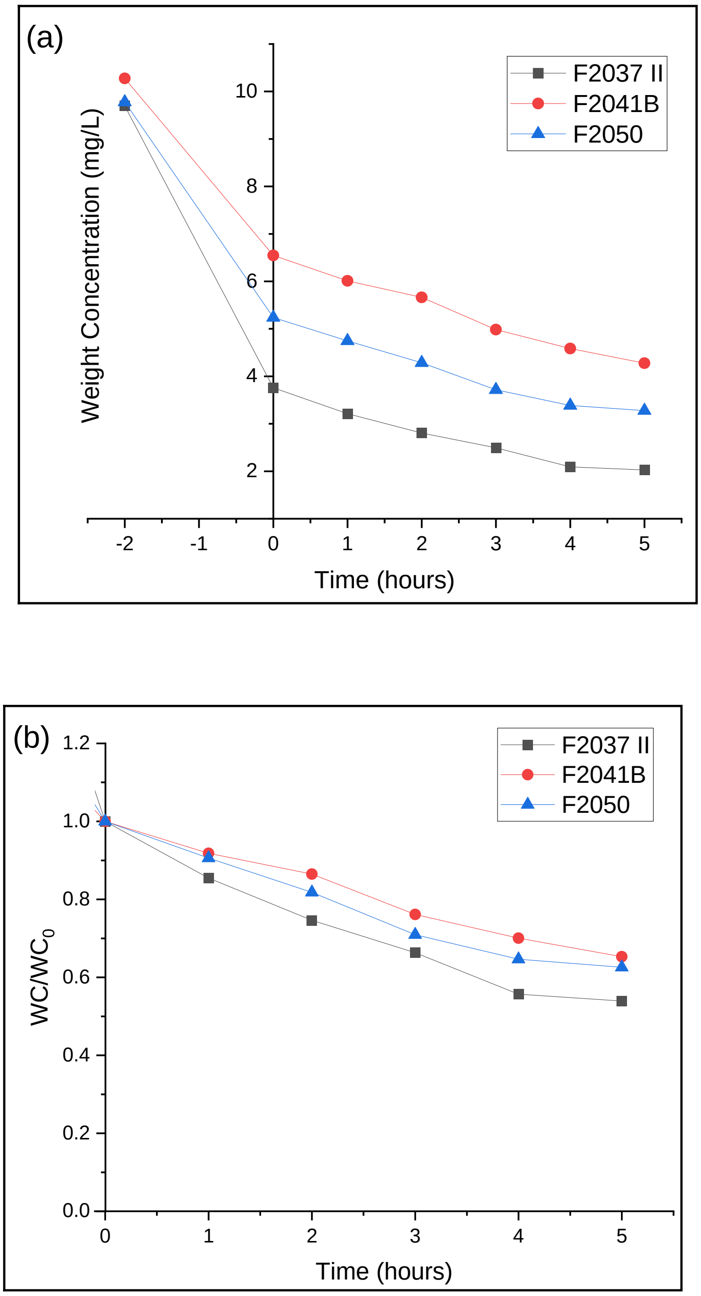

Figure 73 Photodegradation of methylene blue catalysed by F2037 II, F2041B, and F2050: (a) Weight concentration changed versus time; (b) Weight concentration ratio changed versus time. F2037 II shows the highest adsorption ability among the three samples. However, no sample has shown a high degradation ability.

,

6.4 Conclusion

In this chapter, AuNPs were synthesized by the pph_3 method, Brust method, and Martin method. The resulting AuNPs were characterized and compared. The AuNPs prepared by the Martin method was used for further syntheses. Several organic compounds were synthesized from the starting material 4-(Chloroacetyl)catechol. Three compounds that contained a catechol structure, a carbon chain, and a thiol group as an ending group were derived. These compounds were used for synthesizing AuNP-Organic-TiNT composites. Organic compounds attached on TiNT by catechol structure, and AuNPs bound to the thiol group. Three composites were synthesized, and their characterization, including UV-Vis, TEM and XPS, were measured. The photodegradation activity of these composites was tested by photodegradation of methylene blue. However, their activities were not high, and the reason was proposed to be poor charge transfer and weak linking between AuNPs and TiNT.

Chapter 7: Summary and Future Work

In this project, TiNT was modified by several catechol compounds. The characterization of TiNT-catechol compounds showed the formation of charge transfer complex and attachment on TiNT via monodentate attachment. Selective surface enhanced Raman scattering were reported. The enhancement was explained by the charge transfer complex, and the selectivity was explained by the HOMO and LUMO positions of modifiers.

g-C_3N_4-TiNT nanocomposites were synthesized. It was found that TiNT could transform to anatase under high temperatures. The photodegradation activity was highest for the samples heated under 400 ^oC, which was explained by the existence of anatase when the samples heated under 300 ^oC showed high adsorption ability.

AuNPs were synthesized by several methods and compared. Several organic compounds were synthesized from the starting material 4-(Chloroacetyl)catechol. Three compounds were derived and used in synthesizing AuNP-Organic-TiNT composites. Three composites were synthesized and characterized. However, the photodegradation activity of these composites was not high.

The future work of the project includes three parts: investigation of other TiNT-catechol systems for SERS, and explore the potential of these systems using as biosensor; synthesis of conjugated catechol compounds and measure their properties as an organic linker for Au-Organic-TiNT; investigate the photodegradation of methylene blue process by Electron Spin Resonance (ESP), which was on the schedule but delayed by Covid-19 and cannot be measured before submission.

Reference List

1. Pandikumar, A.; Jothivenkatachalam, K., *Photocatalytic Functional Materials for Environmental Remediation*. Wiley: **2019**.
2. Tanaka, K.; Padermpole, K.; Hisanaga, T., Photocatalytic degradation of commercial azo dyes. *Water Research* **2000,** *34* (1), 327-333.
3. Maas, R.; Chaudhari, S., Adsorption and biological decolourization of azo dye Reactive Red 2 in semicontinuous anaerobic reactors. *Process Biochemistry* **2005,** *40* (2), 699-705.
4. Chen, C.; Ma, W.; Zhao, J., Semiconductor-mediated photodegradation of pollutants under visible-light irradiation. *Chemical Society Reviews* **2010,** *39* (11), 4206-4219.
5. Ajmal, A.; Majeed, I.; Malik, R. N.; Idriss, H.; Nadeem, M. A., Principles and mechanisms of photocatalytic dye degradation on TiO2 based photocatalysts: a comparative overview. *RSC Advances* **2014,** *4* (70), 37003-37026.
6. Siffert, B.; Metzger, J.-M., Study of the interaction of titanium dioxide with cellulose fibers in an aqueous medium. *Colloids and Surfaces* **1991,** *53* (1), 79-99.
7. Fox, M. A.; Dulay, M. T., Heterogeneous photocatalysis. *Chemical Reviews* **1993,** *93* (1), 341-357.
8. Tunesi, S.; Anderson, M., Influence of chemisorption on the photodecomposition of salicylic acid and related compounds using suspended titania ceramic membranes. *The Journal of Physical Chemistry* **1991,** *95* (8), 3399-3405.
9. Alaton, I. A.; Balcioglu, I. A.; Bahnemann, D. W., Advanced oxidation of a reactive dyebath effluent: comparison of O3, H2O2/UV-C and TiO2/UV-A processes. *Water Research* **2002,** *36* (5), 1143-1154.
10. Muruganandham, M.; Swaminathan, M., Solar photocatalytic degradation of a reactive azo dye in TiO2-suspension. *Solar Energy Materials and Solar Cells* **2004,** *81* (4), 439-457.
11. Qamar, M.; Saquib, M.; Muneer, M., Photocatalytic degradation of two selected dye derivatives, chromotrope 2B and amido black 10B, in aqueous suspensions of titanium dioxide. *Dyes and Pigments* **2005,** *65* (1), 1-9.
12. Moztahida, M.; Lee, D. S., Photocatalytic degradation of methylene blue with P25/graphene/polyacrylamide hydrogels: Optimization using response surface methodology. *Journal of Hazardous Materials* **2020,** *400*, 123314.
13. Bizani, E.; Fytianos, K.; Poulios, I.; Tsiridis, V., Photocatalytic decolorization and degradation of dye solutions and wastewaters in the presence of titanium dioxide. *Journal of Hazardous Materials* **2006,** *136* (1), 85-94.

14. Neppolian, B.; Choi, H. C.; Sakthivel, S.; Arabindoo, B.; Murugesan, V., Solar light induced and TiO2 assisted degradation of textile dye reactive blue 4. *Chemosphere* **2002,** *46* (8), 1173-1181.
15. Saquib, M.; Muneer, M., Semiconductor mediated photocatalysed degradation of an anthraquinone dye, Remazol Brilliant Blue R under sunlight and artificial light source. *Dyes and Pigments* **2002,** *53* (3), 237-249.
16. Lea, J.; Adesina, A. A., Oxidative degradation of 4-nitrophenol in UV-illuminated titania suspension. *Journal of Chemical Technology & Biotechnology* **2001,** *76* (8), 803-810.
17. Wang, K.; Zhang, J.; Lou, L.; Yang, S.; Chen, Y., UV or visible light induced photodegradation of AO7 on TiO2 particles: the influence of inorganic anions. *Journal of Photochemistry and Photobiology A: Chemistry* **2004,** *165* (1), 201-207.
18. Matthews, R. W.; McEvoy, S. R., Photocatalytic degradation of phenol in the presence of near-UV illuminated titanium dioxide. *Journal of Photochemistry and Photobiology A: Chemistry* **1992,** *64* (2), 231-246.
19. Schirmer, R. H.; Adler, H.; Pickhardt, M.; Mandelkow, E., "Lest we forget you — methylene blue …". *Neurobiology of Aging* **2011,** *32* (12), 2325.e7-2325.e16.
20. Rafatullah, M.; Sulaiman, O.; Hashim, R.; Ahmad, A., Adsorption of methylene blue on low-cost adsorbents: A review. *Journal of Hazardous Materials* **2010,** *177* (1), 70-80.
21. Tan, I. A. W.; Ahmad, A. L.; Hameed, B. H., Adsorption of basic dye on high-surface-area activated carbon prepared from coconut husk: Equilibrium, kinetic and thermodynamic studies. *Journal of Hazardous Materials* **2008,** *154* (1), 337-346.
22. Ghosh, D.; Bhattacharyya, K. G., Adsorption of methylene blue on kaolinite. *Applied Clay Science* **2002,** *20* (6), 295-300.
23. Yao, Y.; Xu, F.; Chen, M.; Xu, Z.; Zhu, Z., Adsorption behavior of methylene blue on carbon nanotubes. *Bioresource Technology* **2010,** *101* (9), 3040-3046.
24. Dawson, G.; Liu, J.; Lu, L.; Chen, W., Dopamine-Modified Trititanate Nanotubes with UV- and Visible-Light Photocatalytic Activity: Coordinative Self-Assembly into a Recyclable Absorber. *ChemCatChem* **2012,** *4* (8), 1133-1138.
25. Michaelis, L.; Granick, S., Metachromasy of Basic Dyestuffs. *Journal of the American Chemical Society* **1945,** *67* (7), 1212-1219.
26. Mills, A.; Wang, J., Photobleaching of methylene blue sensitised by TiO2: an ambiguous system? *Journal of Photochemistry and Photobiology A: Chemistry* **1999,** *127* (1), 123-134.
27. de Tacconi, N. R.; Carmona, J.; Rajeshwar, K., Reversibility of Photoelectrochromism at the TiO₂/Methylene Blue Interface. **1997,** *144*, 2486.

28. Houas, A.; Lachheb, H.; Ksibi, M.; Elaloui, E.; Guillard, C.; Herrmann, J.-M., Photocatalytic degradation pathway of methylene blue in water. *Applied Catalysis B: Environmental* **2001,** *31* (2), 145-157.
29. Height, M. J.; Pratsinis, S. E.; Mekasuwandumrong, O.; Praserthdam, P., Ag-ZnO catalysts for UV-photodegradation of methylene blue. *Applied Catalysis B: Environmental* **2006,** *63* (3), 305-312.
30. Liu, S.; Sun, H.; Liu, S.; Wang, S., Graphene facilitated visible light photodegradation of methylene blue over titanium dioxide photocatalysts. *Chemical Engineering Journal* **2013,** *214*, 298-303.
31. Boonprakob, N.; Wetchakun, N.; Phanichphant, S.; Waxler, D.; Sherrell, P.; Nattestad, A.; Chen, J.; Inceesungvorn, B., Enhanced visible-light photocatalytic activity of g-C3N4/TiO2 films. *Journal of Colloid and Interface Science* **2014,** *417*, 402-409.
32. Lee, C.-K.; Liu, S.-S.; Juang, L.-C.; Wang, C.-C.; Lyu, M.-D.; Hung, S.-H., Application of titanate nanotubes for dyes adsorptive removal from aqueous solution. *Journal of Hazardous Materials* **2007,** *148* (3), 756-760.
33. Liu, R.; Fu, X.; Wang, C.; Dawson, G., Dopamine Surface Modification of Trititanate Nanotubes: Proposed In-Situ Structure Models. *Chemistry – A European Journal* **2016,** *22* (17), 6071-6074.
34. Kazuhito, H.; Hiroshi, I.; Akira, F., TiO 2 Photocatalysis: A Historical Overview and Future Prospects. *Japanese Journal of Applied Physics* **2005,** *44* (12R), 8269.
35. Qu, X.; Alvarez, P. J. J.; Li, Q., Applications of nanotechnology in water and wastewater treatment. *Water Research* **2013,** *47* (12), 3931-3946.
36. Fujihara, K.; Ohno, T.; Matsumura, M., Splitting of water by electrochemical combination of two photocatalytic reactions on TiO2 particles. *Journal of the Chemical Society, Faraday Transactions* **1998,** *94* (24), 3705-3709.
37. Khan, S. U. M.; Al-Shahry, M.; Ingler Jr, W. B., Efficient Photochemical Water Splitting by a Chemically Modified n-TiO2. *ChemInform* **2003,** *34* (2), no-no.
38. Ni, M.; Leung, M. K. H.; Leung, D. Y. C.; Sumathy, K., A review and recent developments in photocatalytic water-splitting using TiO2 for hydrogen production. *Renewable and Sustainable Energy Reviews* **2007,** *11* (3), 401-425.
39. Hoffmann, M. R.; Martin, S. T.; Choi, W.; Bahnemann, D. W., Environmental Applications of Semiconductor Photocatalysis. *Chemical Reviews* **1995,** *95* (1), 69-96.
40. Sun, C.-C.; Chou, T.-C., Kinetics and Mechanism of Photoelectrochemical Oxidation of Nitrite Ion by Using the Rutile Form of a TiO2/Ti Photoelectrode with High Electric Field Enhancement. *Industrial & Engineering Chemistry Research* **1998,** *37* (11), 4207-4214.
41. Fisher, M. B.; Keane, D. A.; Fernández-Ibáñez, P.; Colreavy, J.; Hinder,

S. J.; McGuigan, K. G.; Pillai, S. C., Nitrogen and copper doped solar light active TiO2 photocatalysts for water decontamination. *Applied Catalysis B: Environmental* **2013,** *130*, 8-13.

42. Nelson, B. P.; Candal, R.; Corn, R. M.; Anderson, M. A., Control of Surface and ζ Potentials on Nanoporous TiO2 Films by Potential-Determining and Specifically Adsorbed Ions. *Langmuir* **2000,** *16* (15), 6094-6101.

43. Hamnett, A.; Stevens, P. S.; Wingate, R. D., Nafion®-bonded porous titanium oxide electrodes for oxygen evolution: towards a regenerative fuel cell. *Journal of Applied Electrochemistry* **1991,** *21* (11), 982-985.

44. Bach, U.; Lupo, D.; Comte, P.; Moser, J. E.; Weissortel, F.; Salbeck, J.; Spreitzer, H.; Gratzel, M., Solid-state dye-sensitized mesoporous TiO2 solar cells with high photon-to-electron conversion efficiencies. *Nature* **1998,** *395* (6702), 583-585.

45. Boro, B.; Gogoi, B.; Rajbongshi, B. M.; Ramchiary, A., Nano-structured TiO2/ZnO nanocomposite for dye-sensitized solar cells application: A review. *Renewable and Sustainable Energy Reviews* **2017**.

46. O'Regan, B.; Gratzel, M., A low-cost, high-efficiency solar cell based on dye-sensitized colloidal TiO2 films. *Nature* **1991,** *353* (6346), 737-740.

47. Peng, Z.; Shi, Z.; Liu, M., Mesoporous Sn-TiO composite electrodes for lithium batteries. *Chemical Communications* **2000,** (21), 2125-2126.

48. Tang, Y.; Zhang, Y.; Deng, J.; Wei, J.; Tam, H. L.; Chandran, B. K.; Dong, Z.; Chen, Z.; Chen, X., Mechanical Force-Driven Growth of Elongated Bending TiO2-based Nanotubular Materials for Ultrafast Rechargeable Lithium Ion Batteries. *Advanced Materials* **2014,** *26* (35), 6111-6118.

49. Wang, J.; Polleux, J.; Lim, J.; Dunn, B., Pseudocapacitive Contributions to Electrochemical Energy Storage in TiO2 (Anatase) Nanoparticles. *The Journal of Physical Chemistry C* **2007,** *111* (40), 14925-14931.

50. Landmann, M.; Rauls, E.; Schmidt, W. G., The electronic structure and optical response of rutile, anatase and brookite TiO_2. *Journal of Physics: Condensed Matter* **2012,** *24* (19), 195503.

51. Zhang, Y.; Jiang, Z.; Huang, J.; Lim, L. Y.; Li, W.; Deng, J.; Gong, D.; Tang, Y.; Lai, Y.; Chen, Z., Titanate and titania nanostructured materials for environmental and energy applications: a review. *RSC Advances* **2015,** *5* (97), 79479-79510.

52. Fujishima, A.; Honda, K., Electrochemical Photolysis of Water at a Semiconductor Electrode. *Nature* **1972,** *238* (5358), 37-38.

53. Kraeutler, B.; Jaeger, C. D.; Bard, A. J., Direct observation of radical intermediates in the photo-Kolbe reaction - heterogeneous photocatalytic radical formation by electron spin resonance. *Journal of the American Chemical Society* **1978,** *100* (15), 4903-4905.

54. Kraeutler, B.; Bard, A. J., Heterogeneous photocatalytic preparation of supported catalysts. Photodeposition of platinum on titanium dioxide powder

and other substrates. *Journal of the American Chemical Society* **1978,** *100* (13), 4317-4318.

55. Banerjee, S.; Pillai, S. C.; Falaras, P.; O'Shea, K. E.; Byrne, J. A.; Dionysiou, D. D., New Insights into the Mechanism of Visible Light Photocatalysis. *The Journal of Physical Chemistry Letters* **2014,** *5* (15), 2543-2554.
56. Chen, X.; Mao, S. S., Titanium Dioxide Nanomaterials: Synthesis, Properties, Modifications, and Applications. *Chemical Reviews* **2007,** *107* (7), 2891-2959.
57. Jia, H.; Xiao, W.-J.; Zhang, L.; Zheng, Z.; Zhang, H.; Deng, F., In Situ l-Hydroxyproline Functionalization and Enhanced Photocatalytic Activity of TiO 2 Nanorods. *The Journal of Physical Chemistry C* **2008,** *112* (30), 11379-11384.
58. Rajh, T.; Chen, L. X.; Lukas, K.; Liu, T.; Thurnauer, M. C.; Tiede, D. M., Surface Restructuring of Nanoparticles: An Efficient Route for Ligand−Metal Oxide Crosstalk. *The Journal of Physical Chemistry B* **2002,** *106* (41), 10543-10552.
59. Motonari, A.; Yusuke, M.; Makoto, H.; Susumu, Y., Formation of Titania Nanotubes with High Photo-Catalytic Activity. *Chemistry Letters* **2000,** *29* (8), 942-943.
60. Chen, Q.; Zhou, W.; Du, G. H.; Peng, L.-M., Trititanate Nanotubes Made via a Single Alkali Treatment. *Advanced Materials* **2002,** *14* (17), 1208-1211.
61. Dawson, G.; Chen, W.; Zhang, T.; Chen, Z.; Cheng, X., A study on the effect of starting material phase on the production of trititanate nanotubes. *Solid State Sciences* **2010,** *12* (12), 2170-2176.
62. Kasuga, T.; Hiramatsu, M.; Hoson, A.; Sekino, T.; Niihara, K., Formation of Titanium Oxide Nanotube. *Langmuir* **1998,** *14* (12), 3160-3163.
63. Zhang, S.; Peng, L. M.; Chen, Q.; Du, G. H.; Dawson, G.; Zhou, W. Z., Formation Mechanism of $H_2Ti_3O_7$ Nanotubes. *Physical Review Letters* **2003,** *91* (25), 256103.
64. Bae, C.; Yoo, H.; Kim, S.; Lee, K.; Kim, J.; Sung, M. M.; Shin, H., Template-Directed Synthesis of Oxide Nanotubes: Fabrication, Characterization, and Applications. *Chemistry of Materials* **2008,** *20* (3), 756-767.
65. Gong, D.; Grimes, C. A.; Varghese, O. K.; Hu, W.; Singh, R. S.; Chen, Z.; Dickey, E. C., Titanium oxide nanotube arrays prepared by anodic oxidation. *Journal of Materials Research* **2011,** *16* (12), 3331-3334.
66. Bavykin, D. V.; Walsh, F., *Titanate and Titania Nanotubes Synthesis, Properties and Applications*. 2009; p 1-182.
67. Feist, T. P.; Davies, P. K., The soft chemical synthesis of TiO_2 (B) from layered titanates. *Journal of Solid State Chemistry* **1992,** *101* (2), 275-295.
68. Gao, T.; Fjellvåg, H.; Norby, P., Defect Chemistry of a Zinc-Doped Lepidocrocite Titanate $Cs_xTi_{2-x/2}Zn_{x/2}O_4$ (x = 0.7) and its Protonic Form. *Chemistry of Materials* **2009,** *21* (15), 3503-3513.

69. Bavykin, D. V.; Carravetta, M.; Kulak, A. N.; Walsh, F. C., Application of Magic-Angle Spinning NMR to Examine the Nature of Protons in Titanate Nanotubes. *Chemistry of Materials* **2010,** *22* (8), 2458-2465.
70. Morgado Jr, E.; Jardim, P. M.; Marinkovic, B. A.; Rizzo, F. C.; de Abreu, M. A. S.; Zotin, J. L.; Araújo, A. S., Multistep structural transition of hydrogen trititanate nanotubes into TiO_2-B nanotubes: a comparison study between nanostructured and bulk materials. *Nanotechnology* **2007,** *18* (49), 495710.
71. Leite, M. M.; Martins, V. L.; Vichi, F. M.; Torresi, R. M., Electrochemistry of sodium titanate nanotubes as a negative electrode for sodium-ion batteries. *Electrochimica Acta* **2020,** *331*.
72. Zhao, X.; Lei, Y.; Liu, G.; Qian, L.; Zhang, X.; Ping, Y.; Li, H.; Han, Q.; Fang, P.; He, C., A reclaimed piezoelectric catalyst of MoS2@TNr composites as high-performance anode materials for supercapacitors. *RSC Advances* **2020,** *10* (63), 38715-38726.
73. Bhoomireddy, R. P. R.; Narla, L. G. B.; Peddiahgari, V. G. R., Green synthesis of 1,2,3-triazoles via Cu2O NPs on hydrogen trititanate nanotubes promoted 1,3-dipolar cycloadditions. **2019,** *33* (3), e4752.
74. Liu, H.; Liu, G.; Xie, G.; Zhang, M.; Hou, Z.; He, Z., Gd3+, N-codoped trititanate nanotubes: Preparation, characterization and photocatalytic activity. *Applied Surface Science* **2011,** *257* (8), 3728-3732.
75. Chinnakoti, P.; Vankayala, R. K.; Chunduri, A. L. A.; Nagappagari, L. R.; Muthukonda, S. V.; Kamisetti, V., Trititanate Nanotubes as highly efficient adsorbent for fluoride removal from water: Adsorption performance and uptake mechanism. *Journal of Environmental Chemical Engineering* **2016,** *4* (4, Part A), 4754-4768.
76. Ismael, M.; Wu, Y., A mini-review on the synthesis and structural modification of g-C3N4-based materials, and their applications in solar energy conversion and environmental remediation. *Sustainable Energy & Fuels* **2019,** *3* (11), 2907-2925.
77. Xu, J.; Brenner, T. J. K.; Chabanne, L.; Neher, D.; Antonietti, M.; Shalom, M., Liquid-Based Growth of Polymeric Carbon Nitride Layers and Their Use in a Mesostructured Polymer Solar Cell with Voc Exceeding 1 V. *Journal of the American Chemical Society* **2014,** *136* (39), 13486-13489.
78. Xu, J.; Wang, G.; Fan, J.; Liu, B.; Cao, S.; Yu, J., g-C3N4 modified TiO2 nanosheets with enhanced photoelectric conversion efficiency in dye-sensitized solar cells. *Journal of Power Sources* **2015,** *274*, 77-84.
79.Kessler, F. K.; Zheng, Y.; Schwarz, D.; Merschjann, C.; Schnick, W.; Wang, X.; Bojdys, M. J., Functional carbon nitride materials — design strategies for electrochemical devices. *Nature Reviews Materials* **2017,** *2* (6), 17030.
80. Zhang, Y.; Thomas, A.; Antonietti, M.; Wang, X., Activation of Carbon Nitride Solids by Protonation: Morphology Changes, Enhanced Ionic Conductivity, and Photoconduction Experiments. *Journal of the American*

Chemical Society **2009,** *131* (1), 50-51.
81. Wang, X.; Maeda, K.; Thomas, A.; Takanabe, K.; Xin, G.; Carlsson, J. M.; Domen, K.; Antonietti, M., A metal-free polymeric photocatalyst for hydrogen production from water under visible light. *Nature Materials* **2009,** *8* (1), 76-80.
82. Li, Z.; Luan, Y.; Qu, Y.; Jing, L., Modification Strategies with Inorganic Acids for Efficient Photocatalysts by Promoting the Adsorption of O2. *ACS Applied Materials & Interfaces* **2015,** *7* (41), 22727-22740.
83. Liu, J.; Xie, S.; Geng, Z.; Huang, K.; Fan, L.; Zhou, W.; Qiu, L.; Gao, D.; Ji, L.; Duan, L.; Lu, L.; Li, W.; Bai, S.; Liu, Z.; Chen, W.; Feng, S.; Zhang, Y., Carbon Nitride Supramolecular Hybrid Material Enabled High-Efficiency Photocatalytic Water Treatments. *Nano Letters* **2016,** *16* (10), 6568-6575.
84. Yue, B.; Li, Q.; Iwai, H.; Kako, T.; Ye, J., Hydrogen production using zinc-doped carbon nitride catalyst irradiated with visible light. *Science and technology of advanced materials* **2011,** *12* (3), 034401.
85. Tonda, S.; Kumar, S.; Kandula, S.; Shanker, V., Fe-doped and -mediated graphitic carbon nitride nanosheets for enhanced photocatalytic performance under natural sunlight. *Journal of Materials Chemistry A* **2014,** *2* (19), 6772-6780.
86. Wei, F.; Liu, Y.; Zhao, H.; Ren, X.; Liu, J.; Hasan, T.; Chen, L.; Li, Y.; Su, B.-L., Oxygen self-doped g-C3N4 with tunable electronic band structure for unprecedentedly enhanced photocatalytic performance. *Nanoscale* **2018,** *10* (9), 4515-4522.
87. Wang, K.; Li, Q.; Liu, B.; Cheng, B.; Ho, W.; Yu, J., Sulfur-doped g-C3N4 with enhanced photocatalytic CO2-reduction performance. *Applied Catalysis B: Environmental* **2015,** *176-177*, 44-52.
88. Zhou, Y.; Zhang, L.; Liu, J.; Fan, X.; Wang, B.; Wang, M.; Ren, W.; Wang, J.; Li, M.; Shi, J., Brand new P-doped g-C3N4: enhanced photocatalytic activity for H2 evolution and Rhodamine B degradation under visible light. *Journal of Materials Chemistry A* **2015,** *3* (7), 3862-3867.
89. Patnaik, S.; Martha, S.; Madras, G.; Parida, K., The effect of sulfate pre-treatment to improve the deposition of Au-nanoparticles in a gold-modified sulfated g-C3N4 plasmonic photocatalyst towards visible light induced water reduction reaction. *Physical Chemistry Chemical Physics* **2016,** *18* (41), 28502-28514.
90. Lei, J.; Liu, F.; Wang, L.; Liu, Y.; Zhang, J., A binary polymer composite of graphitic carbon nitride and poly(diphenylbutadiyne) with enhanced visible light photocatalytic activity. *RSC Advances* **2017,** *7* (44), 27377-27383.
91. Sun, J.-X.; Yuan, Y.-P.; Qiu, L.-G.; Jiang, X.; Xie, A.-J.; Shen, Y.-H.; Zhu, J.-F., Fabrication of composite photocatalyst g-C3N4–ZnO and enhancement of photocatalytic activity under visible light. *Dalton Transactions* **2012,** *41* (22),

6756-6763.

92. He, Y.; Wang, Y.; Zhang, L.; Teng, B.; Fan, M., High-efficiency conversion of CO2 to fuel over ZnO/g-C3N4 photocatalyst. *Applied Catalysis B: Environmental* **2015,** *168-169*, 1-8.

93. Yang, M.; Liu, J.; Zhang, X.; Qiao, S.; Huang, H.; Liu, Y.; Kang, Z., C3N4-sensitized TiO2 nanotube arrays with enhanced visible-light photoelectrochemical performance. *Physical Chemistry Chemical Physics* **2015,** *17* (27), 17887-17893.

94. Li, Y.; Wang, R.; Li, H.; Wei, X.; Feng, J.; Liu, K.; Dang, Y.; Zhou, A., Efficient and Stable Photoelectrochemical Seawater Splitting with TiO2@g-C3N4 Nanorod Arrays Decorated by Co-Pi. *The Journal of Physical Chemistry C* **2015,** *119* (35), 20283-20292.

95. Zhou, X.; Peng, F.; Wang, H.; Yu, H.; Fang, Y., Carbon nitride polymer sensitized TiO2 nanotube arrays with enhanced visible light photoelectrochemical and photocatalytic performance. *Chemical Communications* **2011,** *47* (37), 10323-10325.

96. Wen, J.; Xie, J.; Chen, X.; Li, X., A review on g-C3N4-based photocatalysts. *Applied Surface Science* **2017,** *391*, 72-123.

97. Zhang, Y.; Liu, J.; Wu, G.; Chen, W., Porous graphitic carbon nitride synthesized via direct polymerization of urea for efficient sunlight-driven photocatalytic hydrogen production. *Nanoscale* **2012,** *4* (17), 5300-5303.

98. Dong, F.; Wu, L.; Sun, Y.; Fu, M.; Wu, Z.; Lee, S. C., Efficient synthesis of polymeric g-C3N4 layered materials as novel efficient visible light driven photocatalysts. *Journal of Materials Chemistry* **2011,** *21* (39), 15171-15174.

99. Moskovits, M., Surface-enhanced Raman spectroscopy: a brief retrospective. *Journal of Raman Spectroscopy* **2005,** *36* (6-7), 485-496.

100. Singh, P., *Surface plasmon resonance*. New York : Novinka, [2014]: 2014.

101. Maier, S. A., *Plasmonics: Fundamentals and Applications*. Springer: 2007.

102. P, K. C. a. M., *Introduction to Solid State Physics*. New York: Wiley: 1996.

103. Willets, K. A.; Van Duyne, R. P., Localized surface plasmon resonance spectroscopy and sensing. *Annual review of physical chemistry* **2007,** *58*, 267-97.

104. M, K. U. a. V., *Optical Properties of Metal Clusters*. Springer-Verlag Berlin Heidelberg: 1995.

105. Zeng, S.; Baillargeat, D.; Ho, H.-P.; Yong, K.-T., Nanomaterials enhanced surface plasmon resonance for biological and chemical sensing applications. *Chemical Society Reviews* **2014,** *43* (10), 3426-3452.

106. Wu, N., Plasmonic metal–semiconductor photocatalysts and photoelectrochemical cells: a review. *Nanoscale* **2018,** *10* (6), 2679-2696.

107. Cushing, S. K.; Li, J.; Meng, F.; Senty, T. R.; Suri, S.; Zhi, M.; Li, M.; Bristow, A. D.; Wu, N., Photocatalytic Activity Enhanced by Plasmonic Resonant Energy Transfer from Metal to Semiconductor. *Journal of the American Chemical Society* **2012,** *134* (36), 15033-15041.
108. Li, J.; Cushing, S. K.; Meng, F.; Senty, T. R.; Bristow, A. D.; Wu, N., Plasmon-induced resonance energy transfer for solar energy conversion. *Nature Photonics* **2015,** *9* (9), 601-607.
109. Derkacs, D.; Lim, S. H.; Matheu, P.; Mar, W.; Yu, E. T., Improved performance of amorphous silicon solar cells via scattering from surface plasmon polaritons in nearby metallic nanoparticles. **2006,** *89* (9), 093103.
110. Schaadt, D. M.; Feng, B.; Yu, E. T., Enhanced semiconductor optical absorption via surface plasmon excitation in metal nanoparticles. **2005,** *86* (6), 063106.
111. Tian, Y.; Tatsuma, T., Mechanisms and Applications of Plasmon-Induced Charge Separation at TiO2 Films Loaded with Gold Nanoparticles. *Journal of the American Chemical Society* **2005,** *127* (20), 7632-7637.
112. Tian, Y.; Tatsuma, T., Plasmon-induced photoelectrochemistry at metal nanoparticles supported on nanoporous TiO2. *Chemical Communications* **2004,** (16), 1810-1811.
113. Skoog, D. A.; Holler, F. J.; Crouch, S. R., *Principles of instrumental analysis*. 6th ed. / ed.; Belmont (Calif.) : Thomson: 2007.
114. Kohli, R., Chapter 3 - Methods for Monitoring and Measuring Cleanliness of Surfaces. In *Developments in Surface Contamination and Cleaning*, Kohli, R.; Mittal, K. L., Eds. William Andrew Publishing: Oxford, 2012; pp 107-178.
115. Bragg, W. L., The diffraction of short electromagnetic Waves by a Crystal. **1929,** *23* (45), 153 %J Scientia.
116. Speight, J. G., Chapter Five - Sources and Types of Inorganic Pollutants. In *Environmental Inorganic Chemistry for Engineers*, Speight, J. G., Ed. Butterworth-Heinemann: 2017; pp 231-282.
117. Liu, Y.-F.; Lee, Y.-L., Adsorption characteristics of OH-terminated alkanethiol and arenethiol on Au(111) surfaces. *Nanoscale* **2012,** *4* (6), 2093-2100.
118. Lal, S.; Grady, N. K.; Goodrich, G. P.; Halas, N. J., Profiling the Near Field of a Plasmonic Nanoparticle with Raman-Based Molecular Rulers. *Nano Letters* **2006,** *6* (10), 2338-2343.
119. McFarland, A. D.; Young, M. A.; Dieringer, J. A.; Van Duyne, R. P., Wavelength-Scanned Surface-Enhanced Raman Excitation Spectroscopy. *The Journal of Physical Chemistry B* **2005,** *109* (22), 11279-11285.
120. Le Ru, E. C.; Blackie, E.; Meyer, M.; Etchegoin, P. G., Surface Enhanced Raman Scattering Enhancement Factors: A Comprehensive Study. *The Journal of Physical Chemistry C* **2007,** *111* (37), 13794-13803.
121. Hu, Y.; Shi, Y.; Jiang, H.; Huang, G.; Li, C., Scalable Preparation of

Ultrathin Silica-Coated Ag Nanoparticles for SERS Application. *ACS Applied Materials & Interfaces* **2013,** *5* (21), 10643-10649.

122. Qi, D.; Lu, L.; Wang, L.; Zhang, J., Improved SERS Sensitivity on Plasmon-Free TiO2 Photonic Microarray by Enhancing Light-Matter Coupling. *Journal of the American Chemical Society* **2014,** *136* (28), 9886-9889.

123. Gottlieb, H. E.; Kotlyar, V.; Nudelman, A., NMR Chemical Shifts of Common Laboratory Solvents as Trace Impurities. *The Journal of Organic Chemistry* **1997,** *62* (21), 7512-7515.

124. Hurst, S. J.; Fry, H. C.; Gosztola, D. J.; Rajh, T., Utilizing Chemical Raman Enhancement: A Route for Metal Oxide Support-Based Biodetection. *The Journal of Physical Chemistry C* **2011,** *115* (3), 620-630.

125. Tae, E. L.; Lee, S. H.; Lee, J. K.; Yoo, S. S.; Kang, E. J.; Yoon, K. B., A Strategy To Increase the Efficiency of the Dye-Sensitized TiO2 Solar Cells Operated by Photoexcitation of Dye-to-TiO2 Charge-Transfer Bands. *The Journal of Physical Chemistry B* **2005,** *109* (47), 22513-22522.

126. Hilal, H. S.; Majjad, L. Z.; Zaatar, N.; El-Hamouz, A., Dye-effect in TiO2 catalyzed contaminant photo-degradation: Sensitization vs. charge-transfer formalism. *Solid State Sciences* **2007,** *9* (1), 9-15.

127. Kim, S.; Choi, W., Visible-Light-Induced Photocatalytic Degradation of 4-Chlorophenol and Phenolic Compounds in Aqueous Suspension of Pure Titania: Demonstrating the Existence of a Surface-Complex-Mediated Path. *The Journal of Physical Chemistry B* **2005,** *109* (11), 5143-5149.

128. The reflection of X-rays by crystals. *Proceedings of the Royal Society of London. Series A* **1913,** *88* (605), 428.

129. Watt, A. A. R.; Bothma, J. P.; Meredith, P., The supramolecular structure of melanin. *Soft Matter* **2009,** *5* (19), 3754-3760.

130. Coats, A. W.; Redfern, J. P., Thermogravimetric analysis. A review. *Analyst* **1963,** *88* (1053), 906-924.

131. Musumeci, A.; Gosztola, D.; Schiller, T.; Dimitrijevic, N. M.; Mujica, V.; Martin, D.; Rajh, T., SERS of Semiconducting Nanoparticles (TiO2 Hybrid Composites). *Journal of the American Chemical Society* **2009,** *131* (17), 6040-6041.

132. Lee, N. S.; Hsieh, Y. Z.; Paisley, R. F.; Morris, M. D., Surface-enhanced Raman spectroscopy of the catecholamine neurotransmitters and related compounds. *Analytical Chemistry* **1988,** *60* (5), 442-446.

133. Salama, S.; Stong, J. D.; Neilands, J. B.; Spiro, T. G., Electronic and resonance Raman spectra of iron(III) complexes of enterobactin, catechol, and N-methyl-2,3-dihydroxybenzamide. *Biochemistry* **1978,** *17* (18), 3781-3785.

134. Cornard, J.-P.; Rasmiwetti; Merlin, J.-C., Molecular structure and spectroscopic properties of 4-nitrocatechol at different pH: UV–visible, Raman, DFT and TD-DFT calculations. *Chemical Physics* **2005,** *309* (2), 239-249.

135. Liu, R.; Morris, E.; Cheng, X.; Amigues, E.; Lau, K.; Kim, B.; Liu,

Y.; Ke, Z.; Ashbrook, S. E.; Bühl, M.; Dawson, G., SERS of Trititanate Nanotubes: Selective Enhancement of Catechol Compounds. **2018,** *3* (28), 8338-8343.

136. Liu, J.; Zhang, T.; Wang, Z.; Dawson, G.; Chen, W., Simple pyrolysis of urea into graphitic carbon nitride with recyclable adsorption and photocatalytic activity. *Journal of Materials Chemistry* **2011,** *21* (38), 14398-14401.

137. Zhang, J.; Zhang, G.; Chen, X.; Lin, S.; Möhlmann, L.; Dołęga, G.; Lipner, G.; Antonietti, M.; Blechert, S.; Wang, X., Co-Monomer Control of Carbon Nitride Semiconductors to Optimize Hydrogen Evolution with Visible Light. *Angewandte Chemie International Edition* **2012,** *51* (13), 3183-3187.

138. Zhang, J.; Zhang, M.; Zhang, G.; Wang, X., Synthesis of Carbon Nitride Semiconductors in Sulfur Flux for Water Photoredox Catalysis. *ACS Catalysis* **2012,** *2* (6), 940-948.

139. Dong, F.; Wang, Z.; Sun, Y.; Ho, W.-K.; Zhang, H., Engineering the nanoarchitecture and texture of polymeric carbon nitride semiconductor for enhanced visible light photocatalytic activity. *Journal of Colloid and Interface Science* **2013,** *401*, 70-79.

140. XPS Elements Table. https://xpssimplified.com/periodictable.php (accessed 28.Jun).

141. Huang, Z. a.; Sun, Q.; Lv, K.; Zhang, Z.; Li, M.; Li, B., Effect of contact interface between TiO2 and g-C3N4 on the photoreactivity of g-C3N4/TiO2 photocatalyst: (001) vs (101) facets of TiO2. *Applied Catalysis B: Environmental* **2015,** *164*, 420-427.

142. Yang, Y.; Zeng, Z.; Zeng, G.; Huang, D.; Xiao, R.; Zhang, C.; Zhou, C.; Xiong, W.; Wang, W.; Cheng, M.; Xue, W.; Guo, H.; Tang, X.; He, D., Ti3C2 Mxene/porous g-C3N4 interfacial Schottky junction for boosting spatial charge separation in photocatalytic H2O2 production. *Applied Catalysis B: Environmental* **2019,** *258*, 117956.

143. Chen, X.; Liu, L.; Yu, P. Y.; Mao, S. S., Increasing Solar Absorption for Photocatalysis with Black Hydrogenated Titanium Dioxide Nanocrystals. *Science* **2011,** *331* (6018), 746.

144. Shanker, U.; Jassal, V.; Rani, M., Catalytic removal of organic colorants from water using some transition metal oxide nanoparticles synthesized under sunlight. *RSC Advances* **2016,** *6* (97), 94989-94999.

145. Rauf, M. A.; Meetani, M. A.; Khaleel, A.; Ahmed, A., Photocatalytic degradation of Methylene Blue using a mixed catalyst and product analysis by LC/MS. *Chemical Engineering Journal* **2010,** *157* (2), 373-378.

146. Wang, Y.; Wang, X.; Antonietti, M., Polymeric Graphitic Carbon Nitride as a Heterogeneous Organocatalyst: From Photochemistry to Multipurpose Catalysis to Sustainable Chemistry. *Angewandte Chemie International Edition* **2012,** *51* (1), 68-89.

147. Gleiter, H., Nanostructured materials: basic concepts and microstructure. *Acta Materialia* **2000,** *48* (1), 1-29.

148. Brust, M.; Walker, M.; Bethell, D.; Schiffrin, D. J.; Whyman, R., Synthesis of thiol-derivatised gold nanoparticles in a two-phase Liquid-Liquid system. *Journal of the Chemical Society, Chemical Communications* **1994,** (7), 801-802.

149. Martin, M. N.; Basham, J. I.; Chando, P.; Eah, S.-K., Charged Gold Nanoparticles in Non-Polar Solvents: 10-min Synthesis and 2D Self-Assembly. *Langmuir* **2010,** *26* (10), 7410-7417.

150. Chang, Y.-A.; Ares, J.; Anderson, K.; Sabol, B.; Wallace, R. A.; Farooqui, T.; Uretsky, N.; Miller, D. D., Dopamine agonists: effects of charged and uncharged analogs of dopamine. *Journal of Medicinal Chemistry* **1987,** *30* (1), 214-218.

151. Bastús, N. G.; Comenge, J.; Puntes, V., Kinetically Controlled Seeded Growth Synthesis of Citrate-Stabilized Gold Nanoparticles of up to 200 nm: Size Focusing versus Ostwald Ripening. *Langmuir* **2011,** *27* (17), 11098-11105.

152. Woehrle, G. H.; Brown, L. O.; Hutchison, J. E., Thiol-Functionalized, 1.5-nm Gold Nanoparticles through Ligand Exchange Reactions: Scope and Mechanism of Ligand Exchange. *Journal of the American Chemical Society* **2005,** *127* (7), 2172-2183.

153. Moniri, S.; Reza Hantehzadeh, M.; Ghoranneviss, M.; Asadi Asadabad, M., Au-Pt alloy nanoparticles obtained by nanosecond laser irradiation of gold and platinum bulk targets in an ethylene glycol solution. *The European Physical Journal Plus* **2017,** *132* (7), 318.

154. Kislina, I. S.; Librovich, N. B.; Maiorov, V. D.; Tarakanova, E. G.; Yukhnevich, G. V., The Structure of DMF · HCl and DMF · (HCl)2 Complexes according to ab initio Calculations. *Kinetics and Catalysis* **2002,** *43* (5), 671-674.

155. Clemmensen, E., Reduktion von Ketonen und Aldehyden zu den entsprechenden Kohlenwasserstoffen unter Anwendung von amalgamiertem Zink und Salzsäure. **1913,** *46* (2), 1837-1843.

156. Kishner, N., Wolff–Kishner reduction; Huang–Minlon modification. *J. Russ. Phys. Chem. Soc* **1911,** *43*, 582-595.

157. Pinho, S. P.; Macedo, E. A., Solubility of NaCl, NaBr, and KCl in Water, Methanol, Ethanol, and Their Mixed Solvents. *Journal of Chemical & Engineering Data* **2005,** *50* (1), 29-32.

158. Li, S.; Peng, Y.; Hu, C.; Chen, Z., Self-assembled synthesis of benzene-ring-grafted g-C3N4 nanotubes for enhanced photocatalytic H2 evolution. *Applied Catalysis B: Environmental* **2020,** *279*, 119401.

159. Vitale, F.; Fratoddi, I.; Battocchio, C.; Piscopiello, E.; Tapfer, L.; Russo, M. V.; Polzonetti, G.; Giannini, C., Mono- and bi-functional arenethiols as surfactants for gold nanoparticles: synthesis and characterization. *Nanoscale*

Research Letters **2011,** *6* (1), 103.
160. Casaletto, M. P.; Longo, A.; Martorana, A.; Prestianni, A.; Venezia, A. M., XPS study of supported gold catalysts: the role of Au0 and Au+δ species as active sites. **2006,** *38* (4), 215-218.

Appendix

Appendix 1: GC-MS results of photodegradation product

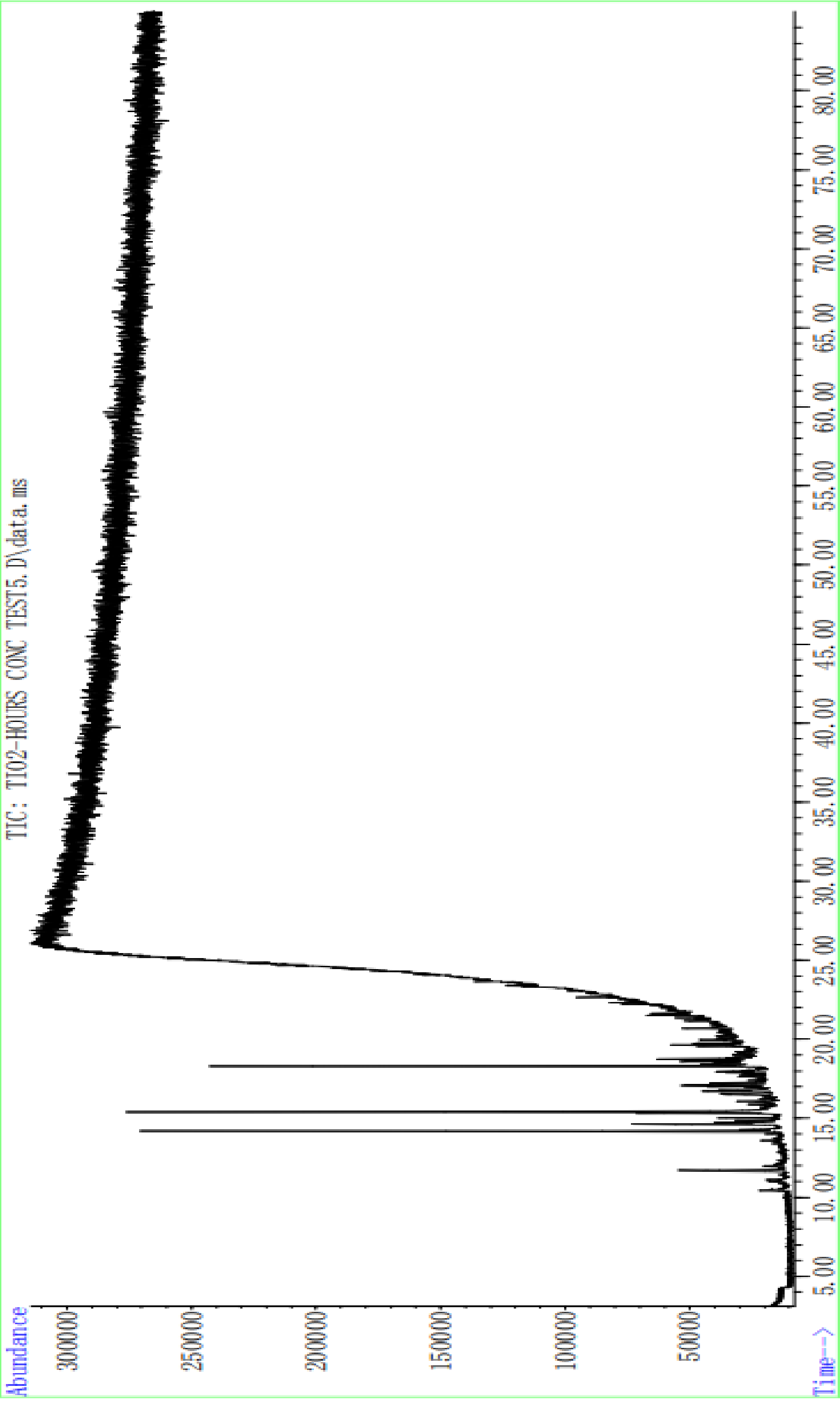

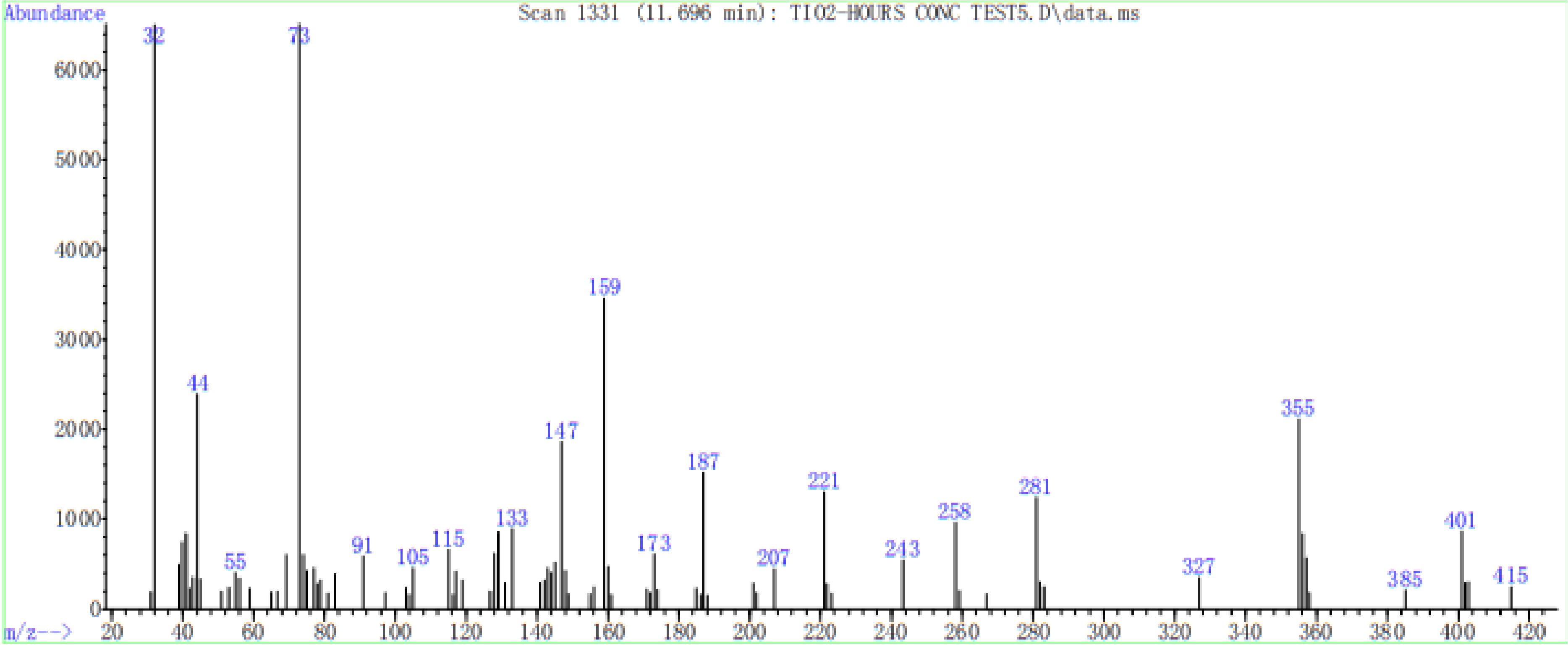
Scan 1331 (11.696 min): TIO2-HOURS CONC TEST5.D\data.ms
Abundance
6000
5000
4000
3000
2000
1000
0
m/z-->
20
40
60
80
100
120
140
160
180
200
220
240
260
280
300
320
340
360
380
400
420
32
73
44
55
91
105
115
133
147
159
173
187
207
221
243
258
281
327
355
385
401
415

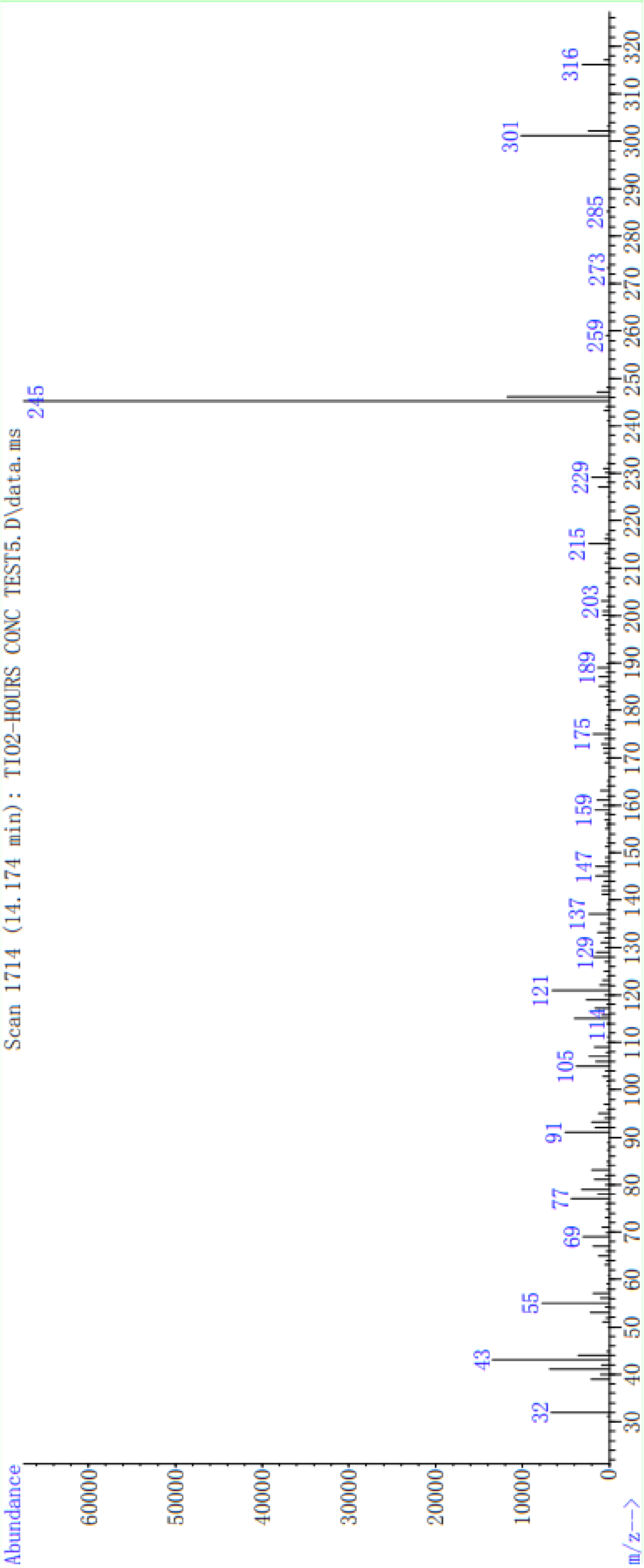
Scan 1714 (14.174 min): TIO2-HOURS CONC TEST5.D\data.ms
Abundance
60000
50000
40000
30000
20000
10000
0
m/z-->
30
40
50
60
70
80
90
100
110
120
130
140
150
160
170
180
190
200
210
220
230
240
250
260
270
280
290
300
310
320
32
43
55
69
77
91
105
114
121
129
137
147
159
175
189
203
215
229
245
259
273
285
301
316

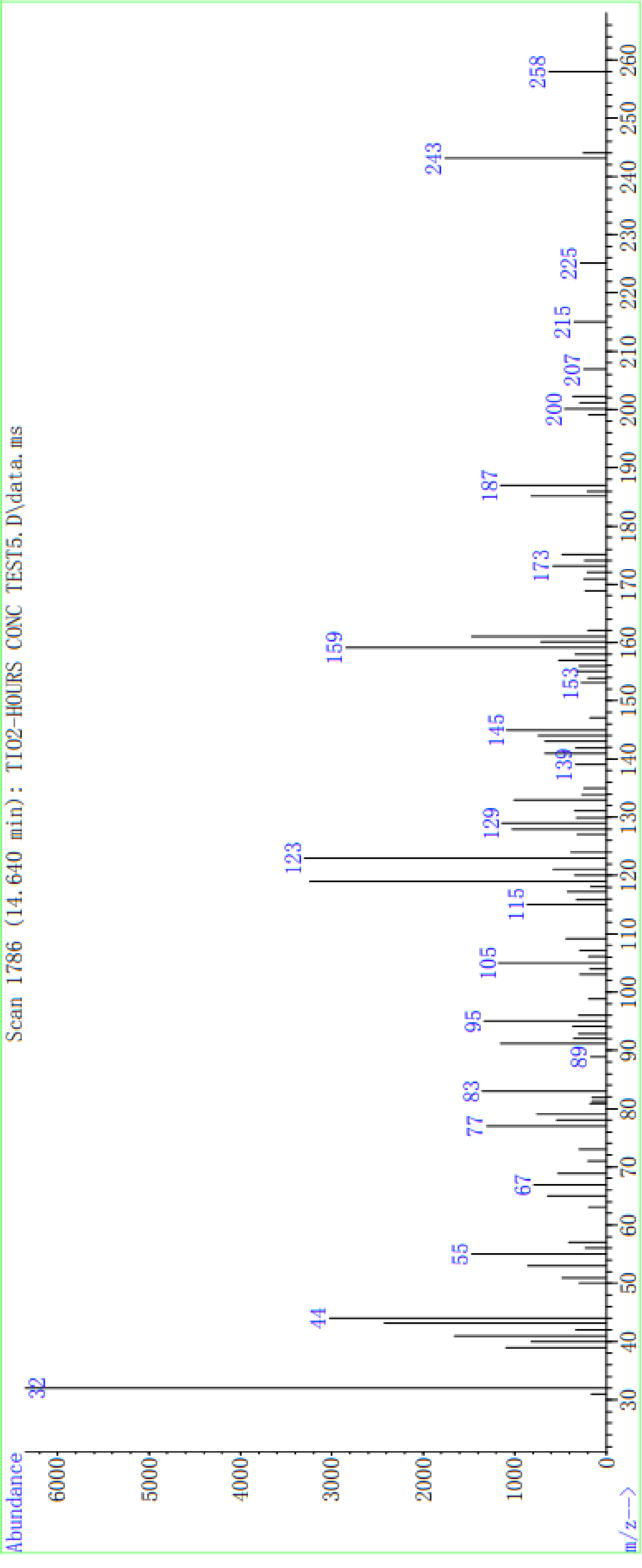
Scan 1786 (14.640 min): TIO2-HOURS CONC TEST5.D\data.ms
Abundance
6000
5000
4000
3000
2000
1000
0
m/z-->
30
40
50
60
70
80
90
100
110
120
130
140
150
160
170
180
190
200
210
220
230
240
250
260
32
44
55
67
77
83
89
95
105
115
123
129
139
145
153
159
173
187
200
207
215
225
243
258

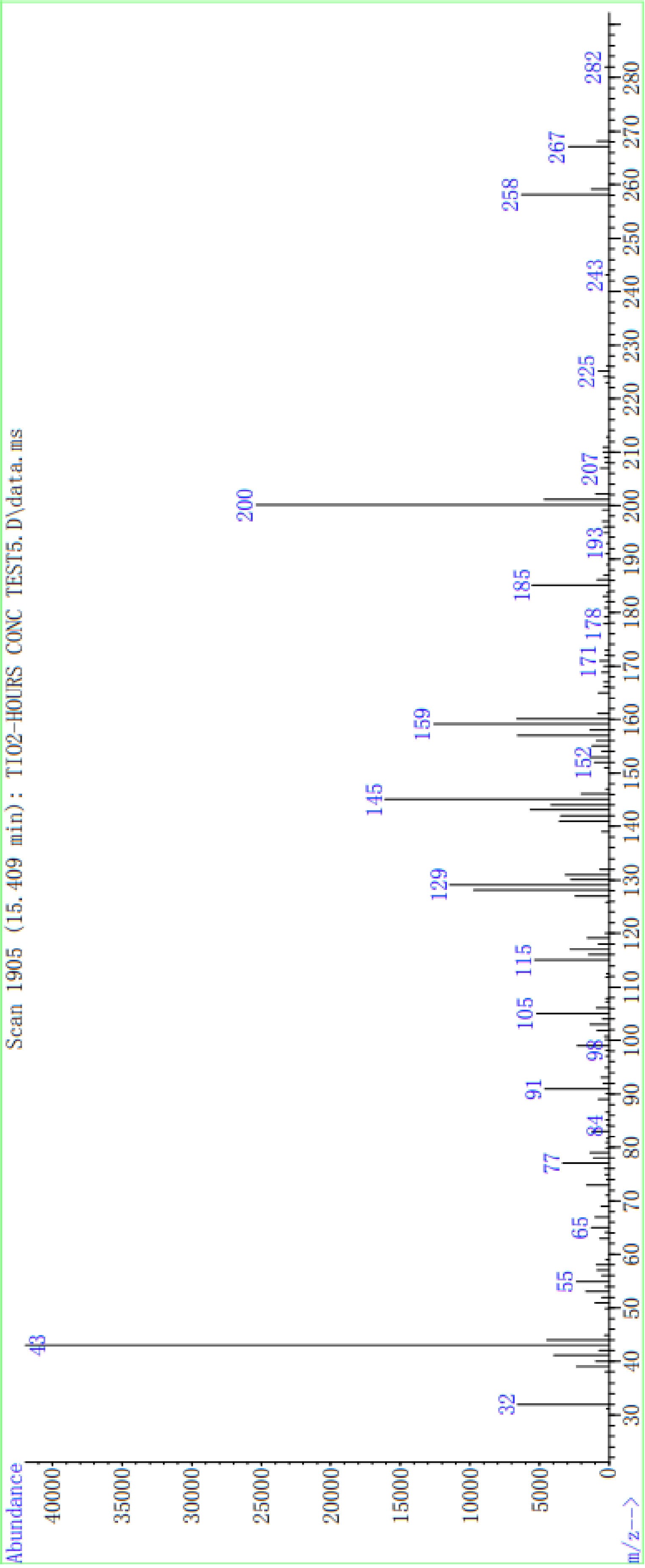
Scan 1905 (15.409 min): TIO2-HOURS CONC TEST5.D\data.ms
Abundance
40000
35000
30000
25000
20000
15000
10000
5000
0
m/z-->
30
40
50
60
70
80
90
100
110
120
130
140
150
160
170
180
190
200
210
220
230
240
250
260
270
280
32
43
55
65
77
84
91
98
105
115
129
145
152
159
171
178
185
193
200
207
225
243
258
267
282

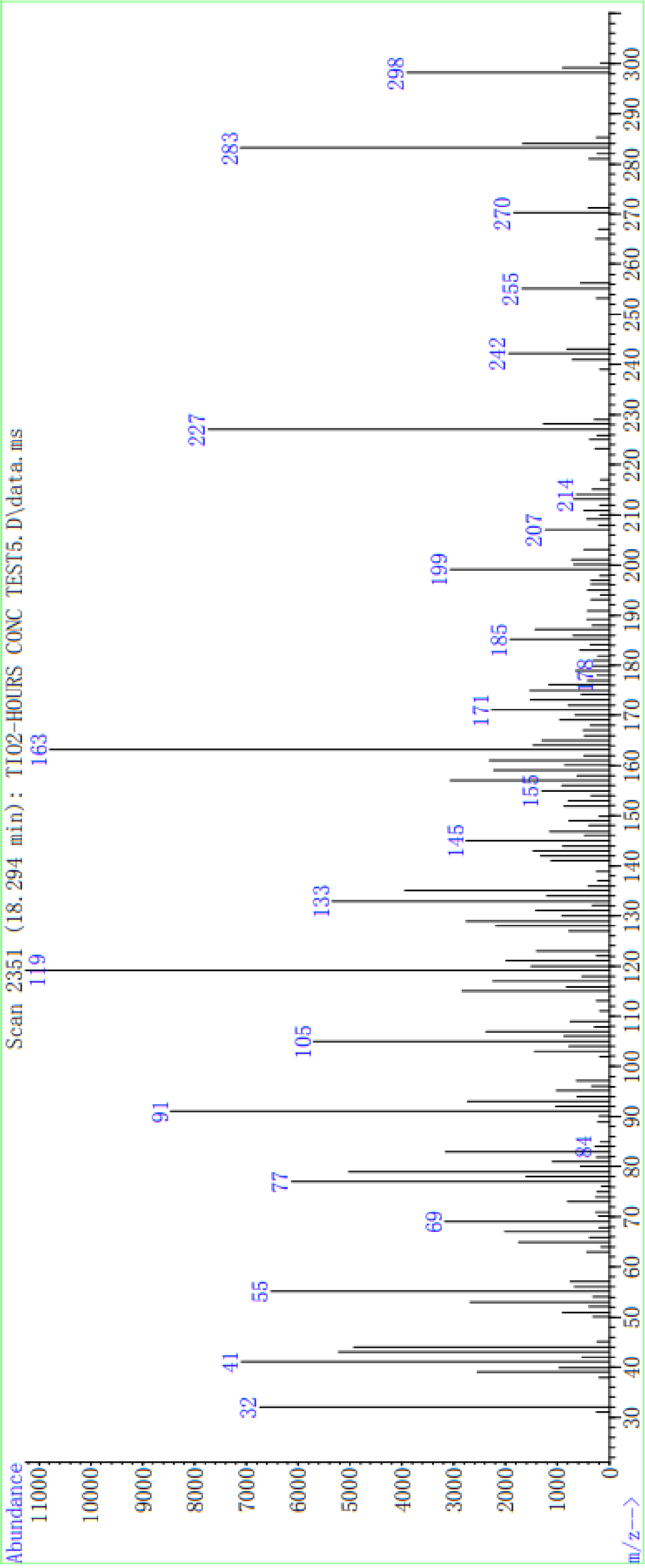
Abundance
Scan 2351 (18.294 min): TIO2-HOURS CONC TEST5.D\data.ms
11000
10000
9000
8000
7000
6000
5000
4000
3000
2000
1000
0
m/z-->
30
40
50
60
70
80
90
100
110
120
130
140
150
160
170
180
190
200
210
220
230
240
250
260
270
280
290
300
32
41
55
69
77
84
91
105
119
133
145
155
163
171
178
185
199
207
214
227
242
255
270
283
298